

A Thesis Submitted for the Degree of PhD at the University of Warwick

Permanent WRAP URL:

<http://wrap.warwick.ac.uk/145635>

Copyright and reuse:

This thesis is made available online and is protected by original copyright.

Please scroll down to view the document itself.

Please refer to the repository record for this item for information to help you to cite it.

Our policy information is available from the repository home page.

For more information, please contact the WRAP Team at: wrap@warwick.ac.uk



Ferromagnetic MnSb Growth on Graphene

by

Nur Alifah Binti Ab Rahman

Thesis

Submitted to the University of Warwick

For the degree of

Doctor of Philosophy

Department of Physics

January 2019



Contents

List of Figures	iii
List of Tables	ix
Acknowledgements	x
Declarations	xii
Abstract	xiii
Abbreviations	xiv
Chapter 1: Introduction	1
1.1 Motivation	1
1.2 Aim and Organisation of the Thesis	3
1.4 Properties of MnSb	10
1.5 Wood's Notation	13
1.6 Convention for Labelling Crystallographic Directions	13
Chapter 2: Experimental Techniques	18
2.1 Chemical vapour deposition	18
2.2 Molecular beam epitaxy	23
2.3 Electron diffraction technique	29
2.3.1 Reflection high-energy electron diffraction	29
2.3.2 Low-energy electron diffraction	35
2.4 Microscopy techniques	36
2.4.1 Atomic force microscopy	36
2.4.2 Scanning Electron Microscopy	37
2.5 X-ray photoelectron spectroscopy	40
2.6 Bulk magnetometry	43
Chapter 3: Pre-growth Substrate Preparation	45
3.1 Introduction	45
3.2 Experimental details	49

3.3	Results and discussion	52
3.4	Summary.....	57
Chapter 4:	Graphene on Cu plate.....	58
4.1	Introduction.....	58
4.2	Experimental details.....	58
4.3	Results and discussion	59
4.4	Summary.....	83
Chapter 5:	MnSb on graphene on Cu plate	84
5.1	Introduction.....	84
5.2	Experiment details.....	85
5.3	Result and discussion	86
5.4	Summary.....	109
Chapter 6:	Graphene on Cu single crystal.....	110
6.1	Introduction.....	110
6.2	Experimental details.....	110
6.3	Results and discussion.....	111
6.4	Summary.....	120
Chapter 7:	Conclusions and future work	121
7.1.	Conclusions.....	121
7.2.	Future work	123
Appendix A	125
References	130

List of Figures

Figure 1-1:(a) the real space structure of graphene. The shaded area shows the unit cell, with two inequivalent carbon atoms, A and B. (b) the reciprocal lattice of graphene. Here the shaded region indicates the first Brillouin zone and the high symmetry points: Γ , M, K and K'. Adapted from [14]. 5

Figure 1-2:The electronic structure of graphene, showing the valence and conduction bands around the first Brillouin zone. On the right is a magnification around K point, where the valence and conduction band meet. This shows the linear dispersion around the so-called Dirac point. Taken from [16]...... 6

Figure 1-3: Polymorphs of MnSb crystallize (a) niccolite (n) (b) cubic (c) and (c) wurtzite (w) structures..... 11

Figure 1-4: MnSb/GaAs hysteresis curves adapted from [37] with a nominal thickness 1.5 nm. Thick solid line: type I, grown on thermally cleaned GaAs. Thin solid line: type II, grown on a 15 nm GaAs buffer layer. The curve of type II shows the same behavior as that of a thick film $\sim 1000 \text{ \AA}$, broken line. 12

Figure 1-5: (a) Crystallographic orientations in hexagonal lattice with three conventional index while (b) by Bravais-Miller indexing which remains unchanged by a rotation of 120° 14

Figure 1-6: Overlayers structures with the highlighted is adsorbate unit cell compare to substrate unit cell. (a), (b) and (c) showing different notations in Wood's and Matrix..... 16

Figure 2-1:Graphene growth mechanism by CVD with (a) Cu plate after cleaning, (b) Cu grains develop during anneal at 950°C , (c) Graphene growth starts with CH_4 (gas precursor) and H_2 at 950°C and (d) Enlargement of graphene flakes and coalescence of graphene domains..... 19

Figure 2-2: CVD schematic setup at University of Warwick. 19

Figure 2-3:The LabView control program for Warwick CVD system. 20

Figure 2-4: Graphene bending energy illustrated for (a) nanofacet and (b) microfacet. A grey circle represents graphene layers at steps and bending energy

applies for changing in direction (circle dashed-line). Red line is the relative energy of graphene layer. Both figures are imagined as a same length on the substrate surface..... 23

Figure 2-5: A schematic of Warwick MBE growth chamber. Effusion cells with Mn and Sb as source material are directed towards a sample substrate heated to the required temperature. RHEED allows in situ observing of the surface on the substrate. 25

Figure 2-6: An illustration of the process which can occur at surface during surface growth. 27

Figure 2-7: Schematic of three idealised growth mode (a) three-dimensional island growth, (b) layer- by- layer growth, (c) wetting layer with three-dimensional island growth. 28

Figure 2-8: Ewald sphere construction for (a) 3D reciprocal lattice, (b) 2D reciprocal lattice also shown is the intersection of the Ewald sphere with the reciprocal lattice rods resulting in the formation of streaks. 30

Figure 2-9: RHEED pattern obtained from a MnSb(0001) surface with the electron beam orientated along the [1120] direction showing a (2x) periodicity. On the right is the schematic of the figure highlights the key features of the pattern. Image courtesy of Dr Chris W. Burrows..... 32

Figure 2-10: Geometric of RHEED pattern to determine lattice parameter. The left-hand side shows the reciprocal space correlation between the Ewald sphere and diffracted beam directions. The right-hand side shows the observed streak pattern..... 33

Figure 2-11: AFM schematic of the optical detection of cantilever movement. The cantilever is deflected up and down due to changes in surface topography and a photodetector is used to determine the direction of deflection through the movement of a reflected laser spot as illustrated on the left-hand side of the figure. 36

Figure 2-12: (a) SEM instrument schematic, (b) Mechanisms of SEM and (c) Illustration of the random excitation in the sample before primary excitation out from the sample..... 38

Figure 3-1: RHEED pattern for Cu foil mounted on MBE sample plate holder. Pink colour on the top highlights a contrast image of shadow edge with black line as a vision guide for eyes.....	45
Figure 3-2: EBSD grain size texture (a) Cu foil, (Image adapted from [38]) and (b) Cu plate. Blue, green and red indicates (111), (101) and (100) grains respectively. Other colours represent direction that lie in between these grains.	48
Figure 3-3: (a) 2-steps and (b) 4-steps preparation methods for Cu foil. Refer to Figure 3-4 for electropolish details.	50
Figure 3-4: Electropolishing set-up for Cu foil/plate (a) large Cu cathode connected to negative terminal (black wire) of the power supply, (b) Cu foil/plate connected to anode (positive terminal, red wire) in the middle.	51
Figure 3-5: SEM images for 2-steps pre-graphene growth (a) Cu foil, (b) Cu plate, inset is a highlight of grain boundaries and impurity spots, (c) and (d) Raman spectrum for both Cu foil and plate respectively, red line is Gaussian fit.	52
Figure 3-6: AFM topography for graphene on 2-steps prepared for Cu plate (a) topography, (b) vertical deflection and (c) horizontal deflection [Black circles highlighted impurity spots while arrows show a graphene grain boundary.	54
Figure 3-7: Reflected light microscope images for (a) Cu plate as purchased, (b) Cu plate after 2-steps and (c) Cu plate after 4-steps with 20 s electropolish.....	55
Figure 3-8: SEM images of Gr on Cu plate after 4-steps substrate preparation with (a) 10 s, (b) 15 s, and (c) 20 s electropolishing time. Growth condition for this study is 20 mins anneal with 5 sccm H ₂ at 950 °C, 30 mins growth time with 10 sccm H ₂ and 3 sccm CH ₄ and cooling to 600 °C with 5 sccm H ₂ and 2 sccm CH ₄	56
Figure 4-1: Raman spectra for graphene on Cu plate (30 min anneal and 20 min growth). Left panel indicates spectrum of dark region while right panel is bright region of the sample. Blue and green shaded areas represent Gaussian fit over a linear background (red lines).	61
Figure 4-2: RHEED pattern obtained from Gr on Cu plate surface. The schematic on the right hand side of the figure highlights the streaks features of the pattern. Pink and white colours on the top left panel highlights a contrast image of shadow edge with black line as a guide for eyes.	62

Figure 4-3: Electron diffraction obtained from a clean graphene on Cu plate surface showing two different areas of scan (a) and (b). The electrons energy are 67 eV, 76 eV and 83 eV of LEED pattern respectively. F1 (green), F2 (pink) and F3 (yellow) are facet points. Green, pink and yellow straight lines indicate graphene domains related with its own facet points respectively. The smooth arc in these imaged labelled 'artifact ring' is an artefact of the channel plate LEED screen.....	65
Figure 4-4: SEM images for 10 mins growth time and anneal at 5 sccm of H ₂ (a) 10 mins, extra panel highlighted white region and impurity spots, and dark non-uniform flakes as bilayer graphene (b) 15 mins, (c) 20 mins and (d) 30 mins.....	66
Figure 4-5: SEM images for longer growth time (a) 20 mins anneal, 20 mins growth, (b) 30 mins anneal, 20 mins growth, (c) 20 mins anneal, 30 mins growth, (d) 30 mins anneal, 30 mins growth.....	68
Figure 4-6: Area density of impurity spots vs anneal time from SEM image.	69
Figure 4-7: Graphene grain size vs anneal time from SEM image.	70
Figure 4-8: AFM for 15 mins anneal and 10 mins growth with different image size respectively (a), (b) and (c).	72
Figure 4-9: Different scan area of AFM for 30 mins anneal and 20 mins growth (a), (b), (c), (d) are topography images and (d), (e), (f), (g) are images in vertical deflection.	74
Figure 4-10: RMS roughness as a function of AFM image size.	75
Figure 4-11: XPS survey scan for TOA 30° (left) and TOA 90° (right).....	76
Figure 4-12: Right panel is fitted XPS spectra of C 1s with TOA 90° and left panel with TOA 30°.....	78
Figure 4-13: Right panel is fitted XPS spectra of Cu 2p with TOA 90° and left panel with TOA 30°. Open circles are experimental data points and red lines show fits as described in the text.	79
Figure 4-14: Right panel is fitted XPS spectra of O 1s with TOA 90° and left panel with TOA 30°.....	80

Figure 5-1: (a) Low magnification SEM image of graphene on Cu plate with red rectangle the position of a zoom shown in (b), (c) Low magnification SEM image of MnSb on graphene (supported on Cu plate) and (d) other part of sample (c)	87
Figure 5-2: MnSb on graphene on Cu plate with 28 nm nominal thickness. (a) Low magnification SEM image using secondary electron mode, (b) High magnification SEM image using backscattering mode with red rectangle the position of a zoom shown in (d), and (c) AFM image with inset of 3D profile.	88
Figure 5-3: SEM image for thinner sample with nominal thickness 1.6 nm with backscattered electron signal mode.	90
Figure 5-4: RHEED patterns for before, during and after growth respectively (a) graphene on Cu plate (b) MnSb growth after 4s and (c) MnSb after Sb cap. Panel (d), (e) and (f) highlight a contrast image of streaks and spots pattern.	91
Figure 5-5: XPS survey scan for MnSb on graphene/Cu.	94
Figure 5-6: An illustration of MnSb growth on graphene on Cu plate	95
Figure 5-7: XPS spectrum of C 1s for MnSb on graphene/Cu. See Appendix 2 for spectral parameter details.	96
Figure 5-8: XPS fitted Sb 3d and O 1s regions indicate Sb-oxides overlapping of atmospheric O. See Appendix 2 for spectral parameter details.	97
Figure 5-9: XPS spectrum for Mn2p of MnSb on graphene.	99
Figure 5-10: XPS spectrum of shallow core region with the Mn 3p and Sb 4d core level presents on the (top) panel and (bottom) panel is Sb 4d regions fitted indicates the presence of Sb-Sb, Sb-Mn and Sb-O. See Appendix 2 for spectral parameter details.	101
Figure 5-11: SQUID magnetometry of a 28 nm MnSb nominal thickness on graphene on Cu plate substrate. Panel (a) shows a hysteresis loop (M-H) acquired at 10 K and 300 K between -3 and 3000 Oe. Panel (b) shows a M-T plot for the same sample taken at a fixed applied field of 3000 Oe, the inset shows a Brillouin function plot for MnSb at $T_c = 590$ K.	104
Figure 5-12: Top panel is a nominal thickness for set of samples versus Mn percentage from XPS, bottom panel is the condition after MBE growth for 28 nm and 1.6 nm nominal thickness, left and right respectively.	105

Figure 5-13: An illustration of graphite crystal structure. The dotted lines model the weak forces between the layers in graphite. The hexagonal unit cell is 0.142 nm and half the crystallographic c-axis spacing is 0.335 nm.....	107
Figure 6-1: Raman spectra for (a) Cu(100) and (b) Cu(410) after 30 mins anneal and 20 mins graphene growth in CVD	111
Figure 6-2: SEM images for Cu(100) with (a) low magnification with green and red a zoom in showed at (i) and (ii) respectively. (b) and (c) displays a higher magnification of the sample.	112
Figure 6-3: Cu(100) LEED patterns from graphene on Cu. (a), (b) and (c) are indexed in (d), (e) and (f) respectively shows graphene orientation preference. Panel (g), (h) and (i) are indexed in (j), (k), and (l) at a higher energy displaying how facets do not move with energy. Blue represents the expected reciprocal lattice of facet spots on Cu(100). Red, green, yellow and purple indicates the graphene rings related with facet Cu(100). (l) in blue line shows the 12 strong graphene spots.....	114
Figure 6-4: SEM images for Cu(410). Panel (a) is low magnification image and red circles represent impurity spots. Panel (b), (c) and (d) are details image with high magnifications and were taken at different spots of scan area. Darker region marks as bilayer graphene and black-dashed line is graphene grain boundaries.....	115
Figure 6-5: Cu(410) LEED patterns from graphene on Cu. (a) (indexed in (b)) shows graphene orientation preference. (b) (indexed in (d)) at a higher energy displaying how facet do not move with energy. F1 and F2 are two different facet points identified in the pattern. Green and pink circles are graphene spots correlate with F1 and F2 respectively. Black line is a mirror plane of 2-fold symmetry.	117
Figure 6-6: Cu(410) LEED pattern. (a) after ion-bombardment and annealing of the surface. (b) Reference LEED pattern from Valbuena et.al [110].	118
Figure A-A-1: C 1s for all MnSb on graphene/Cu sample.	126
Figure A-A-2: O 1s for all MnSb on graphene/Cu sample.	127
Figure A-A-3: Mn 2p for all MnSb on graphene/Cu sample.....	128

List of Tables

Table 1-1: Structural properties of the three polymorphs MnSb.....	11
Table 3-1: Characteristics of two sets of commercial copper used in this study.	47
Table 3-2: Summary of electropolishing time vs area density of spots.....	57
Table 4-1: CVD growth parameters.....	59
Table 4-2: Sample summary for CVD growth study.	60
Table 4-3: Summary of chemical composition for C 1s, O 1s and Cu 2p for XPS spectra of graphene on Cu plate.....	82
Table 5-1: Peak fitting details showing the assigned bonding environment and binding energy for a sample MnSb on graphene. Values are taken from the fits in Figure 5-8.	98
Table 5-2: Sb 4d region peak binding energies, chemical shift relative to the Sb-Sb bonding environment and percentage breakdown of Sb bonding environments for MnSb on graphene/Cu sample. Values are taken from the fit shown in Figure 5-10.	103
Table 5-3: Core level and percentage composition for the C 1s, O 1s, Mn 3p, and Sb 4d.....	103
Table A-1: Growth conditions for all MnSb on graphene/Cu sample.....	125

Acknowledgements

All praises and thanks be to Allah. Once I have made decision, the universe conspired to make it happen.

Firstly, I am profoundly grateful to my supervisor Dr Gavin Bell for his continuous support of my Ph.D study and related research, for his patience, motivation, and immense knowledge. My research would have been impossible without the aid and support for writing this thesis. I could not have imagined having a better advisor and mentor like Gavin.

Dr Tom Hase as my co-supervisor should be thanked for his insightful comments and encouragement and also for all the tough questions he gave which motivated me to widen my research from various perspectives. To Dr Neil Wilson and his group members, I could not thank you enough for the Hamlet's unlimited CVD graphene growth.

My heartfelt thanks go to our group big brother, Dr Chris Burrows who always lent a hand with almost everything with MADGE! Not to forget, Dr Marc Walker the **XPertS's** guy, who gave me invaluable help with Casa and Dr Luke Rochford for his unconditional helps in LEED. Without their precious support it would not be possible to conduct this research. I thank my fellow lab and office mates (Dr Haiyuan Wang, Dr Collins E. Ouserigha, Dr Philip Mousley, Dr Stephanie Glover, Dr Daesung Park, Dr Sepehr Vashegani-Farahani, Dr Mingmin Yang, Dr Danqing, Dr Geanina Apachitei, Alex, and Zhongdong) for the stimulating discussions, for the sleepless nights we worked together before deadlines, and for all the fun we have had in the last four years.

Also, I thank my Coventry friends in “Ladies Kekopi” for endless support in the foreign land. To Fariza, I really appreciated your “don’t mind” as I treated your house as my second home. The struggle is real! Kak N, Farah and Ain, thanks a million for always be by my side through thick and thin. For the last two years without you, I missed you much for our “zero-cost” coffee time, sponsored by Wxx (undisclosed-third party). To Sarah, Fatin, and Amaliyana, thank you is an understatement, May Allah reward you His highest Jannah, always be by my side through my ups and downs living away from home.

My other ukhwah-fillah thanks dedicated to Syakirah and Amilia for always making me realised that every time I was being rejected from something good, I was actually being re-directed to something better. For my Johorian best friends, Nurulsalwan, Farina, Kak Norra, Kak Syarina, Kak Dada, Shafrizan, Suriati, Kak Bibi, Kak Mislina, Kak Maslina, Kak Hairiyah, Cik Nab, Sheila, Junaini, Kak Laila, Mama Gorgeous, Ladies SKBP 1994, Puteri KTAM 1997, Rumpun 1999, the most sincere prayers and positive vibes for me since the first day I had applied for PhD in Warwick, may Allah bless you all with the very best in this life and the next.

Last but not the least, I would like to thank my better half (read: trust me all in all) – Syazarul Shahrir, my 24/7 lucky live reminder with favourite question “How many pages have you written today? Erkkkkk” – Irfan, Alya & Aufa, my supportive parents - Haji Ab Rahman & Hajjah Faridah, my wonderful parents-in-law – Haji Mohd Zainal Abidin & Hajjah Che Sepiah, my loyal sister (read: worth a thousand friends) – Nur Afiqah, and to my brothers and sisters (long list starts now, Salleh, Hakim, Nur Aqilah, Raqib, Khaliq, Zawiyah, Abe Hisham, Kak Yah, Abe Aruwan, Kak Suriana, Abe Affendy, Kak Suriati, Hasrul, Suraida, Hafiz, Suhaila, Athirah and Syahmie) for supporting me physically and spiritually throughout writing this thesis and my life in general.

Declarations

I declare that this thesis reports my work between April 2014 and January 2019 under the supervision of Dr Gavin Bell. The research reported here has not been submitted either wholly or in part in this or any other academic institution for the admission to a higher degree.

The MnSb on graphene/Cu samples used in Chapter 5 were grown with the assistance of Dr Chris Burrows. The LEED data presented throughout this thesis were obtained by Dr Gavin Bell, Dr Marc Walker and Dr Luke Rochford. The RHEED data shown in Figure 2-8 and 3-1 were obtained by Dr Chris Burrows. The EBSD image in Figure 3-2(a) was taken by Dr Alex Marsden. The XPS spectra in Chapter 4 and 5 were taken by Dr Marc Walker. The bulk magnetometry measurements presented in Chapter 5 were obtained by Dr Geanina Apachitei. All other analysis and data collection have been performed by the author.

The work presented in this thesis has been presented at the following international conference.

Growth of ferromagnetic MnSb on graphene (poster presentation), Magnetism 2017, University of York, UK (March 2017)

Abbreviations

2D	two-dimensional
CVD	chemical vapour deposition
MBE	molecular beam epitaxy
SEM	scanning electron microscope
AFM	atomic force microscope
XPS	x-ray photoelectron spectroscopy
RHEED	reflection high electron energy diffraction
LEED	low electron energy diffraction
SQUID	superconducting quantum interference device
TMP	transition metal pnictides
RMS	root mean square
UHV	ultra-high vacuum
EBSD	electron backscattered diffraction
IPA	isopropyl alcohol
CMP	chemical mechanical polishing
DR	double resonance
ISD	impurity spot density
TOA	take-off angle
XRD	x-ray diffraction
TEM	transmission electron microscope
SAXS	small-angle x-ray scattering

Abstract

Integration of ferromagnetic and 2-dimensional material is of interest for potential spin transport applications. Most research materials support the importance of graphene application in many sectors and industries due to its electronic, thermal and chemical properties and potential of being magnetised. This study aimed at fabricating graphene on polycrystalline copper plate with chemical vapour deposition (CVD) and then used it as a substrate to grow epitaxial layers of MnSb by molecular beam epitaxy (MBE). It has been motivated by the transfer of sample in MBE which needs rigid copper substrate to overcome the foil limitation.

The study involved several experiments with the first being focused on pre-growth substrate preparation, graphene growth on Cu plate and single crystal. Graphene growth on Cu(100) and Cu(410) showed the structural feedback or faceting that happened on foil and plate also appeared on bulk single crystal. Graphene domain formation for Cu plate is a mixture of different grain boundaries of crystallography. Important techniques such as SEM, EBSD, AFM, XPS, Raman spectroscopy, RHEED, LEED, and magnetometry were utilised in this experiment. MnSb was chosen due to its promising ferromagnetic materials and the hope that it will be a cubic MnSb (c-MnSb) which can be manipulated as spintronic materials. The quality of monolayer graphene on Cu plate was confirmed by Raman with 2D/G peak ratio between 2 to 4. It then used as substrate for epitaxial growth MnSb on graphene. Although the ultimate aim is to induce magnetism in the graphene layer, the evidence discussed cannot provide the epitaxial behaviour in total.

The magnetic hysteresis loop was detected with the coercive field (667 ± 5) Oe and (900 ± 20) Oe at 300 K and 10 K respectively. The shallow core XPS region for Mn 3p was fitted carefully and showed a metallic state consistent with MnSb.

Chapter 1: Introduction

1.1 Motivation

In frenetic climate, new technologies are emerging each day, and high-tech device development and deployment are on the rise. Most researchers and developers are dedicated to establish new techniques and models for the design of new devices to reduce the costs, capacity, and increase scalability and efficiency. For example, the first stored-program computer 70 years ago could fill in a room, now fits in the palm of a hand due to reduction of its size. Moreover, the evolution of technology in daily life has led the crucial point on how modern communication is driven efficiently in social growth. Additionally, Moore's Law is focused on the emphasis of developing small devices which performs more significant functions because the computers are getting too hot, and the data centers are consuming unsustainable power [1]. The law is mostly based on empirical studies to make technology smaller. In 1965, Gordon Moore stated how the number of components on a printed circuit board had doubled at regular intervals, and that this would continue for "at least ten years" [2]. In fact, this has influenced how most people are involved in technology in the current world. Along with growth in the Moore's Law, there is an increasing concern over the space, the materials and technologies that have been used so far have begun to reach their limits [3]. It also includes the change in design of the devices to address the heat variation by manufacturing devices which process instructions at low clock rates and limits the movement of the chip's electron [4]. Technology advancement with the utilisation of few available materials to create tools impacting industries is a

major motivation for this study with the aim of magnetising graphene while leveraging its thermal, electronic properties.

In 2004, there was a significant inspiration to miniaturisation of technology. The researchers, Novoselov and Geim successfully managed to isolate, manipulate, and then measure a single sheet of graphite with only one atom thick that is called graphene [5]. Being the first two-dimensional crystal, graphene has inspired many possibilities of miniaturisation technology [6] as well as other 2D materials. Graphene has many significant properties that trigger excitement in this crucial technology research. Even though graphene is chemically stable, highly conductive and strong, it is not magnetic. Graphene transfer is avoided due to the tears and cracks [7] formed during the monolayer transfer in the flat substrates such as copper, Cu substrate. On the other hand, the field of material science such as nanomaterial study is receiving a great concern in 2D materials evaluation. Mas-Balleste et al. [8], stated that graphene is just one of the 2D materials. The other 2D materials include hydroxides, metal oxides, chalcogenides and transition metal dichalcogenides. Metal oxides and hydroxides layers separation have been investigated using exfoliation methods but only a single layer is being isolated. The isolation of layers was motivated by graphene sheets separation.

The prospect of combining graphene with other material [9] has attracted more recent attention to magnetise graphene [10], [11]. The integration of ferromagnetism and graphene is of interest for potential spin transport applications. It could help to alter graphene's properties and open routes to existing technologies to enhance their performance when traditional silicon transistor cannot even get smaller as its limits reached.

Spintronics introduce the concept of manipulating the quantum mechanical spin of an electron as well as its charge. Any successful spin injector

materials must satisfy two conditions. First, it is capable of delivering a current with significant spin polarisation. Secondly, any spin injector materials need to be compatible with the present technologies. In this case, a relatively straightforward approach using compound ferromagnetic materials, MnSb as binary pnictide is used. MnSb has promising magnetic properties, stable and abrupt interfaces [12]. This thesis examines how graphene interacts with MnSb. Specifically, it explores how to make graphene as a substrate in epitaxial growth of MnSb. Understanding these interactions will help bring magnetic graphene as a new technology and this has become a necessity in this digital age.

1.2 Aim and Organisation of the Thesis

This thesis focuses on graphene growth on polycrystalline Cu and heteroepitaxial growth of manganese antimonide, MnSb overlayers on graphene/Cu as a substrate. The work represents graphene on Cu plate (0.25mm thick Cu sheet) in the preliminary investigation into the structural aspects problem to overcome epitaxial growth compatibility and surface structure. Additionally the thicker type of Cu substrate was investigated to allow easier manipulation. The work was carried out using chemical vapor deposition (CVD) and molecular beam epitaxy (MBE). The remainder of this chapter states general properties of graphene and the transition-metal pnictides.

Chapter 2 presents the methods and techniques that have been used to study the properties of graphene and MnSb films and interfaces are included. The background theory and experimental schematics are related to the analysis of procedures used. The pre-growth substrate preparation of graphene on the Cu plate and foil is described in Chapter 3. This condition is crucial to getting “ready to grow” condition because the Cu plate and foil have different commercial

material specifications. In Chapter 4, graphene growth in CVD is presented using the best pre-growth conditions explained before. The surface morphology for polycrystalline Cu plate is compared with foil. This includes the study of graphene layers from Raman Spectroscopy.

Chapter 5 details the growth of MnSb on the polycrystalline copper plate as a substrate. A combination microscopy study such as SEM, AFM, XPS, RHEED, LEED and SQUID is presented to understand the properties of MnSb overlayers grown on graphene on copper. The MnSb on graphene is used due to the stable magnetic properties of the material rather than components such as Fe or Co which are affected by hybridisation that polarize some atoms in Fe or Co/graphene [13].

Chapter 6 explains graphene growth on bulk Cu single crystal, Cu(100) and Cu(410). This is a preliminary study of interest structural feedback or faceting feature as compared to Cu foil and plate. SEM, Raman and LEED analysis will be presented in this section. Finally, Chapter 7 concludes the main findings of this research and future works is discussed.

1.3 Properties of Graphene

Graphene is a two-dimensional sp^2 bonded carbon atom. Its primitive unit cell, shown in figure 1-1(a), is a rhombus with two non-equivalent carbon atoms, named as A and B respectively. The basis vectors of the unit cell are

$$a_1 = \left(\frac{\sqrt{3}a}{2}, \frac{a}{2} \right) \quad a_2 = \left(\frac{\sqrt{3}a}{2}, -\frac{a}{2} \right) \quad (1.1)$$

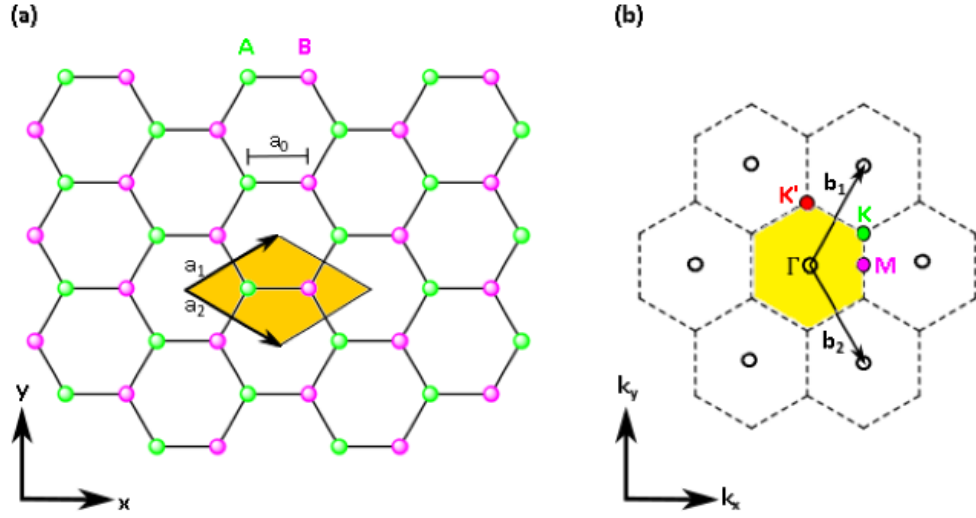


Figure 1-1:(a) the real space structure of graphene. The shaded area shows the unit cell, with two inequivalent carbon atoms, A and B. (b) the reciprocal lattice of graphene. Here the shaded region indicates the first Brillouin zone and the high symmetry points: Γ , M, K and K' . Adapted from [14].

where $a = \sqrt{3}a_0$ is the lattice constant and a_0 is the C-C bond length (0.142 nm).

The corresponding reciprocal lattice vectors are

$$b_1 = \left(\frac{2\pi}{\sqrt{3}a}, \frac{2\pi}{a} \right) \quad b_2 = \left(\frac{2\pi}{\sqrt{3}a}, -\frac{2\pi}{a} \right) \quad (1.2)$$

and these are shown in figure 1.1(b). The high symmetry points are shown and have the vectors

$$\Gamma = (0,0) \quad K = \left(\frac{2\pi}{\sqrt{3}a}, \frac{2\pi}{3a} \right) \quad M = \left(\frac{2\pi}{\sqrt{3}a}, 0 \right) \quad (1.3)$$

Electronic Properties

The reciprocal lattice helps to describe graphene's unique electronic band structure which can be calculated using a nearest-neighbour tight-binding model. It yields the following dispersion relation for graphene [15]

$$E(k_x, k_y) = \pm t \sqrt{3 + 2 \cos(\sqrt{3} k_y a_0)} + 4 \cos\left(\frac{\sqrt{3}}{2} k_y a_0\right) \cos\left(\frac{3}{2} k_y a_0\right) \quad (1.4)$$

with t the hopping parameter (the nearest-neighbour (π orbitals) hopping energy $t \approx 2.8$ eV. E is an energy of electrons with wave vector, k_x and k_y as shown in Figure 1-2. a_0 is a lattice constant with value = 2.46 Å.

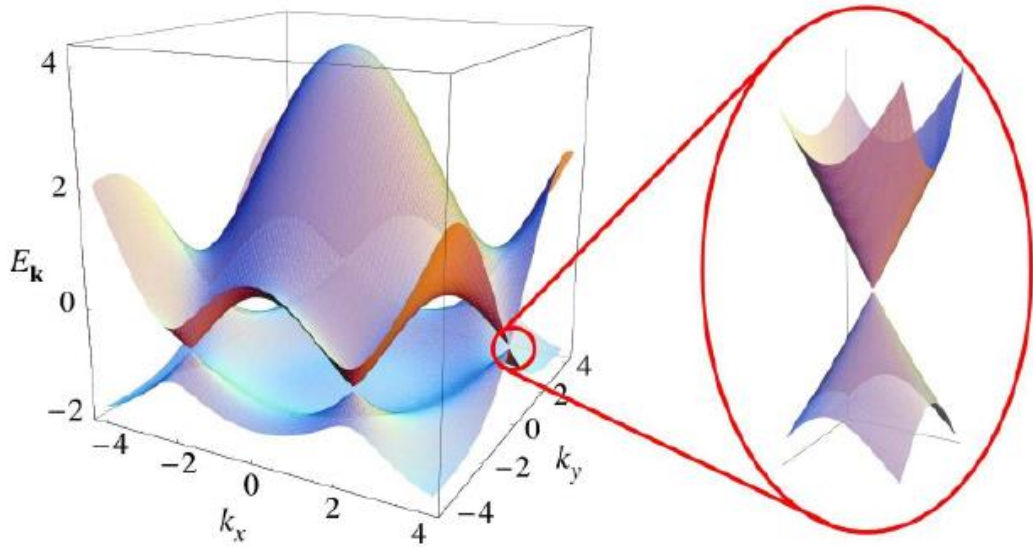


Figure 1-2: The electronic structure of graphene, showing the valence and conduction bands around the first Brillouin zone. On the right is a magnification around K point, where the valence and conduction band meet. This shows the linear dispersion around the so-called Dirac point. Taken from [16].

The most notable feature in the band structure is the linear dispersion around the K point, where the valence band and conduction meet which is highlighted in Figure 1-2. These points are referred to as Dirac points, and the cone shapes dispersion called Dirac cones because of the nature of charge carrier in this region: the linear dispersion implies they behave as if they are Dirac fermions, quantum mechanically described by the relativistic Dirac equation.

Around the K point a nearest-neighbour tight-binding model accurately predicts the graphene band structure and thus can be used to measure the properties of graphene based on this structure. The linear dispersion around K can be approximated to

$$E(q) \approx \pm v_F |q| + O((q/K)^2) \quad (1.5)$$

with $q = K - k$, the momentum relative to the K point. Here v_F is the Fermi velocity which is given by

$$v_F = \frac{3ta_0}{2} \quad (1.6)$$

with t the hopping parameter as before. Around the K point, the density of states ($\rho(E)$) is then

$$\rho(E) = \frac{2A_c}{\pi} \frac{|E|}{v_F^2} \quad (1.7)$$

Where $A_c = \frac{3\sqrt{3}a^2}{2}$ is the area of the unit cell. For undoped graphene, the Fermi level sits at the Dirac point. On the other hand, for doped graphene, the shift in

Fermi level will cause a change in carrier concentration per unit cell (n). This can be calculated using the Equation 1.7 to give,

$$n = \frac{2}{3\pi} \left(\frac{E_D - E_F}{t} \right)^2 \quad (1.8)$$

Where $E_D - E_F$ is the energy of the Dirac crossing relative to the Fermi energy.

Optical Properties

Graphene is highly transparent. It has an opacity of $2.3 \pm 0.1 \%$ and negligible reflectance of $< 0.1 \%$, and optical spectroscopy shows that the opacity is practically independent of wavelength [17].

Epitaxy/Growth Properties

Graphene has a high mobility of electrons ($\mu = 2800 \text{ cm}^2 \text{ V}^{-1} \text{ s}^{-1}$) at room temperature. The electron density denoted as n is $8.1 \times 10^{11} \text{ cm}^{-2}$ and $7.5 \times 10^{11} \text{ cm}^{-2}$ at room temperature and 2.2 K respectively.

Mechanical Properties

A single sheet of graphene has an intrinsic strength $42 \pm 4 \text{ Nm}^{-1}$ and Young's modulus of $1.0 \pm 0.1 \text{ TPa}$ which makes graphene the strongest material ever measured [18]. Despite properties, the fracture toughness of graphene is measured as the critical stress intensity factor of $4.0 \pm 0.6 \text{ MPa}\sqrt{\text{m}}$ and the equivalent critical strain energy release rate of 15.9 Jm^{-2} [19]. The cracked

graphene exhibit a fast brittle fracture behaviour with the breaking stress much lower than the intrinsic strength of graphene [19]. It shows a great ability to minimise the impact force compared to any known material.

Interest in Graphene Magnetism

Graphene has no d or f electrons, hence this mechanism is significant to form a magnetic moment around the copper plate. Also these create tremendous potential for making graphene as a spin generator in spintronics applications. In principle, it can be done in a controlled approach by the introduction of defects to graphene. Theoretically, there are many possible reasons for graphene magnetism. Several attempts have been made to apply atomic-scale defect by using adatoms and vacancies to manipulate and increase the spin-orbit coupling in graphene [11], [20]–[25]. Some researchers [26]–[28] have been reported in spin-polarised states at zig-zag edges. This phenomenon if in-plane homogenous electric fields are applied across the zig-zag shaped edges of the graphene nanoribbons and leads to controllable magnetic properties by external electric fields. Recent evidence suggests that the grain boundary dislocation with the core consisting of pentagon, octagon and heptagon (5-8-7) defect is a typical structural element of dangling bonds and magnetism of grain boundaries with relatively low energies [29]. This was studied by Monte Carlo simulations for a specific type of defects within the grain. Alexandre et al. have been reported their ab-initio calculations of one-dimensional defects with the ferromagnetic ground state at domain boundaries [30]. The investigators have examined the effects of inducing hydrogen-vacancy defect using the quantum-chemistry method. However, the ferromagnetic ordering of the spins is obtained to be limited by the concentration of hydrogen-vacancy defects and would be preserved if the number of defects

does not exceed eight [31]. Using tight-binding approximation, the analytic solution in bilayer graphene has been derived for the wave function of unusual surface states [32].

Magnetic Moments from Defects and Adatoms

The existence of localised moments is frequently described as an outcome of Lieb's theorem which derived for a half-filled single band Hubbard model [33]. This theorem expresses that on a bipartite lattice the ground state has magnetic moment $\mu_B |N_A - N_B|$ with N_A and N_B are the number of sublattice sites. Magnetic moment in the π band can be created with vacancy or removing a site by placing on an adatom, if the defect does not strongly couple π and σ bands [33]. Structural defects in graphene are important because they strongly influence its physical and chemical properties, even at low concentrations. Other defects include nanoparticle graphene etching.

1.4 Properties of MnSb

Manganese, Mn is a transition-metal atom and antimony, Sb is located in a Group V atom in the periodic table. The combination of both groups of these atoms represents intermetallic alloys called the binary transition-metal pnictides (TMPs). MnSb can be presented in a range of crystallographic and magnetic structures. Typically, it exhibits a double hexagonal niccolite (n) structure with an ABAC stacking order and belongs to the space group $P6_3/mmc$ (see figure 1.3(a)). The stacking arrangement is such that the transition metal occupies the 'A' sites, while the pnictogen (Group V) atom occupies the alternating 'B' and 'C' sites. Although MnSb prefers the NiAs-type (niccolite) structure, it also exists in two

other metastable (cubic [zincblende] and wurtzite) phases [34]. Figure 1-3 gives an illustration of the three polymorphs of MnSb, namely (a) niccolite (*n*)-MnSb, (b) cubic (*c*)-MnSb and (c) wurtzite (*w*)-MnSb structures.

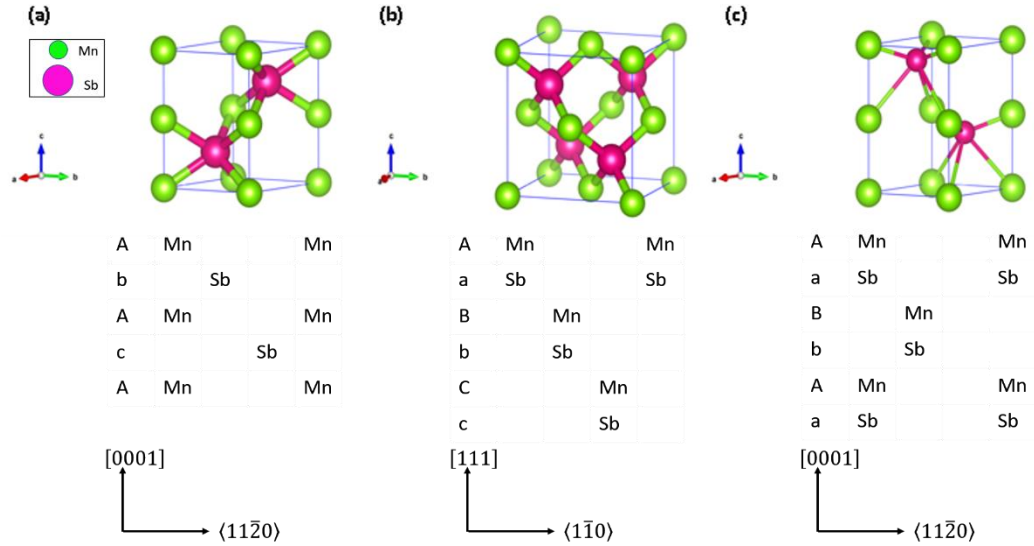


Figure 1-3: Polymorphs of MnSb crystallize (a) niccolite (*n*) (b) cubic (*c*) and (c) wurtzite (*w*) structures.

Their crystallographic information and lattice parameters are listed in Table 1-1. The atoms of a zinc blende unit cell are referred to as tetrahedrally coordinated, and those of a niccolite structure forms a trigonal prismatic geometry.

Table 1-1: Structural properties of the three polymorphs MnSb.

Polymorph	Lattice Parameter (Å)		Reference
Structure	<i>a</i>	<i>c</i>	
Niccolite (<i>n</i> -MnSb)	4.12	5.77	[35]
Zincblende (<i>c</i> -MnSb)	6.21	6.21	[36]
Wurtzite (<i>w</i> -MnSb)	4.29	7.0	[34]

Hysteresis loop is generated by measuring the magnetic flux of a ferromagnetic material while the magnetizing force is changed. Moreover, the failure to retrace the curve of magnetisation in the opposite direction defines the hysteresis property and it is associated with the domains of magnetism existing in the ferromagnetic material.

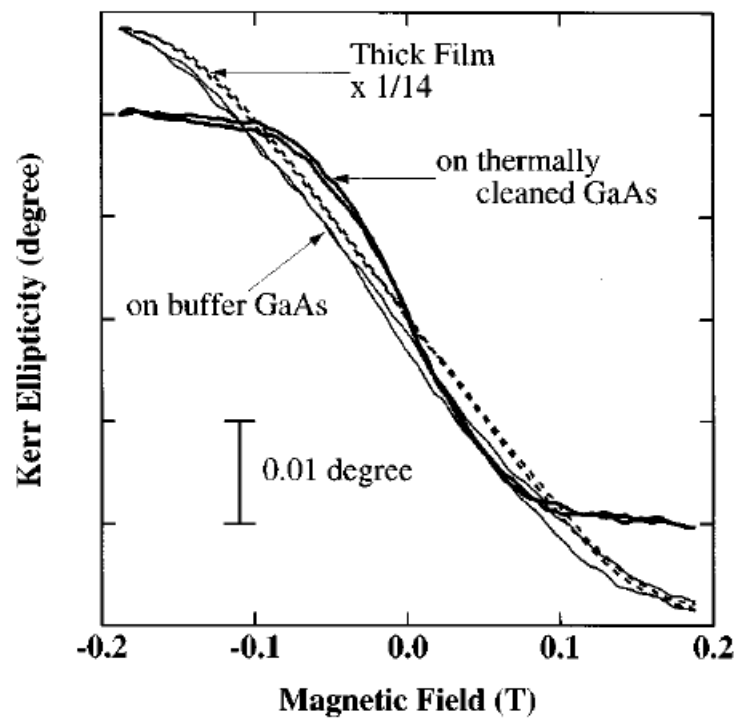


Figure 1-4: MnSb/GaAs hysteresis curves adapted from [37] with a nominal thickness 1.5 nm. Thick solid line: type I, grown on thermally cleaned GaAs. Thin solid line: type II, grown on a 15 nm GaAs buffer layer. The curve of type II shows the same behavior as that of a thick film $\sim 1000 \text{ \AA}$, broken line.

Figure 1-4 shows the hysteresis curve of MnSb(0001) on GaAs(111) with Sb-capped layer. This study by Akinaga et al. confirmed that MnSb magnetisation loops of the thick and thin films were showing the same behaviour respectively.

This motivated an interest in MnSb that has strong magnetic properties and can be detected as thin as 1.5 nm.

1.5 Convention for Labelling Crystallographic Directions

With hexagonal lattice system, using Bravais-Miller system for labelling crystallographic directions, the confusion rises from conventional three index notation can be omitted. In Figure 1-5(a), three index notation leads to the confusion when the $[1\bar{1}0]$ direction which is symmetrically equivalent to $[120]$ but inequivalent to $[110]$. Instead, the four indices ($hkil$) that obey the constraint with $h + k + i = 0$ where h, k and l are identical to the corresponding Miller indices, and i is a redundant index. Apparently, labelling using the four indices system makes permutation symmetries is more obvious in a hexagonal lattice. It is illustrated in Figure 1-5(b), the similarity between $[110] \equiv [11\bar{2}0]$ can be differentiate when indicating the redundant index.

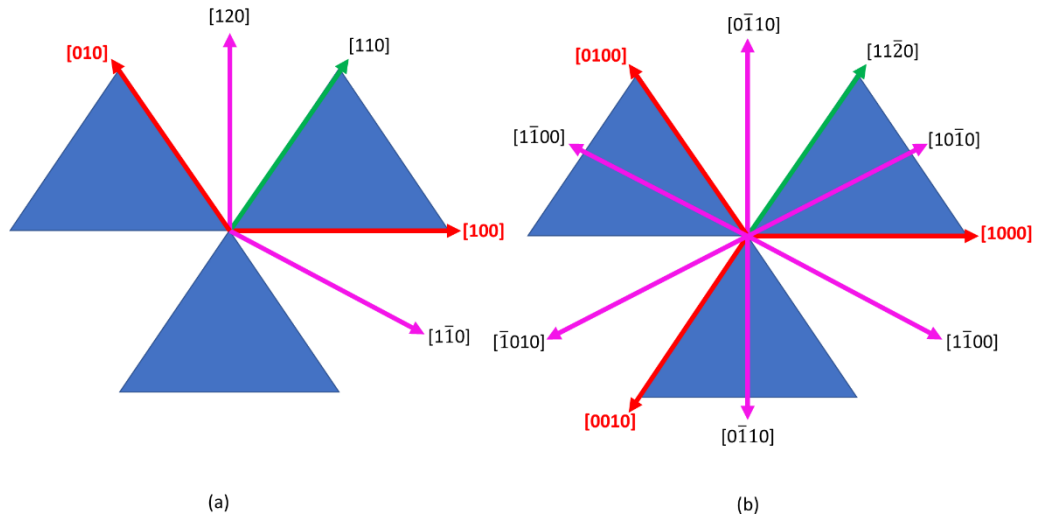


Figure 1-5: (a) Crystallographic orientations in hexagonal lattice with three conventional index while (b) by Bravais-Miller indexing which remains unchanged by a rotation of 120° .

Lattice mismatch is formed by the accumulation of total strain energy up to the levels exceeding the structural transformation energy in the material used. In this study, the mismatch epitaxy occurs when there are differences between the symmetry of orientation between graphene and copper, that is, the hexagonal grapheme over layer is seen on the copper foil surface lower symmetry lattice. According to Wilson et al. [38], there is consistency in the angles measured and calculated between the Cu(110) geometry surface unit cell and graphene orientations which is 10.53° and $10.8^\circ \pm 0.8^\circ$ respectively. Hence the epitaxy of graphene and Cu is a weak mismatch where Cu(110) (rectangular) defines graphene (hexagonal) orientations [38].

1.6 Wood Notation

Classification of overlayer structures can be described by using two principal methods. First, is the matrix notation [39] and the second one is Wood notation which is the most frequently used and simplest for describing a surface structure [40].

The Matrix notation: The matrix system relates the vectors a' and b' to the substrate vectors a and b using a simple matrix.

$$\begin{pmatrix} a' \\ b' \end{pmatrix} = G \begin{pmatrix} a \\ b \end{pmatrix} \quad (1.9)$$

Then, the matrix coefficients G is used to describe the surface reconstruction.

$$G = \begin{pmatrix} G_{11} & G_{12} \\ G_{21} & G_{22} \end{pmatrix} \quad (1.10)$$

It is a more general and system describing surface structures which can be applied to all ordered overlayers. It allows to describe incommensurate adsorbate layers where both substrate and adsorbate do not share the same translational symmetry.

The Wood notation: Wood notation first involves specifying the lengths of the two overlayers vectors a' and b' and substrate unit cell a and b including the rotated angle, which is written as

$$M_{hkl}(m \times n) - R\phi^\circ \quad (1.11)$$

Or

$$M_{hkl}(m \times n)R\phi^\circ \quad (1.12)$$

Here, (hkl) stands for the direction of the crystal (M): ' m ' and ' n ' are the proportionality coefficient of a' and b' , a and b , respectively; \emptyset is the angle of surface unit cell rotating with the underlying substrate in an anticlockwise direction.

Some examples illustrate below in Figure 1-6 to compare the matrix and Wood's notation respectively. If the assumption of rotation between substrate and surface is zero, the $R\emptyset^\circ$ is omitted.

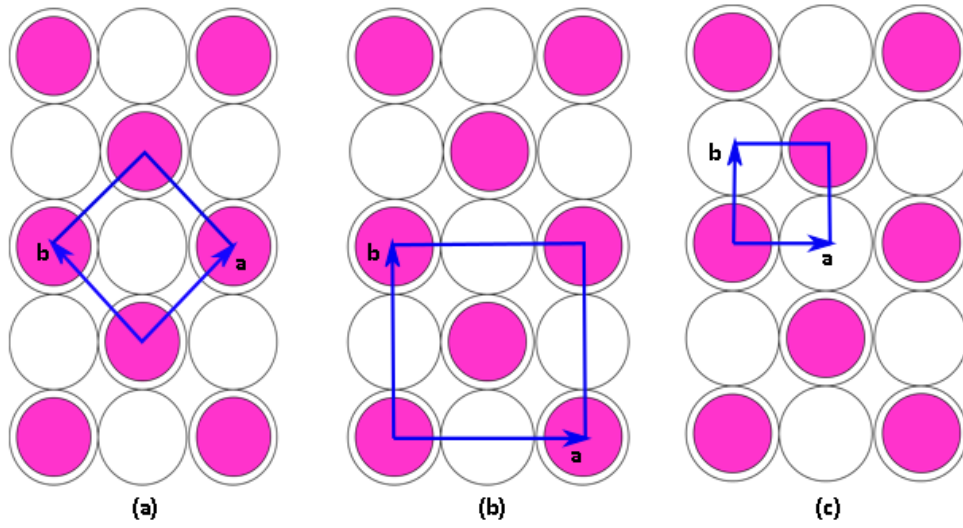


Figure 1-6: Overlayers structures with the highlighted is adsorbate unit cell compare to substrate unit cell. (a), (b) and (c) showing different notations in Wood's and Matrix.

Figure 1-6 (a) describes as $(\sqrt{2} \times \sqrt{2})R45^\circ$ in Wood's notation or $G \begin{pmatrix} 1 & 1 \\ -1 & 1 \end{pmatrix}$ for Matrix notation. While (b) is represents a (2×2) and $G \begin{pmatrix} 2 & 0 \\ 0 & 2 \end{pmatrix}$ using Wood's and Matrix respectively. The basis vector being aligned with the substrate basis vectors. If the assumption of rotation between substrate and surface is zero, the $R\emptyset^\circ$ is omitted. MnSb(0001) epitaxy can be determined by following the orientation of epitaxy on both In_{0.5}Ga_{0.5}As(111) and GaAs(111).

During the epitaxy MnSb, it is recommended that the magnetic anisotropy can be altered significantly but the induced strain must not affect the semi-metallic conductivity in the material [41].

Another crucial epitaxy matrix notation is proposed in Mousley et al. [41] which shows a plausible epitaxy for GaAs(001) on MnSb(1101). GaAs(001) consists of a group of square atoms having a lattice parameter of $b = 4.00 \text{ \AA}$ and it has a two-fold symmetry when a researcher considers dangling bond directions and it is compulsory to have a match with minimal distortions to the mesh of the surface unit which is oblique for MnSb(1101). The perpendicular direction mismatch for GaAs and MnSb[1102] is described using the Equation 1.13,

$$y = \sqrt{C2} + \frac{3a^2}{4} = 6.804 \text{ \AA} \quad (1.13)$$

And notation

$$\begin{pmatrix} 10 & 3 \\ 0 & 1 \end{pmatrix} \quad (1.14)$$

Chapter 2: Experimental Techniques

2.1 Chemical vapour deposition

Chemical vapour deposition (CVD) has been utilised to synthesize graphene. This procedure initially was reported in 2009 [42] and has been developed over the project. The CVD fundamental process is the condensation of a compound or compounds from the gas phase on to a substrate where reaction occurs to produce a solid deposit [43]. Apparently, this is the most promising method, inexpensive and feasible for a single-layer or multi-layers graphene production. CVD has been using transition metal such as nickel (Ni) and copper (Cu) as substrates or thin films as a catalyst. The most famous carbon source is methane (CH_4) and reactant gas hydrogen (H_2) at high temperature ($\sim 950\text{ }^\circ\text{C}$) for the nucleation of graphene [44].

The proposed growth mechanism of graphene on Cu substrate by CVD is shown in the schematic diagram Figure 2-1 with (a) copper plate with native oxide; (b) Native Cu oxide is reduced while Cu develops grains on the surface after annealing at high temperature in H_2 environment; (c) The exposure of the Cu plate to CH_4/H_2 atmosphere at $950\text{ }^\circ\text{C}$ leading to the nucleation of graphene islands; (d) enlargement of the graphene flakes and coalescence of graphene domains with different lattice orientation.

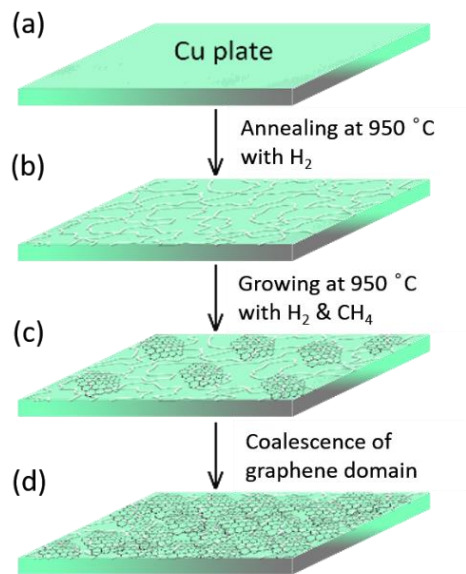


Figure 2-1: Graphene growth mechanism by CVD with (a) Cu plate after cleaning, (b) Cu grains develop during anneal at 950 °C, (c) Graphene growth starts with CH_4 (gas precursor) and H_2 at 950 °C and (d) Enlargement of graphene flakes and coalescence of graphene domains.

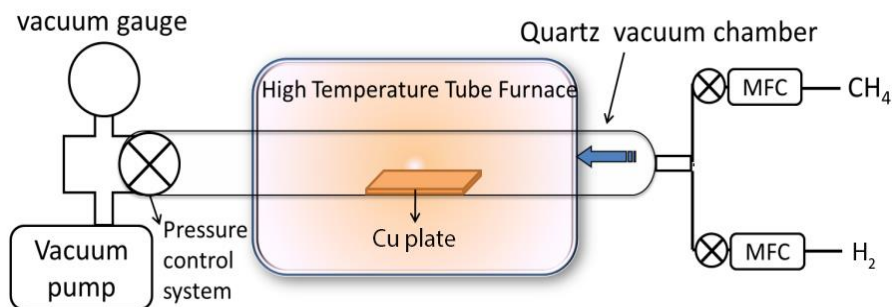


Figure 2-2: CVD schematic setup at University of Warwick.

CVD setup in Warwick (Figure 2-2) which is commonly employed to produce single layer graphene by Cu catalysts. It basically consists of a tube

furnace for high temperature heating, a quartz vacuum chamber, a vacuum and pressure control system for the growth condition adjustment, and several mass flow controllers (MFC) to provide carbon source and reactant gases with a necessary flow rate.

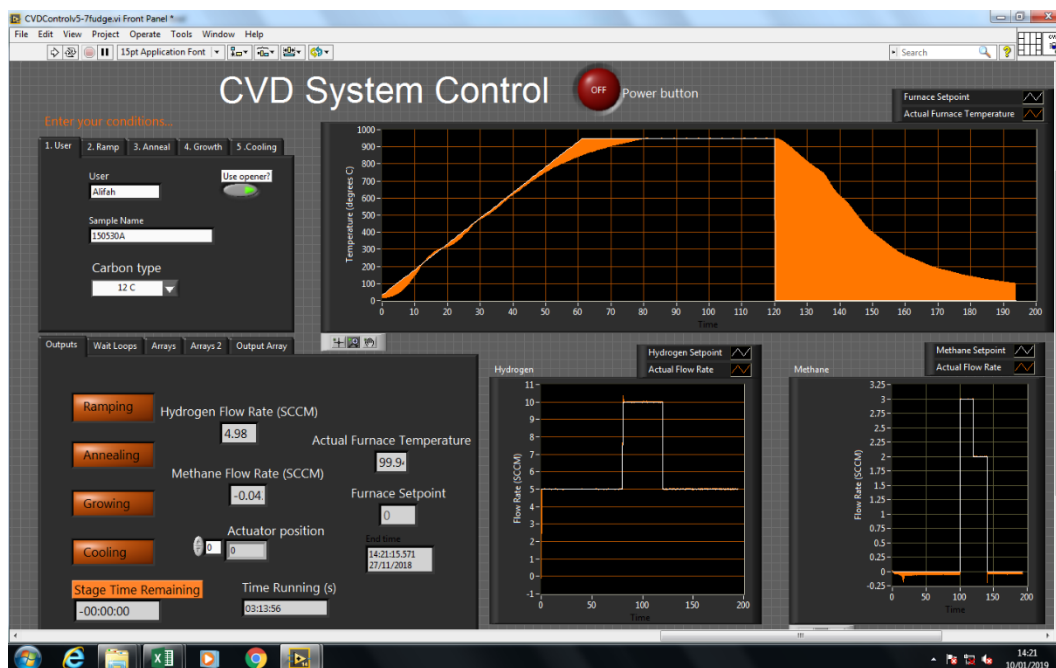


Figure 2-3: The LabView control program for Warwick CVD system.

The heating process was monitored and controlled using the LabView programme shown in Figure 2-3. The Lab View control software requires the system to be powered with reliable power systems, filaments to be turned on and the furnace to be checked. On the other hand, the cooling down process is initiated by turning off the filament, opening the furnace lid and holding it open with a wedge. In the ramp process, temperatures were maintained at 15 °C while the anneal and growth processes both had temperatures set at 950 °C with H₂ and CH₄ flowing rate of 10 and 3 sccm respectively. Temperature is a crucial factor in

examining the growth process. Graphene could only grow at temperatures over 600°C as the Cu catalytic effect and dissociation of methane and hydrogen molecules could not take place below that temperature. For graphene growth on Cu, temperatures are set up to 950 °C. Anything above that temperature will melt the copper. High-quality graphene was also realised when heated at high temperatures of up to 1000 °C, and it must not exceed the melting point of copper which our experiment noted carefully [45].

Using high temperature, the reactivity of the methane, hydrogen and copper will increase. This will allow the general reactions and at the same time control how the growth progresses, nucleation and the growth rate. As temperature increases, nucleation density of graphene decreases [46]. At lower temperatures the rate limiting step for nucleation is thought to be movement of carbon adatoms, and desorption at higher temperatures [47]. In addition, higher temperatures decrease the copper surface roughness which lead to reduction of number of sites of nucleation and improve the adsorbates mobility [48]. Annealing at high temperatures could decrease the grains on the copper substrate. This causes weak mismatched epitaxy of the graphene with the copper foil and allows more uniformly orientated growth of graphene. Thus, copper needs to be annealed under hydrogen before growth in order to improve the substrate surface.

The rate of growth of existing islands and the rate of nucleation and subsequent new islands determines the size of islands. The size of islands could be controlled by the ratios and partial pressures of methane and hydrogen. As a stable precursor even at high temperatures, methane is usually chosen in CVD growth of graphene on copper substrates, compared to larger hydrocarbon which have a high pyrolysis rate [49]. This cause a large amount of carbon deposition on

the surface of the catalyst, and influences a larger number of defects in the graphene sheets [47]. We used the minimum amount of methane to minimise nucleation density and to allow large grain growth.

Using hydrogen with methane is crucial as it is responsible for the activation of the surface bound carbon which is necessary for growth. Hydrogen also helps to control size and morphology of graphene islands by etching weak carbon-carbon bonds and preventing oxidation of the surface [50]. To produce a very high density of small islands or a very sparsely distributed large grains, it is critical to balance etching and growth of graphene. The growth could be altered by changing the ratios of methane to hydrogen which will change the rate of reaction and proportions of molecules of particular energies. The presence of monatomic hydrogen radicals affect the growth of lobed graphene islands with low concentrations linked to hexagonal graphene islands by considering the gas phase equilibrium in a hot-wall CVD system [49]. The balance between hydrogen and methane must be checked to produce the right balance between etching, growth and nucleation to produce large or small grain graphene. In this study, we used fixed ratio of H_2 and CH_4 as stated in Table 4-1.

CVD graphene growth on any substrate has triggered a general phenomenon of step bunching (SB) on 2D materials. Yi et.al found that the SB can occur even in the absence of a compressive strain, is enabled by the rapid diffusion of metal adatoms beneath the graphene and is driven by the release of the bending energy of the graphene overlayer in the vicinity of steps [51]. In this thesis we called it facet features.

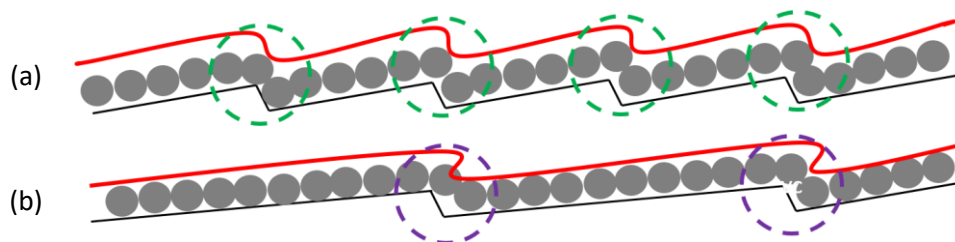


Figure 2-4: Graphene bending energy illustrated for (a) nanofacet and (b) microfacet. A grey circle represents graphene layers at steps and bending energy applies for changing in direction (circle dashed-line). Red line is the relative energy of graphene layer. Both figures are imagined as a same length on the substrate surface.

Figure 2-4 shows an illustration of graphene bending energy on facets. The grey circle is representing C atom to form the most stable condition of graphene layer on surface. Both figures are not scaled but imagined within the same length on transition metal substrate. The illustration demonstrates that graphene on (b) micro-facet needs to bend twice rather than (a) nano-facet with 4 times to firmly attach to the surface. This bending energy is minimised after faceting occur. This signature behaviour that we can see previously in our foil and facet direction always on (100) + (210) due to roll to roll Cu foil production [52]. It is roll-based production of graphene films grown on Cu foil.

2.2 Molecular beam epitaxy

The technology of crystal growth has improved tremendously during the past decades. In the midst of these approaches, the development and refinement of molecular beam epitaxy (MBE) has been among the most important. Crystal growth by MBE is a versatile technique for growing thin epitaxial structures made

of semiconductors, metals or insulator. It is simply crystallization by condensation or reaction of a vapour in ultra-high vacuum (UHV). What distinguishes MBE from other vacuum deposition techniques are its significantly more precise control on the beam fluxes and growth conditions. Because of vacuum deposition, MBE growth is carried out under conditions far from thermodynamic equilibrium and is governed mainly by the kinetics of the surface processes occurring when the impinging beams react with the outermost atomic layers of the substrate crystal.

Molecular beam epitaxy (MBE), first successfully conducted by Arthur and Cho [53] in 1960 is a technique that allows the growth of thin film of crystalline materials on a substrate of the same (homoepitaxy) or different (heteroepitaxy) material. The applications of MBE are vast especially in a technology that fundamentally depends on the growth of multilayer heterostructures such as, solid-state, high-speed transistors, light emitting diodes, and microprocessors. The reason MBE is very significant is its ability to control the thickness of growth material to the atomic level. Besides, MBE is very powerful technique to 'fine tune' the electronic and structural properties of the thin film using strain engineering.

The working principle of MBE is very simple and straightforward. The molecular beams is formed from the heated shuttered cells containing source material (sublimation) and directed towards the substrate. This process is only feasible under vacuum conditions as a result of the large mean free paths possible at such low pressure, $<10^{-5}$ mbar. Under certain conditions like baked vacuum chambers i.e. H_2 , H and CO in which either or both of the electronic properties and crystallographic structure are affected by the contaminant's integration, one must ensure that the density of contaminants remains as low as possible. This will require a more intense condition on the base pressure and the usage of UHV, where the background pressures should be $< 10^{-9}$ mbar [54].

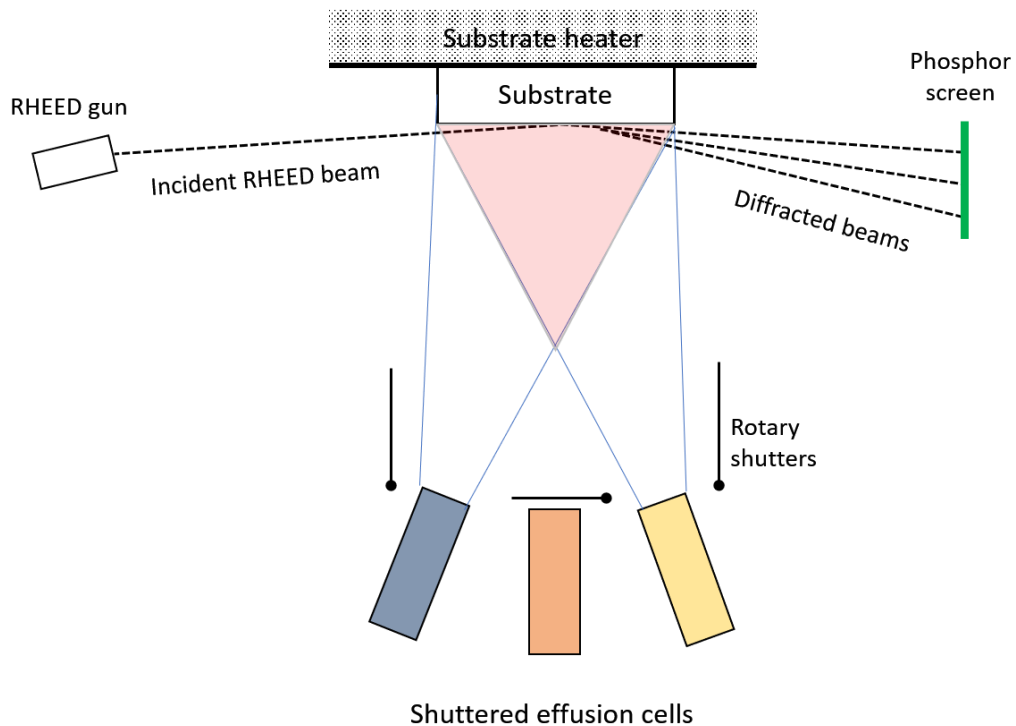


Figure 2-5: A schematic of Warwick MBE growth chamber. Effusion cells with Mn and Sb as source material are directed towards a sample substrate heated to the required temperature. RHEED allows in situ observing of the surface on the substrate.

MBE setup is shown in Figure 2-5. On a removable sample plate which is embedded into a manipulator, a target substrate is attached to it with the substrate directed shuttered effusion cells. Owing to this, the reflection high energy electron diffraction (RHEED) can be used to assess the surface crystallinity and harshness, determine the symmetry, growth orientation and surface reconstruction.

More detailed discussions of the RHEED technique are reserved for Section 2.3.1. The shuttered effusion cells made of ceramic crucible, normally a pyrolytic boron nitride, PBN or alumina and are heated either in direct thermal using a hot filament or by electron beam (e-beam) heating. The growth material determines

the heating method used. According to the Clausius- Clapeyron equation, source materials shows a vapour pressure-temperature behaviour,

$$P = P_0 \exp\left(\frac{-\Delta H}{RT}\right) \quad (2.1)$$

where P is the beam equivalent pressure as measured by a pressure gauge in the path of the beam (beam flux gauge, BFG), ΔH is the enthalpy of sublimation or evaporation (depends on source material) at a temperature T and R is the molar gas constant.

As mentioned earlier, the enthalpy of sublimation is dependent on the source material. For materials with substantially large enthalpy of sublimation such as nickel, sublimation process is considerably difficult to happen [55]. This material would incline towards the electron beam (e-beam) heating method, often with high purity rods ($\geq 99.99\%$ pure) source material exposed in the vacuum. For materials with low enthalpy of sublimation, direct heating to the crucible is substantial to achieve the required beam pressure. The beam pressure stability can be neglected over the growth time. For low sublimation enthalpy material, the thermocouples is used to stabilise the source temperature and a proportional integral derivative (PID) control is used to regulate the power output from the cell's power supply.

At the surface of substrate, atoms and molecules can undergo a number of chemical process at atomic level as shown in Figure 2-6. The rate of each process is determined based on the equation below,

$$R_b = v_0 \exp\left(\frac{-E_b}{k_B T}\right) \quad (2.2)$$

where E_b is the barrier height associated with each process, ν_0 is the frequency related to the lateral vibrations of the atom, and T is absolute temperature of the surface.

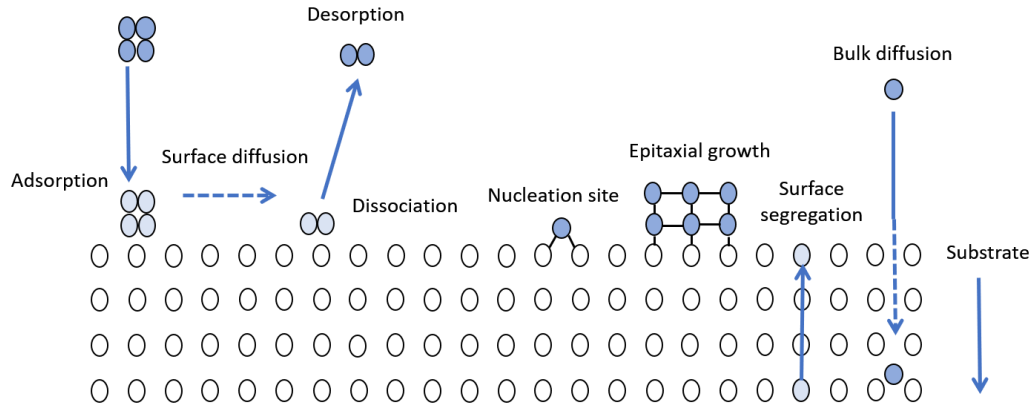


Figure 2-6: An illustration of the process which can occur at surface during surface growth.

When the atoms come close or in contact to the surface, the atoms can be adsorbed physically (physisorption) which is characterised by van der Waals interaction or chemically (chemisorption) which occurs when atoms undergo electron exchange process to the substrate. There are few factors that can affect the resultant thin film. The desorption rate of atoms from the surface substrate depends on the substrate temperature. Not only that, the substrate temperature also affects the kinetic of atoms to migrate on the surface. Next the relative desorption rate (sticking co-efficient) depends on the chemical potential at the surface which is closely associated with the relative abundance of the growth elements that is determined by the beam flux ratio [56]. Besides that, the structural difference between the substrate and the growth layer plays an important role in this process.

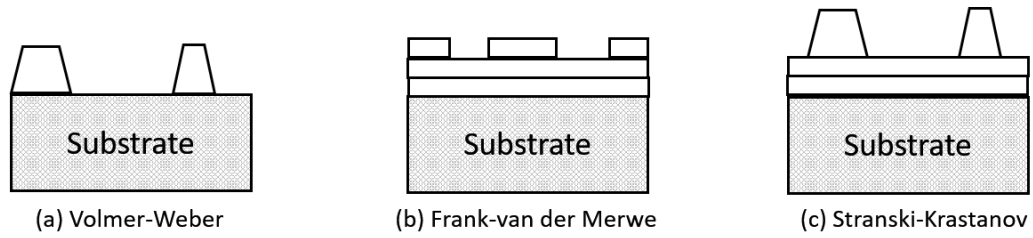


Figure 2-7: Schematic of three idealised growth mode (a) three-dimensional island growth, (b) layer- by- layer growth, (c) wetting layer with three-dimensional island growth.

There are three ideal growth modes which are affected by the interactions between the growth atoms and the substrate. The layer-by-layer growth, known as Frank-van der Merwe mode is favoured in most applications. In this mode, one atomic layer is formed completely before another layer is formed as shown in Figure 2-7(b). However, when the interaction between growth atoms is stronger than interactions between growth atoms and substrate, the 3D island or Volmer-Webber mode is preferred as shown in Figure 2-7(a). Laying between these two modes is the hybrid between the layers and 3D island known as the Stranski-Krastanov mode, Figure 2-7(c) and is observed in the growth of semiconductor quantum dots.

The growth modes are not limited to only those three above even though they are the ideal modes. The crystallographically oriented nanorods can grow spontaneously in-plane or out of-plane from the surface substrate [57], [58] . Other than that, endotaxy is another mode in which oriented crsytallites grow into the substrate due to the high chemical reactivity at the interface which have been observed with MnSb on InP(111), [35] and MnSb on GaSb(001), [59] .

2.3 Electron diffraction technique

The electron diffraction method has been developed based on the wavelike nature of electrons. Fundamentally, a beam of electrons is accelerated to the sample and the diffraction pattern that is formed from it can be utilised to examine the sample. In this section, two particularly advanced electron diffraction technique will be discussed, reflection high-energy electron diffraction (RHEED) and low-energy electron diffraction (LEED).

2.3.1 Reflection high-energy electron diffraction

RHEED involves electrons of high energy which lies between 8 to 20 keV. The electrons incident upon a surface at a grazing angle between 1 to 6 degrees. The electrons then emerged as diffracted beams and projected onto a phosphor screen. The primary reason for the incorporation of this technique into MBE chambers is the electron beam is perpendicular to the direction of the molecular beams, as shown in Figure 2-5. As a result, during growth, the behaviour of thin films can be observed in real-time which can give insight on both structural and morphology of the surface. The structural information can be obtained in the form of surface periodicity and in-plane lattice parameters. In the meantime, the diffraction patterns can give information about the presence of 3D islands, roughness of a surface and crystallisation of a material.

The electron beams will undergo elastic scattering and forms scattered beams. The energy of the electrons is conserved in Equation 2.3,

$$|E_f = E_i| \quad (2.3)$$

where E_f is the final energy of the scattered electron and E_i is the incident energy of the electron. Momentum and energy are related via Equation 2.4(a)

$$E = \frac{\hbar^2 k^2}{2m_e} \quad (2.4a)$$

Since \hbar and m_e are constant, the equation could be simplified as

$$|k_f| = |k_i| \quad (2.4b)$$

where k_f is the final wavevectors of an electron and k_i is the initial wavevectors of an electron.

If the diffraction occurs in 3D, the k_i can change only by a discrete amount with regards to the 3D reciprocal lattice G_{ijk} , of the scattering crystal,

$$k_f = k_i + G_{ijk} \quad (2.5)$$

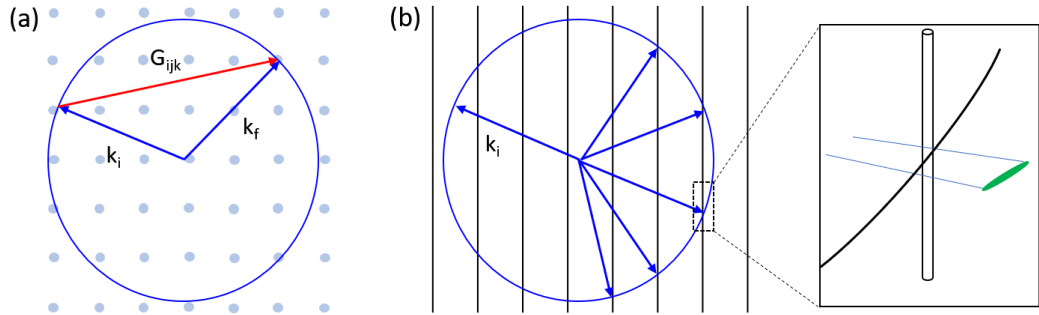


Figure 2-8: Ewald sphere construction for (a) 3D reciprocal lattice, (b) 2D reciprocal lattice also shown is the intersection of the Ewald sphere with the reciprocal lattice rods resulting in the formation of streaks.

In which G_{ijk} is a lattice vector of the 3D reciprocal lattice. Equation 2.5 can be represented graphically using Ewald sphere construction, as shown in Figure 2-8. In this sphere construction, a circle with radius k_i is drawn on a 2D projection, originating from reciprocal lattice point. All points that lie on the surface of the sphere will satisfy the diffraction conditions and Equations 2.3-2.5.

At the surface the periodicity becomes depleted perpendicular to the surface causes the reciprocal lattice points to form infinitely long rods. The long rods are also perpendicular to the surface. Accordingly, Equation 2.5 reduces to the following form,

$$k_f = k_i + G_{ij} \quad (2.6)$$

G_{ij} is now a vector of the 2D reciprocal lattice. Ewald sphere is reduced to a circle as shown in Figure 2-8(b). All points that are in the perimeter of the circle satisfy the diffraction conditions. In RHEED, the intersection between Ewald sphere and the reciprocal lattice is almost tangential because Ewald sphere is greater than the width of the reciprocal lattice rods.

In case of a perfect surface, the pattern formed will be made up of a series of spots where the interception of the rods and Ewald circle is apparent, but this is not observed due to the heat contamination. Thermal diffuse scattering and finite-size disorder the rods gain a finite width and so the intersection results in the formation of streaks, as indicated in Figure 2-9. Besides, if the electron source is not monochromatic, it can cause the formation of a range of incident wavevectors although the effect of the surface disorder is always greater than the width arising from the source [60].

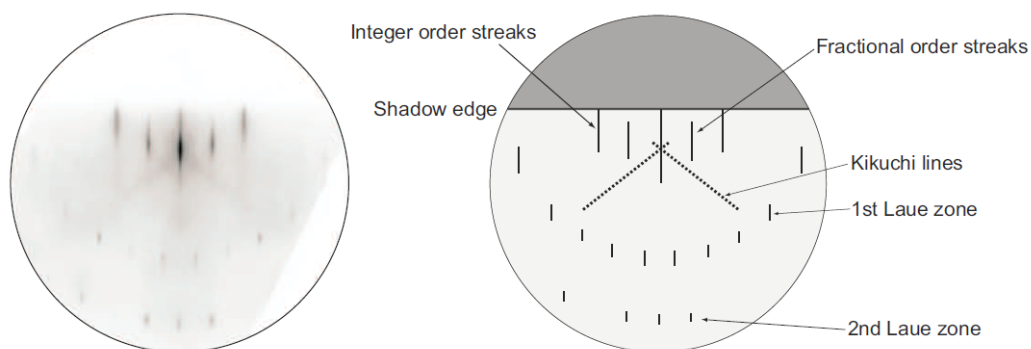


Figure 2-9: RHEED pattern obtained from a MnSb(0001) surface with the electron beam orientated along the $[11\bar{2}0]$ direction showing a $(2\times)$ periodicity. On the right is the schematic of the figure highlights the key features of the pattern. Image courtesy of Dr Chris W. Burrows.

2.3.1.1 RHEED pattern interpretation

The RHEED patterns can be very difficult and hard to interpret because of multiple phenomena which occurs when the electron beam strikes the surface. Figure 2-9 shows an example of RHEED pattern with a corresponding schematic. There are few characteristics in the pattern that are important. Firstly, the intense streak which is connected to shadow edge is the integer order streaks that are formed due to diffraction from rows of atoms in bulk-like positions. The less intense streaks are the fractional order streaks that are formed due to surface reconstruction. This indicates that the surface has been reconstructed in any way possible and the surface periodicity is different from that of the bulk. The example pattern shown in Figure 2-9 has a single fractional streak between the integer streaks and is indicative of a $(2\times)$ periodicity. The sample need to be rotated about the normal surface to determine the reconstruction of the surface. The angle of

rotation differs in each symmetry of the surface. For surface with square symmetry, for instance the III-V(001) surfaces the sample has to be rotated 90° while for surface with hexagonal symmetry like MnSb(0001) or III-V(111), the sample has to be rotated by 30° to determine the reconstruction.

Another important characteristic in RHEED pattern is the dotted lines which is renowned as Kikuchi lines. Kikuchi lines are formed when the inelastic scattered beams acting as incident beams inside the crystal. Kikuchi lines can be used as an indicator of crystallinity and quality of the layer as they are able to be diffracted from bulk planes. They can also be used to align the crystal along high symmetry directions as they are specific to the orientation of crystal under study. Another characteristic is the area of lower edge of the phosphor screen which correspond to Laue zones which are formed when the Ewald sphere intersects higher order reciprocal lattice rods.

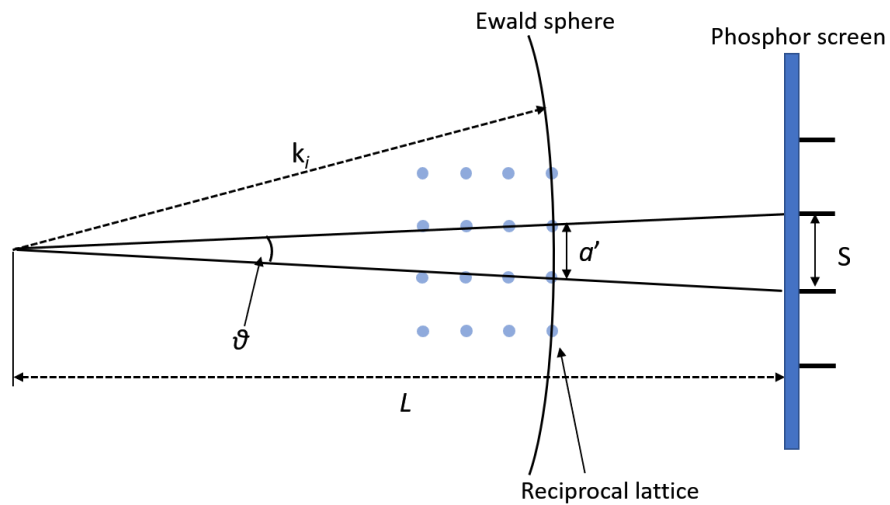


Figure 2-10: Geometric of RHEED pattern to determine lattice parameter. The left-hand side shows the reciprocal space correlation between the Ewald sphere and diffracted beam directions. The right-hand side shows the observed streak pattern.

The distance between integer streak spacing can give information about the in-plane lattice parameters. By using the small angle approximation, the angle between two diffracted beams, θ , can be calculated by using formula below:

$$\tan \theta = \theta = \frac{a'}{k_i} \quad (2.7)$$

where a is the reciprocal lattice spacing. From Figure 2.10, reciprocal lattice spacing can be derived as

$$a' = \frac{k_i s}{L} \quad (2.8)$$

where s is streak separation that is equivalent to the θ , and L is the camera length. The real space lattice parameter is inversely related to the reciprocal lattice parameter, hence the Equation 2.9(a) and (b),

$$a = \frac{2\pi}{a'} \quad (2.9a)$$

$$a = \frac{2\pi L}{\sin \phi k_i s} \quad (2.9b)$$

the spacing relation has been normalised for non-square surfaces where the angle between the primitive lattice vectors, ϕ has been taken into account. In this thesis, RHEED gun was operated at 12.5 keV and k_i is $5.7 \times 10^{11} \text{ m}^{-1}$, and the camera length is 280 mm.

In this work, the streak spacing was determined using a standard digital camera to capture the still image of the diffraction pattern. The image was then analysed using ImageJ. The quality of the image can be improved by converting the pixels to millimetres through the usage of two phosphor squares, (the distance

between the two squares is known) attached to one side of the RHEED screen flange. The incident angle of the beam can be measured from the separation of the straight-through beam and the specular refraction, with $\theta_i = \theta_{out}$ when the calculation of size terraces is performed. The radius of the zeroth Laue zone, where the specular line is located can be used to determine the incident angle following the equation [60]

$$R = L \tan \theta_i \quad (2.10)$$

where R is the radius of the zone, L is the camera distance and θ_i is the angle of incidence.

2.3.2 Low-energy electron diffraction

The way RHEED works is similar to LEED except that electrons in LEED possess energy of 20-200 eV. The low energy electron ensures the surface specificity which have IMFP values in the range of 2-10 Å. Consequently, the probing depth is also limited to this range. LEED is particularly more significant when analysing rotated domain structures or more complex reconstruction as the complete periodicity of the surface reconstruction can be captured in a single image. This is owing to the change from grazing to normal incidence that results in a plan-view projection of the reciprocal lattice/Ewald sphere interaction.

In comparison to RHEED, LEED has a disadvantage which is the lack of sensitivity to the surface morphology and 3D surfaces. This is because the transfer width in LEED lies between 30 and 100 Å and is significantly lower than RHEED [61].

2.4 Microscopy techniques

2.4.1 Atomic force microscopy

Atomic force microscopy technique was developed by Binnig et al. [62] in 1986. As a result, a surface can be scanned with a higher lateral resolution than 10 nm and a lower vertical resolution than 1 Å without having to endure the complexity of UHV conditions.

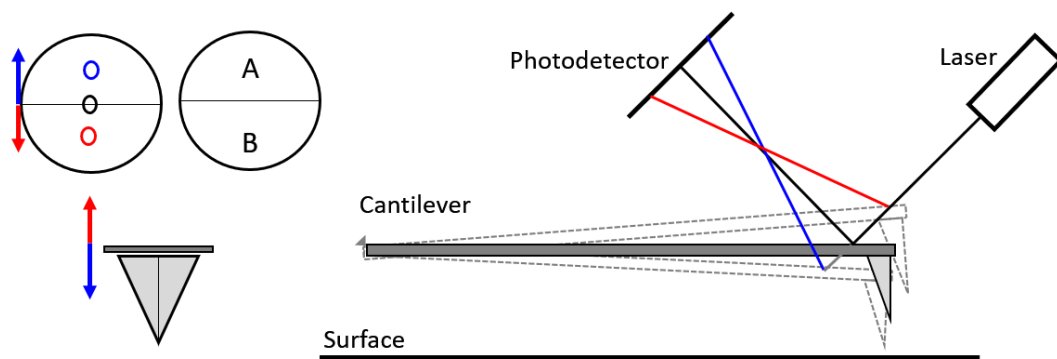


Figure 2-11: AFM schematic of the optical detection of cantilever movement. The cantilever is deflected up and down due to changes in surface topography and a photodetector is used to determine the direction of deflection through the movement of a reflected laser spot as illustrated on the left-hand side of the figure.

The interaction between the surface and the tip in AFM is the underlying method. A sharp tip, usually 10 nm to 25 nm across at the apex is attached to the end of a soft cantilever is moved across the surface and the distance of the tip to the surface is within a few angstroms. Any forces that act on the tip causes the tip to be deflected away from its equilibrium position. The deflection corresponds to the force experienced by the tip. The deflection is then measured using a laser

beam. A laser beam from the back of cantilever is reflected onto a four-zone photodetector, as depicted in Figure 2-11 (only two photodetector zones are shown, A and B). When the cantilever is deflected, the laser spot moved on the photodetector and each photodetector received different laser intensity. The difference in intensity between the top A and bottom B halves of the photodetector correlates with the force felt by the tip.

AFM is consisting of two main operating modes, contact and tapping. In contact mode, the deflection is constant. In order to do so, the tip needed to touch the surface and raster scans using a feedback loop. Meanwhile in tapping mode, the distance between the tip and surface is kept constant. The cantilever oscillates slightly higher than its resonant frequency and any forces that acts on it will change the amplitude of oscillation will give information on the topography of the surface. In practice, all of the work in this thesis was done using a Veeco Multimode with contact mode. The tips used were CSC 17/AL BS ($k= 0.18 \text{ N/m}$, 13 kHz, resonance frequency).

2.4.2 Scanning Electron Microscopy

Optical microscopes are limited by the wavelength of light, thus electron microscope is developed because the electron has shorter wavelength than light. This shorter wavelength of electron is able to provide a better resolution, down to a few nanometres in size of a surface features and defects that vary in size from a few angstroms to a few micrometres.

Electrons accelerated to tens of keV are treated as waves which has a very small wavelength. A thermionic electron gun or a field emission gun is used to generate a beam of electron with typical energies of 1-20 keV. After the

generation, the electrons are accelerated and focussed onto the sample using a series of electrodes. Magnetic coils produce an interaction of mobilise charge with magnetic field. It is then used to manipulate the electron beam. By acting as a series of lenses, the coils focus the beam and the scan coils steers the sample across the sample afterwards.

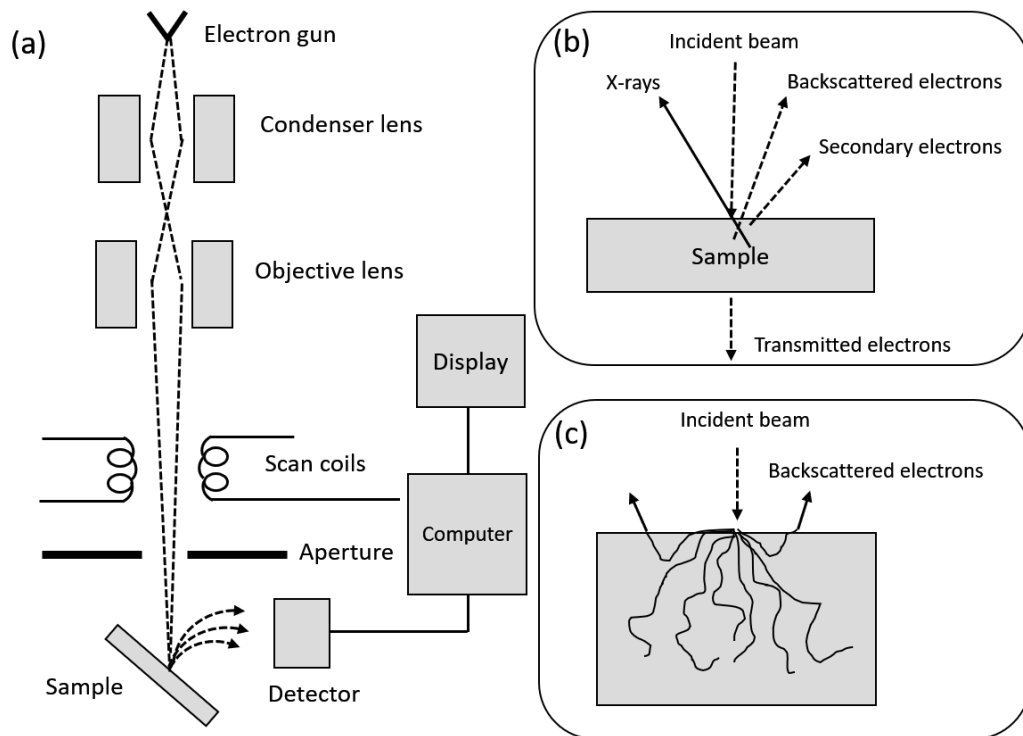


Figure 2-12: (a) SEM instrument schematic, (b) Mechanisms of SEM and (c) Illustration of the random excitation in the sample before primary excitation out from the sample.

A schematic for an SEM instrument is shown in Figure 2.12(a). Panel (b) shows SEM mechanisms when the electron beam hits a sample. The electrons may scatter either elastically or inelastically. Different number of waves emit from this mechanism such as backscattered electrons, secondary electrons and x-ray. This depends on the electron beam energy and density of the material. On the SEM

image, there are a number of contrast and imaging mechanism that can be determined by the detection rate of different types of emission when the electron beam is pointed to the corresponding point of sample. This probes various features and properties of the surface. SEM needs to be carried out in vacuum at pressures higher than $\sim 10^{-4}$ mbar because the electron beams can be readily attenuated by gases.

As mentioned above, there are various types of emission but the main type which is also used in this work is secondary electron emission. Secondary electrons which have low energy emerge from the sample when the incident electron beam collide with the sample. These secondary electrons are accelerated to the detectors through a positive potential to provide an image. Note that, in this mode the main contributor to the image contrast is surface topography. To obtain several high magnifications of the sample, backscattered electrons [63] were used as it had higher energy than secondary electrons. The sample is tilted to 70° relative to the electron source, and a phosphor screen at 90° placed near the sample [64]. Some of the incident electrons are inelastically scattered backwards by the sample, and some of these scattered electrons are incident on atomic planes at the sample surface that satisfy Bragg conditions. Because the energy loss during the inelastic scattering is small (15–25 eV), the wavelength is considered to be unchanged. However, the electrons are now incoherent, and so after diffraction they form Kikuchi bands rather than diffraction spots on the phosphor screen. The angles between Kikuchi bands is measured (usually through a Hough transform) and compared with reference angles for the specified material. In this way, the crystallographic structure is measured at that point and a map of the structure is produced by rastering the beam. All work in this thesis use Zeiss Supra and Gemini in Warwick Microscopy Facility.

2.5 X-ray photoelectron spectroscopy

X-ray photoelectron spectroscopy, (XPS) is one of the surface spectroscopy methods to determine the chemical composition of the surface. A surface is illuminated with monochromatic x-ray to excite the electron into the vacuum from its ground state. The kinetic energy of the photoemitted electron can be measured to determine the binding energy. From the analysis of binding energy, the sample composition and electronic structure of the surface can be acquired.

In order to excite an electron from the atoms, the photon energy of the x-ray must be higher than the binding energy of the electron to the nucleus. By rearranging the Koopman's theorem below,

$$E_k = \hbar\nu - E_b - \phi \quad (2.11)$$

where E_b is the single electron binding energy and ϕ is the work function of the sample.

The kinetic energy of the electron can be determined since $\hbar\nu$ is the photon energy of the x-ray, E_k is the kinetic energy that the photoemitted electron possess, and ϕ is the work function of the sample which differs according to the sample.

This theorem is an over simplification as the model is never observed because there are two relaxation process that takes place. First relaxation is the recombination of the excited electron to the lower energy state because the nucleus becomes more positively charged, thus creating stonger electron affinity. As a result, intra-atomic relaxation potential is induced.

Second relaxation is the inter-atomic relaxation which occurs with the conduction electron. In metal particularly, the mobile conduction electrons acts as

to reduce the change in potential observed by the core electrons. Therefore, a more reliable description of photoelectron energy can be deduced as below

$$E_k = \hbar\nu - E_b + E_a + E_r - \phi \quad (2.12)$$

where E_a is the intra-atomic relaxation energy and E_r is the inter-atomic relaxation energy. The value of inelastic mean free path (IMFP), together with $\lambda(E_k)$ of electrons give rise to surface specificity in XPS. IMFP which usually vary between 5 and 30 Å is calculated using the TPP-2M equation derived from Tanuma, Penn and Powell [65]. The spectra that is produced contains several peaks and the peak areas can help determine the surface composition. Several factors have to be taken into account when analysing the spectra such as the scan dwell time (D_s), the number of scans (n_{scan}), the atomic sensitivity factor (a_{asf}) and the probing depth, which depends on $\lambda(E_k)$. The area under the peak, A^P is given by

$$A^P = \int C(z) \exp\left(\frac{-t}{\sin \theta \lambda(E_k)}\right) dz \quad (2.13)$$

where $C(z)$ is the elemental concentration profile in the surface region, t is the thickness of the surface and θ is the take-off angle (TOA) relative to the surface plane. The scans will be more sensitive to the surface if the TOA is decreasing because the probe is decreasing as well. This effect is very significant during the studies of sub-monolayer deposition or segregation. Fundamentally, this model is reliable to determine the concentration profile, but this is undeniably time consuming and will produce a very rarely unique solutions. Therefore, another assumption has been made, which is $C(z)$ is constant so $A^P \propto \lambda(E_k)$ and the normalised intensity I^P , can be defined as

$$I^P = \frac{A^P}{a\lambda(E_k)D} \quad (2.14)$$

where a is the atomic sensitivity factor for the core level, and D is the total dwell time per point in the scan region. A^P is obtained from peak fitting software after substraction of an appropriate Shirley background [66]. From this assumption, the peak area ratios can be taken and a first approximation of the surface chemical composition can be determined.

However, this assumption is not always applicable in every situation. In such situation, XPS experiments can provide an insight on the concentration profile. The concentration profile strongly affects the area of the peak, being a direct measure of the number of atoms present in the surface region. It is possible to simulate appropriate structures and calculate concentration profiles for these; however, this is time consuming and results in non-unique solutions.

In this work, all XPS data shown were acquired from the Science City XPS (Omicron GMBH) located at University of Warwick using a monochromatic Al K_{α} source with approximate excitation energy at 1486.6 eV. CasaXPS fitting software [67] was used afterwards to analyse all data. Each sample was loaded to preparation chamber and experienced an argon sputtering for removing potentially carbon contamination due to atmosphere exposure. The lowest energy argon beam was used to minimise chemical damage to the underlying material.

2.6 Raman spectroscopy

Raman spectroscopy is a technique based on inelastic scattering of monochromatic light usually from a laser source. Inelastic scattering means that the frequency of photons in monochromatic light changes upon interaction with a sample [68]. Photons of the laser light are absorbed by the sample and then reemitted. Frequency of the reemitted photons is shifted up or down in comparison with original monochromatic frequency, which is called the Raman effect. This technique illustrates the reflection of electron-phonon interactions and electronic structure evolution [69]. Diverse investigations have been undertaken with a view to determine the reason why graphene has a 2D peak. As a result, different techniques have been proposed by different researchers. 2D double peaks present in graphene are crucial in this experiment since they can be used in optically determining the charge density through the behaviour of peak split decrease in correspondence to an increase in the charge density. In addition, the G-band shifts with charge can be used in determining the fluctuations of charge density. 2D are associated with the outer and inner Raman scattering processes [70]. Electronic bands evolution technique has been the most neglected, which evaluates the number of layers of graphene film formed.

The change in excitation energy has a significant impact on the peak changes. In a similar manner, the double resonance (DR) process, which operates by linking vectors of the phonon wave to the structure of the electronic band [71], also impacts peak changes. On the other hand, Raman scattering works within DR which is a fourth order process comprising of four main virtual transitions. These include electron-hole pair laser-induced excitation, electron-phonon scattering both having exchanged momentum near to the symmetrical point and away from

the point of symmetry, K, and recombination of the electron-hole. The conservation of energy in these transitions is vital for reaching the DR condition [71]. This technique is able to differentiate 1 to 5 layers clearly, based on the 2D/G band ratio. Raman spectra in this study is measured using Renishaw inVia Reflex at 532 nm with 50X objective. Extreme care is taken to avoid sample damage or laser induced heating. Different spots are taken to get the average of the surface that covered with expecting graphene after CVD growth.

2.7 Bulk magnetometry

In this work, bulk magnetic properties of MnSb films have been characterised by superconducting quantum interference device (SQUID). SQUID magnetometer has a superconducting ring containing two junctions known as Josephson junctions. Both of the junctions are made from thin insulating layers. One of the two branches of the ring is exposed to the magnetisation of the sample. The Josephson junctions has resistance that can be measured by manipulating the size and sign of the magnetisation of the sample.

With regards to this work, hysteresis loops of MnSb is obtained using SQUID technique and sample magnetisation that varies with temperature is acquired using SQUID technique.

Chapter 3: Pre-growth Substrate Preparation

3.1 Introduction

In this chapter we optimise Cu substrate preparation for graphene growth in CVD. Many attempts have been made to understand the growth mechanism of graphene since it was first published in 2010 [72]. What we know about graphene growth is primarily based on empirical studies that investigate how to produce large grains of crystalline graphene [73]. Scalable production of graphene by CVD is practicable and suitable for industrial applications. The protocol for graphene growth in LP- CVD was reported in 2013 using low-cost Cu foil (0.025 mm thick) [38]. Using this foil had triggered some issues for overlayer MnSb experiment on MBE. Based on our own failed experiment, it shows the foil is not suitable for transfer in MBE. The sample holders in MBE are suitable for more rigid substrates and the flatness of Cu foil had compromised the RHEED in-situ measurement.

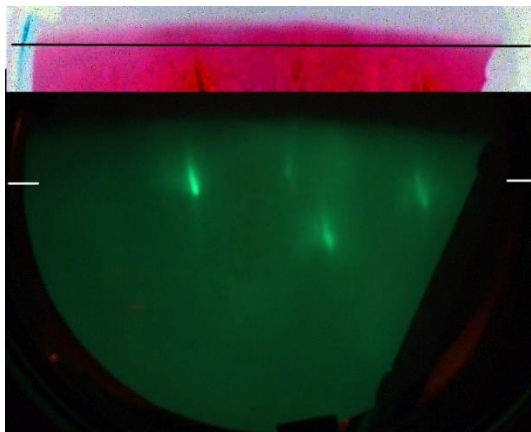


Figure 3-1: RHEED pattern for Cu foil mounted on MBE sample plate holder. Pink colour on the top highlights a contrast image of shadow edge with black line as a vision guide for eyes.

Figure 3.1 shows the RHEED pattern of Cu foil measured as in-situ in a MBE chamber. The difficulty of handling Cu foils for MBE is highlighted by the RHEED pattern shown in Figure 3.1, obtained from clean Cu foil after carefully mounting on an MBE sample plate, introducing to the vacuum system and preparing a clean surface by ion sputtering and annealing. The main RHEED screen photograph (lower part, green) shows clear diffraction features which can be associated with large Cu(100) grains in the foil. The diffuse nature of the streaks is due to the varying surface texture in the polycrystalline foils averaged over the electron beam footprint. However, it is also clear that the foil is not planar. The shadow edge of the RHEED represent the part of the screen obscured by the substrate itself. For a flat substrate such as a semiconductor wafer, this is sharp and straight. Non-planar features on the surface can be observed as silhouettes. The upper part of the image (pink) shows the section around the shadow edge (above the white dashes in the main image) after colour inversion and contrast enhancement. The black straight line can be used as a guide: it is very clear that the surface of the foil is not flat, even after the careful handling. Samples of graphene on Cu foil were also provided to a research group in Anan National College of Technology Japan (Prof. Shiro Tsukamoto) for attempted growth of GaAs and InAs by MBE. However, Prof. Shiro's group also reported practical difficulties with the thin foils. Hence thicker and more robust low-cost polycrystalline Cu substrates were investigated. To overcome this problem, we suggest using thicker foil (plate) with 0.25 mm thickness due to its rigidity and low cost (compared to single crystal). Product specifications and grain characteristics before growth for both foil and plate are explained in Table 3-1.

Table 3-1: Characteristics of two sets of commercial copper used in this study.

Copper / thickness	Foil , 0.025 mm	Plate , 0.25 mm
Purity (%)	99.8	99.99
Conductivity	High	High (Oxygen Free Free Conductivity)
Oxygen content	>5ppm	<5ppm
Annealed	Yes	Yes
Grain size	Typically mm	Tens to 100s um
Texture	Mostly Cu(100) with smaller (111) inclusions	Mixed orientation
Rigidity	Soft and flexible	Half hard and rigid
Supplier/Reference Code	Alfa Aesar/46365	Advert Materials /1346112

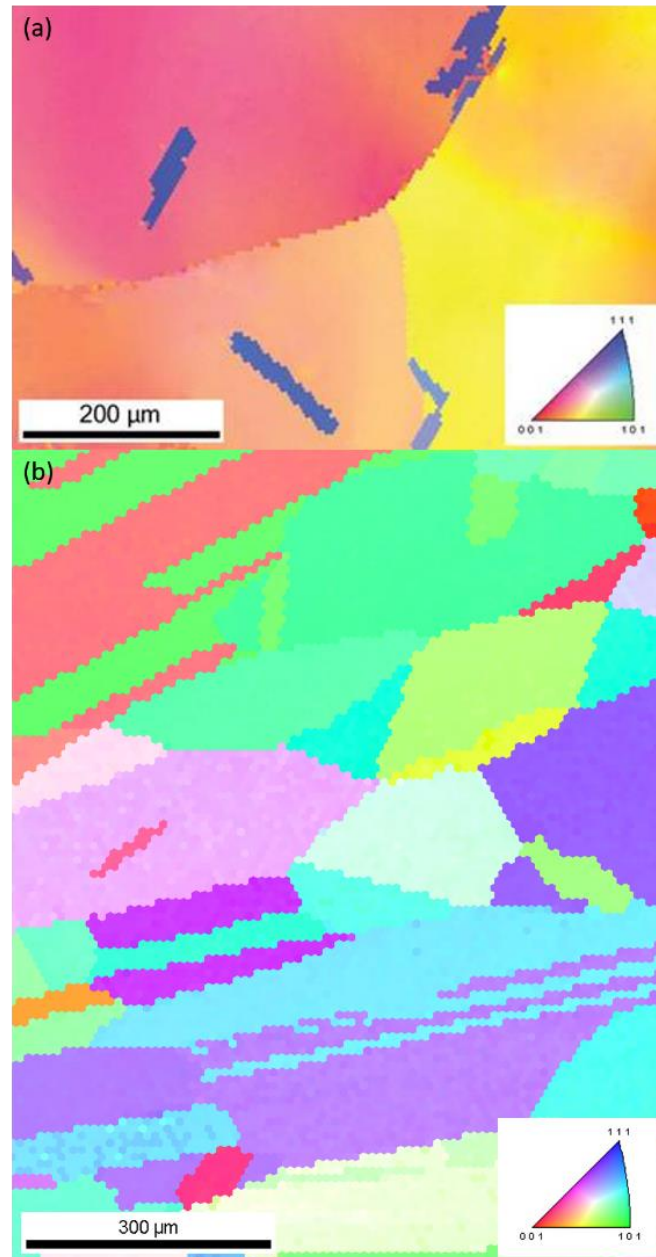


Figure 3-2: EBSD grain size texture (a) Cu foil, (Image adapted from [38]) and (b) Cu plate. Blue, green and red indicates (111), (101) and (100) grains respectively. Other colours represent direction that lie in between these grains.

Figure 3-2 shows the textures as measured by EBSD for both foil and plate. The image in 3.2(a) for Cu foil shows long grain boundaries between a large (100) grain (top left) and two non-(100) grains (lower left and right). Grains extend off out of the image are for several mm and most of the surface is close to (100) for this cold-rolled foil [38]. RHEED in Figure 3-1 also implies large grains because the beam footprint on the sample is several mm long. Inclusions of Cu(111) can be seen (blue) with dimensions of tens to $\sim 100\ \mu\text{m}$. By contrast, the Cu plate shown in Figure 3-2(b) has a much smaller grain size (tens to hundreds of μm) and a far wider variation of crystallographic texture. The smaller grain size is consistent with the supplier description of the plate as “half-hard”. This chapter will focus on pre-growth substrate preparation using Cu plate with Cu foil as reference.

3.2 Experimental details

The preparation for Cu foil is presented in Figure 3.3 (a). It consists of 2-steps, after which the foil is ready for graphene growth. The Cu foil wrinkles can easily be introduced by manual handling before the below procedures are applied.

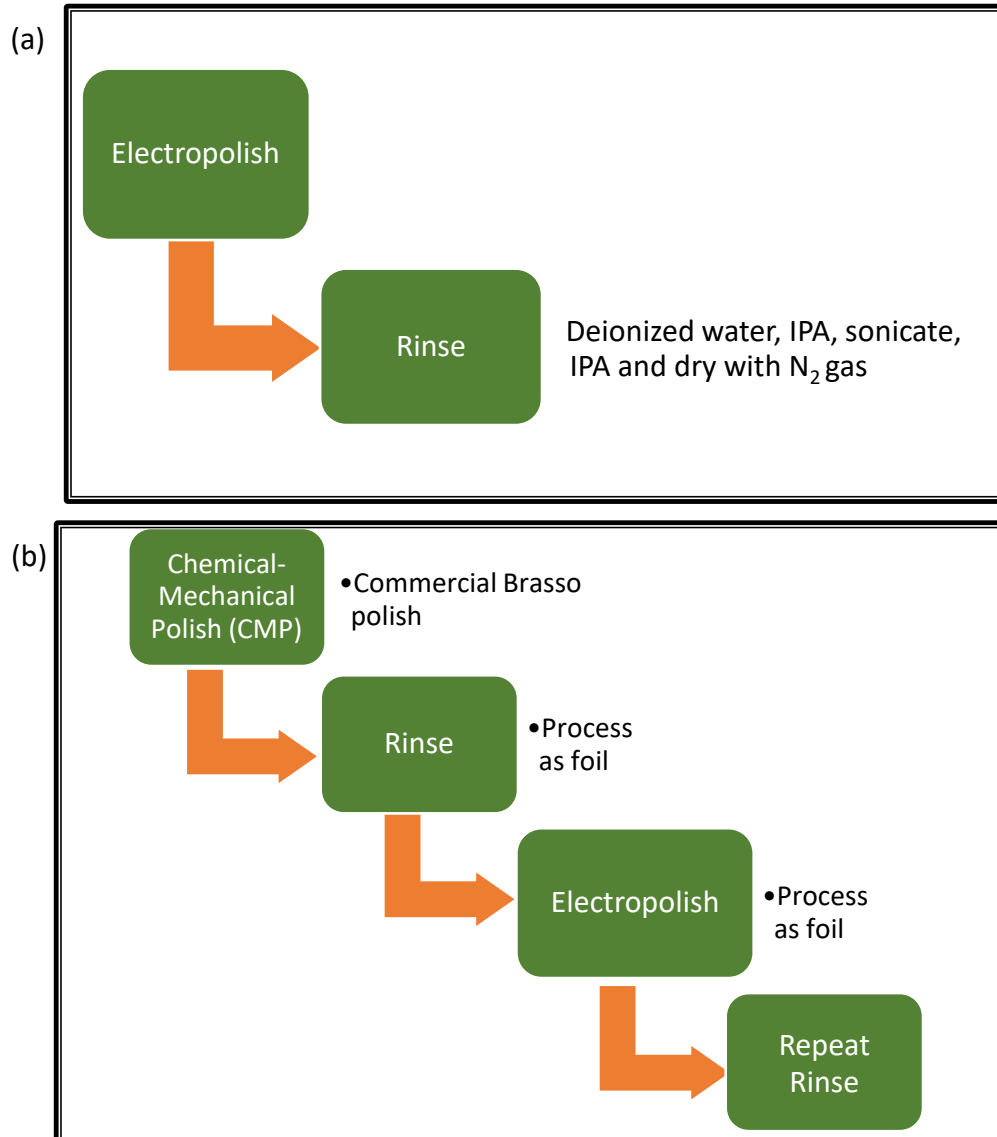


Figure 3-3: (a) 2-steps and (b) 4-steps preparation methods for Cu foil. Refer to Figure 3-4 for electropolish details.

For Cu plate, an extra chemical-mechanical polishing step was applied beforehand because the 2-steps process proved unsuitable. Figure 3-3(b) shows the additional steps. A commercial Brasso polish was found to be effective and

was applied evenly to the plate surface in small circular motions. It was left for a few minutes before buffing with a dry cloth. Cu plate had been rinsed using the same procedure with foil. After these extra steps, Cu plate went into an electrochemical solution with 3 different electrochemical etch times (10 s, 15 s, 20 s) and then rinsed for the second time.

Figure 3-4 shows the electropolishing setup supported by crocodile clips, where the Cu foil/plate was placed into the solution. A large Cu plate was used as the cathode, the solution was 1000 mL of water, 500 mL of ortho-phosphoric acid, 500 mL of ethanol, 100 mL of isopropyl alcohol (IPA) and 10 g of urea. A Hewlett-Packard 6612 System DC power supply was used to supply constant voltage/current. The voltage had been set to a constant value between 4.5 to 5.0 V, the current quickly settled to constant value (~ 1 A) and it applied for 10 s.

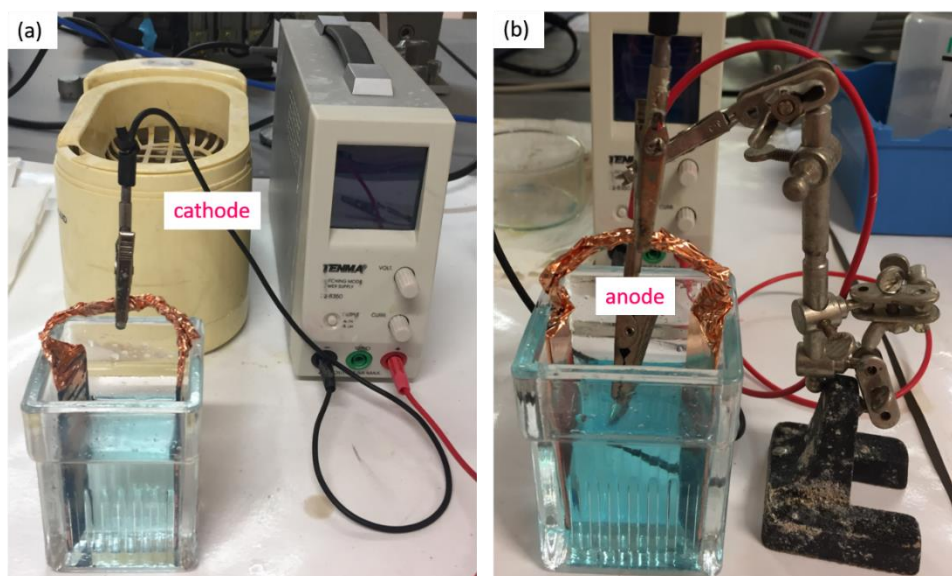


Figure 3-4: Electropolishing set-up for Cu foil/plate (a) large Cu cathode connected to negative terminal (black wire) of the power supply, (b) Cu foil/plate connected to anode (positive terminal, red wire) in the middle.

3.3 Results and discussion

We found the 2-steps substrate preparation was not a promising method to grow graphene in CVD. It has been challenging to achieve large graphene grains since it depends on reproducibly obtaining a clean copper surface free of adventitious carbon or other carbon sources before methane is introduced into the CVD system.

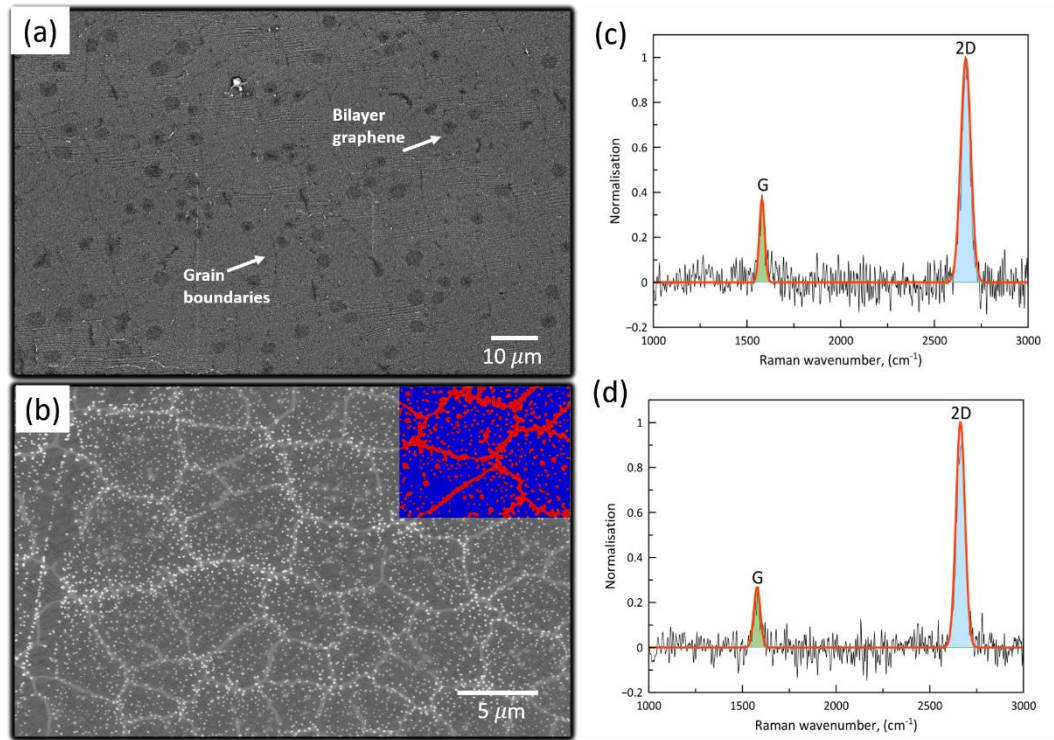


Figure 3-5: SEM images for 2-steps pre-graphene growth (a) Cu foil, (b) Cu plate, inset is a highlight of grain boundaries and impurity spots, (c) and (d) Raman spectrum for both Cu foil and plate respectively, red line is Gaussian fit.

Figure 3-5 shows the SEM images for both copper foil and plate with Gr growth. Panel (a) shows Cu foil with a full coverage of graphene monolayer and

bilayer confirmed with Raman peaks. Panel (b) shows many white particles and top right is the processing image to highlight the grain boundaries and impurity spots using MIPAR software. Thresholding was reliable for counting impurity spots. The thresholding value was adjusted to get the acceptable separation between the white spots but showed that more spots were mixed and became larger than the actual image. Therefore, manual counting was chosen to get the density. The impurity spots emanating from the Cu plate had a density of approximately $\sim 10.5 \mu\text{m}^{-2}$. The grain boundary in panel (b) has visible contrast but is also decorated by a higher density of impurity spots. As known from previous foil studies [38], the impurity spots originate as contamination where segregation occurred from bulk or surface itself. We did not do XPS for 3 reasons. Firstly, the spatial resolution is much higher than the impurity spot size. Our Kratos imaging pixel size is approximately $\sim 3 \mu\text{m}$ and therefore not useful for small particles. Secondly, C 1s is not distinguishable between graphene and adventitious carbon. Lastly the samples had been exposed to air while transported to XPS and the Cu had been oxidised. Panel (c) shows the Raman measurement. For single layer the ratio of 2D/G must lie in between approximately ~ 2 to 4 [74]. For Cu foil, the ratio is 2.66. It is higher in plate with 3.73 but still in the ratio range between 2 to 4. The Cu plate still has produced almost a full coverage of monolayer regardless of the higher density of impurity spots. On the other hand, bilayer patches are not cleared in the SEM due to the many impurity spots covering the image.

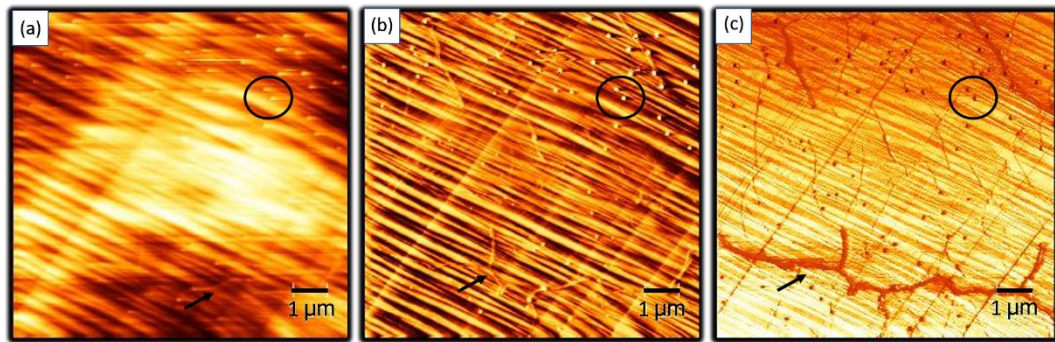


Figure 3-6: AFM topography for graphene on 2-steps prepared for Cu plate (a) topography, (b) vertical deflection and (c) horizontal deflection [Black circles highlighted impurity spots while arrows show a graphene grain boundary.

The AFM image in Figure 3-6 (a) shows the topography and two main features are visible. The stripy pattern from top left to bottom right is Cu faceting. Some discrete points can be seen at the top right corner and was identified as impurity spots, the black circles highlighted two of the spots. It presents similarly universal graphene growth on Cu foil and the RMS roughness was calculated approximately ~ 54 nm for $10 \times 10 \mu\text{m}$ image size. The RMS roughness for 2-step Cu plate is 5 times higher than Cu foil. In panel (b), it shows vertical deflection image as for short-range topography. The impurity spots now can be seen clearly as expected from SEM, faceting becomes very clear and the periodicity of facets is approximately $\sim 300 \mu\text{m}$. AFM probes a tiny area compared to the grain size in Figure 3-2(b) and it might expect different facet pattern might be expected on a different Cu grain. However, we conclude that structural feedback or faceting is not limited to thin foils. Facets are clearly visible with regularly orientated terraces and facets interspersed with smooth regions. The simultaneously acquired friction image shows that the facetted regions are associated with graphene [38].

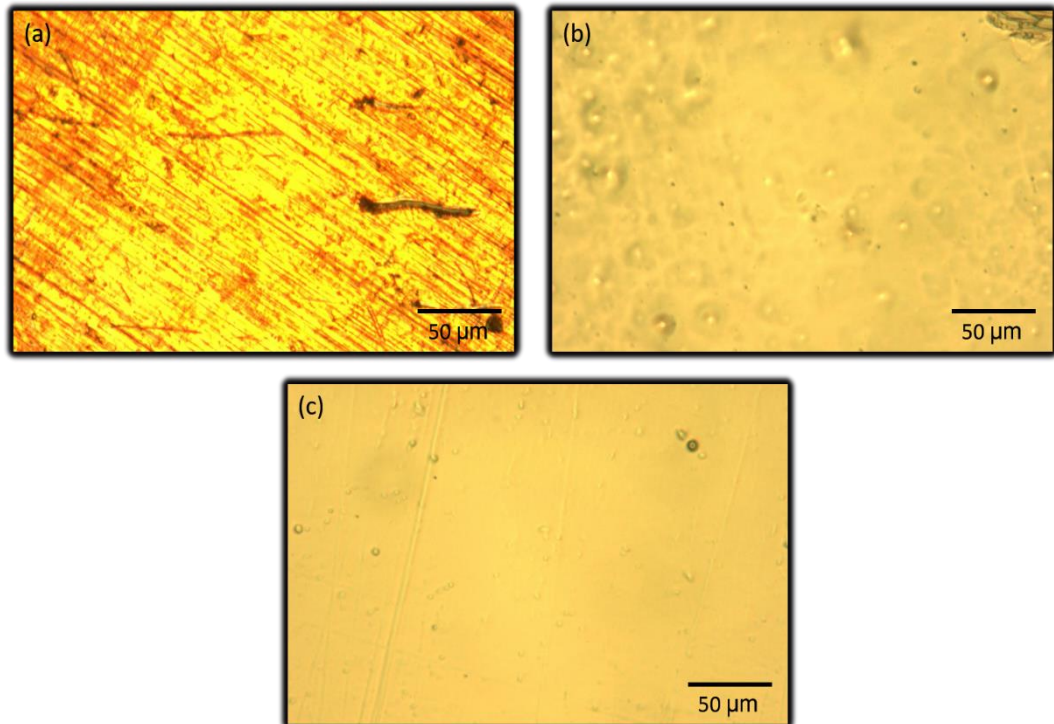


Figure 3-7: Reflected light microscope images for (a) Cu plate as purchased, (b) Cu plate after 2-steps and (c) Cu plate after 4-steps with 20 s electropolish.

The light microscope images in Figure 3-7 compares the Cu condition using the 2-steps and 4-steps method respectively. It displays smoother surfaces taken using the optical microscope at different stages of the cleaning of the copper plate. The CMP stage is needed to reduce the very high initial surface roughness and the likely surface contamination of the supplied Cu plate. To get the result in Figure 3-7(c), we tried 3 different etching time and represented in Figure 3-8.

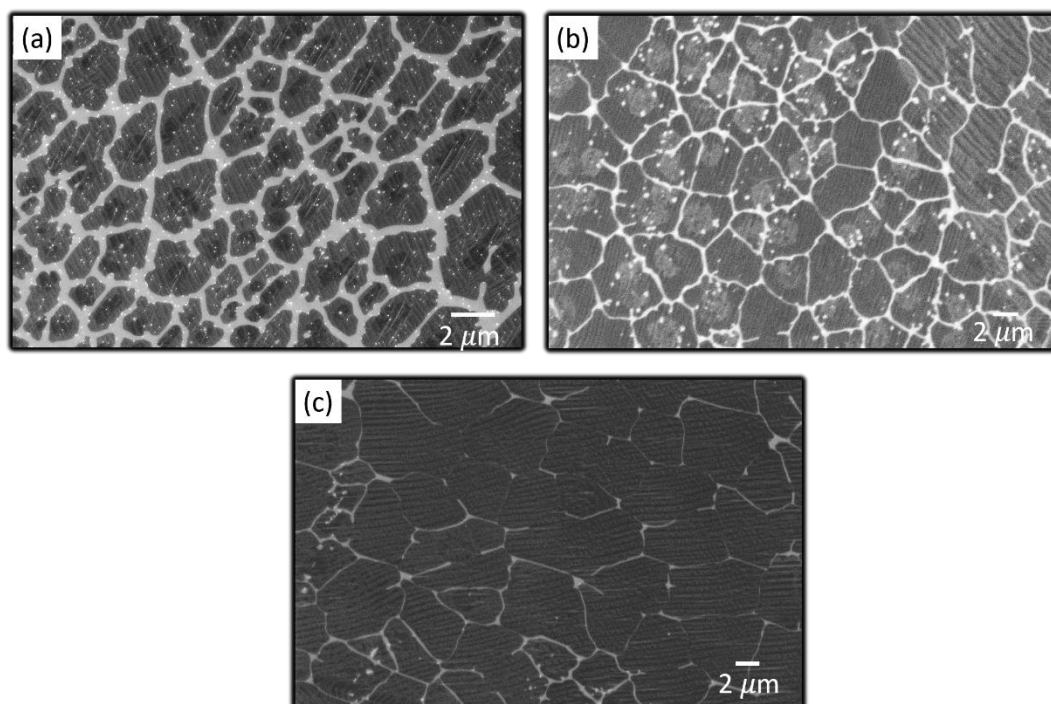


Figure 3-8: SEM images of Gr on Cu plate after 4-steps substrate preparation with (a) 10 s , (b) 15 s, and (c) 20 s electropolishing time. Growth condition for this study is 20 mins anneal with 5 sccm H_2 at 950 °C, 30 mins growth time with 10 sccm H_2 and 3 sccm CH_4 and cooling to 600 °C with 5 sccm H_2 and 2 sccm CH_4 .

Figure 3-8 shows the post-growth graphene on Cu plate with different electropolishing time. Initially, if the electropolishing stage is maintained for 10 s, the graphene growth was found to be poor and showed white spots of contamination. These impurity spots decreasing by time is showed in Table 3-2. By manually counting the impurity spots, we found that the density of impurity spots decreased over time. Even after 20 s, we can still see patches of higher impurity density but compared to area in μm^2 , the spots can be suggested as negligible to the Cu plate. We also tried 30 s and 40 s electropolishing time, but the Cu plate

colour changed. This may be due to over exposure to the electrochemical solution. Whatever the cause, the surface conditions looked unpromising compared to 20 s. Therefore, we decided not to carry on longer than 20 s.

Table 3-2: Summary of electropolishing time vs area density of spots.

Electropolishing time (s)	Area density of impurity spots (μm^{-2})
10	2.12
15	0.25
20	0.03

3.4 Summary

The study in this chapter is motivated by the transfer of a sample to MBE. A rigid substrate is needed to overcome the foil limitation. Foil tends to wrinkle and unflatten after spot-welding on MBE substrate holder. Cu foil has soft and flexibility while Cu plate is a half-hard rigidity. EBSD confirmed that Cu plate has a mixture of grain size in between (x01) and (x11) directions. Polycrystalline Cu plate is still cheaper compared to single crystal. Cu plate had been tried as treatment like foil, but the surface preparation steps needed to modify by adding CMP otherwise high density of impurity spots appeared. We got a good preliminary result for graphene growth as explained in Raman spectrum. With a Cu plate we achieved almost full coverage of monolayer graphene without any compromise in quality. We also observed faceting on the Cu plate and proved that structural feedback was not limited to thin foils. More detailed characterisation of graphene on Cu plate follows in the next chapter.

Chapter 4: Graphene on Cu plate

4.1 Introduction

Chapter 3 showed the necessary surface preparation steps for Cu plate for graphene growth. In this chapter, the growth process for graphene on Cu plate by CVD is investigated. The properties of grown graphene studied include grain size, bilayer coverage, elemental composition and surface roughness. This study aims to enlighten differences and similarities to the growth of graphene with Cu foil. The findings contribute to a better understanding of the underlying growth mechanisms for CVD growth of graphene on 4-step-prepared Cu plate.

4.2 Experimental details

Cu plate was prepared using the 4-step method in Chapter 3. Graphene growth was performed in CVD as described in Chapter 2, varying anneal (flowing H_2) and growth (H_2 and CH_4) times, with everything else fixed and constant. CVD growth protocol, unless stated otherwise, was conducted as follows: the sample was placed in the centre of the furnace and heated to 950 °C with ramp rate showed in Table 4-1 at $\sim 2 \times 10^{-2}$ mbar H_2 and annealed for 60 minutes while maintaining the H_2 partial pressure. The hydrogen flowed continuously until the temperature reached 950 °C and CH_4 was introduced into the chamber to start the graphene synthesis. The growth pressure recorded approximately 5×10^{-2} mbar. The chamber was then cooled to 600 °C with H_2 and CH_4 flowing. After reaching this

Table 4-1: CVD growth parameters.

Ramp	Anneal	Growth	Cooling
15 °C/min	950 °C, H ₂ 5 sccm	950 °C, H ₂ 10 sccm, CH ₄ 3 sccm	600 °C, H ₂ 5 sccm, CH ₄ 2 sccm
6 s time step	10, 15, 20, 25, 30 min.	10, 20, 30 min.	-

temperature, the furnace was turned off and left to cool down to the room temperature.

In Table 4-1, the heating conditions for the ramp, anneal, growth and cooling processes are shown. These parameters are based on the Cu foil experience and were justified in Chapter 2.

4.3 Results and discussion

Table 4-2 shows a detailed sample set for growth optimisation. SEM images were obtained for all of these samples, but the other techniques were only employed for a sub-set of these. Table 4-2 represented 40 minutes growth time, which produced a very similar morphology to 30 minutes growth time which is not reported in detail here. It shows self-limiting graphene growth where growth rate slows after 1 monolayer as explained in Chapter 2.

Table 4-2: Sample summary for CVD growth study.

Growth (min) \ Anneal (min)	10	15	20	25	30
10	SEM, AFM	SEM, AFM	SEM, Raman	SEM	SEM, AFM
20			SEM, AFM, Raman		SEM, AFM, Raman
30			SEM, XPS, Raman		SEM, XPS, Raman
40			SEM		SEM

Raman Spectroscopy was used in the experiment as it would help in the analysis of the 2D and G peaks of the graphene grown on Cu plate by characterising the position, change and relative intensity with the various layers of graphene. The Raman technique was applied using the Renishaw inVia Reflex measuring Raman Spectra at 532 nm with an objective lens of 50x. The measurement was recorded at multi-spot positions and moved around the whole sample typically to 10 different places. A set of 10 spectra was taken with effective spot size $\sim 100 \mu\text{m}$ and the laser power was kept to 1 mW to avoid over heating of the sample. The samples were measured under ambient temperature.

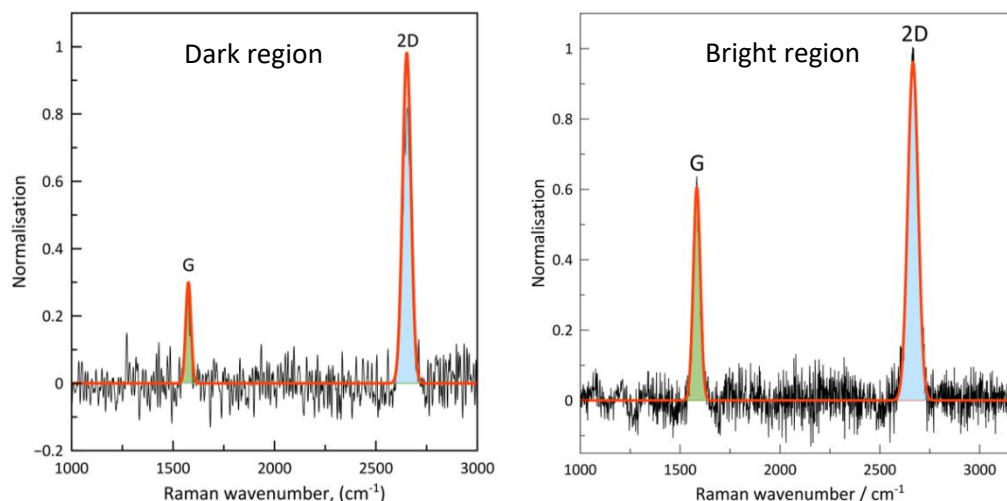


Figure 4-1: Raman spectra for graphene on Cu plate (30 min anneal and 20 min growth). Left panel indicates spectrum of dark region while right panel is bright region of the sample. Blue and green shaded areas represent Gaussian fit over a linear background (red lines).

Figure 4-1 shows the Raman spectrum for graphene on Cu plate with 30 min anneal time and 20 mins growth time. The right panel shows the measurement taken on the dark non-uniform flakes of the sample with the left panel showing measurements on the brighter area. A different area of image contrast was chosen to carry out the Raman measurement because the image contrast mechanism in the SEM normally detects darker regions at bilayer graphene while brighter regimes as a monolayer region [75]. This spectrum indicates that graphene on Cu plate had some bilayer patches with full coverage of monolayer.

In average 1 or 2 spots out of 10 shows almost the same peaks height as the right panel and the rest is similar with the left panel. The Raman peaks were fitted by a Gaussian line shape for analysis over a subtraction of a linear

background in predefined spectral ranges ($1500\text{--}1700\text{ cm}^{-1}$ for G band fitting, $2500\text{--}2800\text{ cm}^{-1}$ for 2D band fitting). Both the right and left panels shows normalisation values (y-axes) to simplify the different scales on peaks intensity to a notionally common scale. It is apparent that the G peaks on the right panel are higher than on the left. The 2D/G intensity ratio for the left sample is ~ 3.13 and is consistent with single layer graphene. In contrary, the right panel 2D/G ratio is around ~ 1.5 and lower than 2. The single layer differentiation must lie between approximately 2 – 4 ratios to enhance accuracy [71].

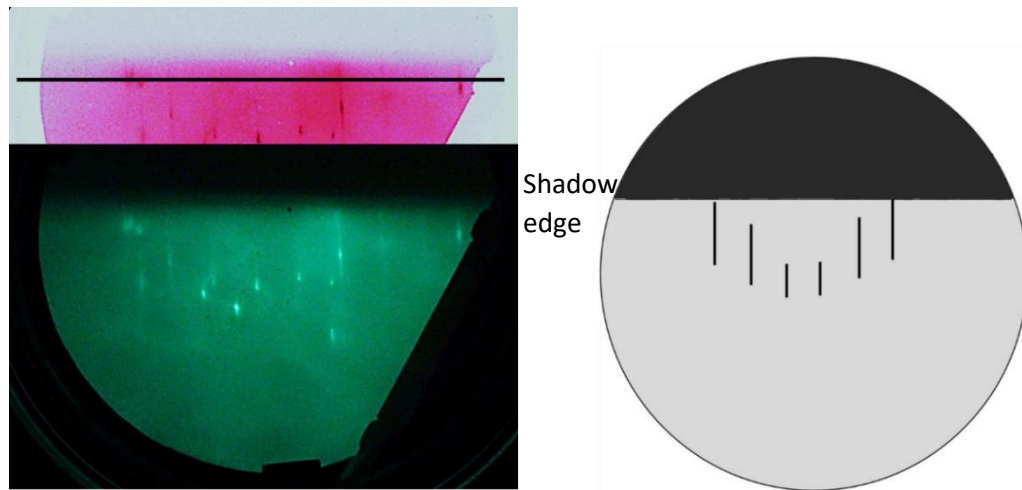


Figure 4-2: RHEED pattern obtained from Gr on Cu plate surface. The schematic on the right hand side of the figure highlights the streaks features of the pattern. Pink and white colours on the top left panel highlights a contrast image of shadow edge with black line as a guide for eyes.

Figure 4-2 shows a RHEED pattern from a sample that we annealed and grew for 30 and 20 minutes respectively. RHEED pattern was taken in MBE chamber after Cu plate was attached with spot-welded tantalum wire on the sample holder just before MnSb growth. The upper part of the image (pink) shows

the section around the shadow edge (above the white dashes in the main image) after colour inversion and contrast enhancement. The black straight line is a guide to the eye: it is very clear that the surface Cu plate is flat. The rigidity of Cu plate compared to the foil in Figure 3-1 shows a much straighter and sharper shadow edge. The highlighted streaks pattern is probably one zone of diffraction features from a large grain. We cannot reliably index either Cu or graphene since their lattice parameters are so similar. There are other streaks and spots from other grains with different texture which are Cu and/or graphene. Diffraction features change a lot as the sample is moved around parallel to the surface. Movement in the range of 50 microns produces a change. This is consistent with EBSD texture and Cu grain size are shown in Figure 3-2. These crystal grains are large and well ordered, enough to give surface diffraction but we cannot tell about the local epitaxy of graphene. Qualitative analysing using LEED has been carried out to observe the surface structure.

A LEED pattern of graphene on a Cu plate is shown in Figure 4-3 with two different areas (a) and (b) respectively. Area 1 at 67 eV shows a green and pink circle labelled with F1 and F2 as facet spots on a Cu surface whose normal is on a tilted Cu surface. These spots did not move when higher energies were applied to the sample. Confirmation with AFM results showed a faceted Cu surface. Three green spots labelled at 76 eV attributed to three orientations of graphene on the surface that is normal to the F1 spot. The separation at these two graphene domains is $11^{\circ} \pm 2^{\circ}$. The domains is Cu plates had a different starting texture compared to foil. Cu foil had two weak mismatch graphene epitaxy domains [38]. We propose that on Cu plate, graphene tried to find a stable orientation on a polycrystalline Cu feature as shown in Figure 3-2(b) and ended up with another structural feedback forming additional (100) + (210) Cu facets. The pink circles at

83 eV showed that the same reflection spots come from facet (F2) with a different surface normal but still had the same 11° separation angles between the two graphene domains. We detect two pairs of the same graphene domain represented by the pink solid line and dashed line and is presumably an incomplete hexagonal graphene pattern. The blue circles display minor facets of polycrystalline Cu. The artefact ring was not real as it came from the channel plate of the LEED system. Figure 4-3(b) shows another area of the same sample. The third facet spots have been identified and labelled as F3 (yellow circle). As this sample was very polycrystalline, the facet spot appeared randomly and resulted in the graphene spots as normal to the facet spot. The yellow solid line confirmed the separation angle between three graphene domains was 11° . All graphene spots related to the normal of F3 were indicated by a yellow solid line. Cu plates has different starting texture compare to foil. It presumably influenced three graphene domains formed on the surface. Graphene is tried to stretch and find the most stable orientation and formed mismatch epitaxy. All features in Figure 4-3 were consistent with weak mismatch epitaxy angle in Cu foil [38] reported as $\pm 16^\circ$ and they do not correspond to any simple epitaxial match. In addition, graphene on Cu plate displays no graphene ring compared to Cu foil.

Facet spots were identified by monitoring spot movement with beam energy and were easy to observe due to their constant position on the screen as the electron energy was changed. Although different, weaker facet spots were often observed, the dominant facet spots were always oriented $11^\circ \pm 2^\circ$ away from the surface normal (00) beam. Primary orientation of the surface is a mixture of polycrystalline Cu plate hence we cannot deduce any direction based on LEED patterns.

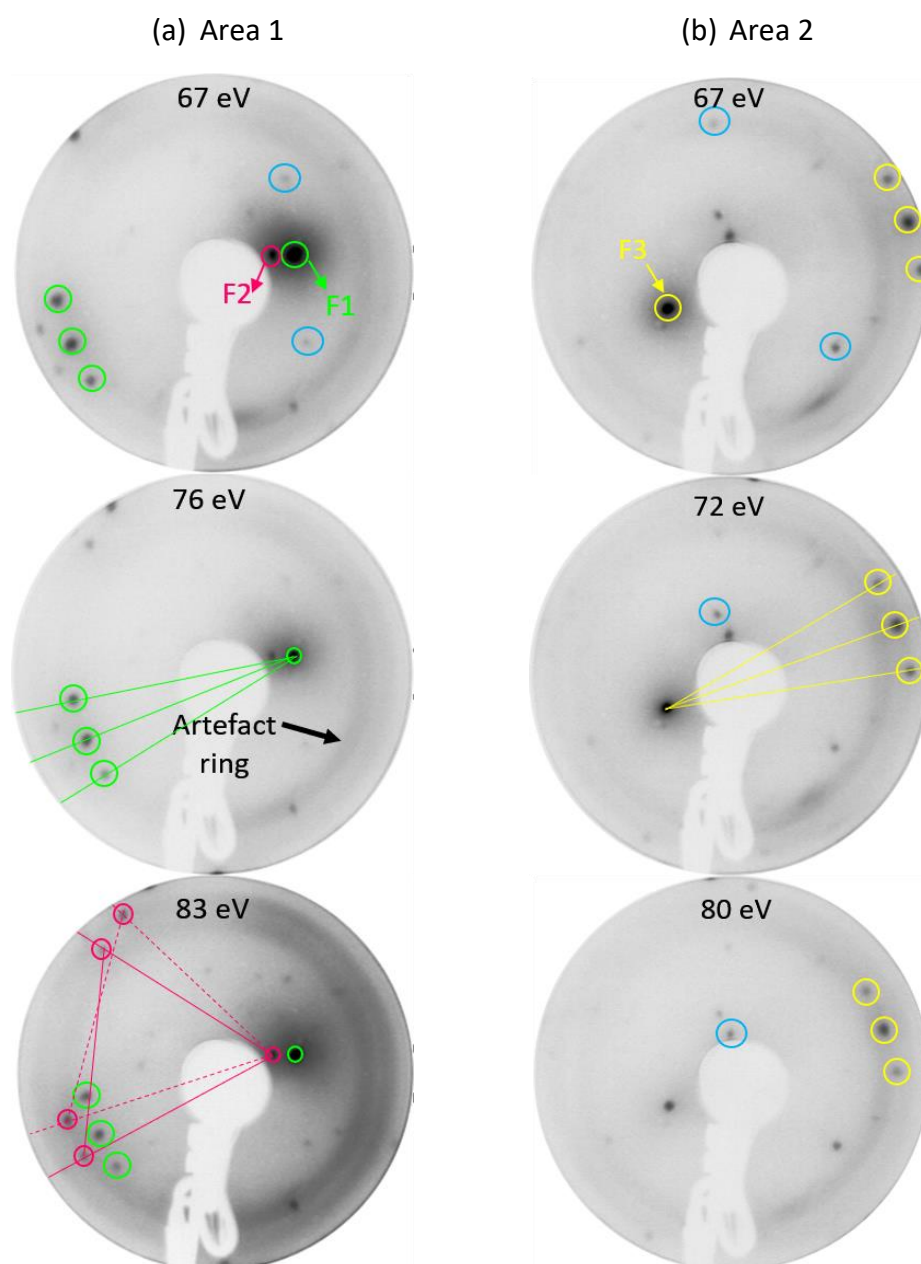


Figure 4-3: Electron diffraction obtained from a clean graphene on Cu plate surface showing two different areas of scan (a) and (b). The electrons energy are 67 eV, 76 eV and 83 eV of LEED pattern respectively. F1 (green), F2 (pink) and F3 (yellow) are facet points. Green, pink and yellow straight lines indicate graphene domains related with its own facet points respectively. The smooth arc in these imaged labelled 'artifact ring' is an artefact of the channel plate LEED screen.

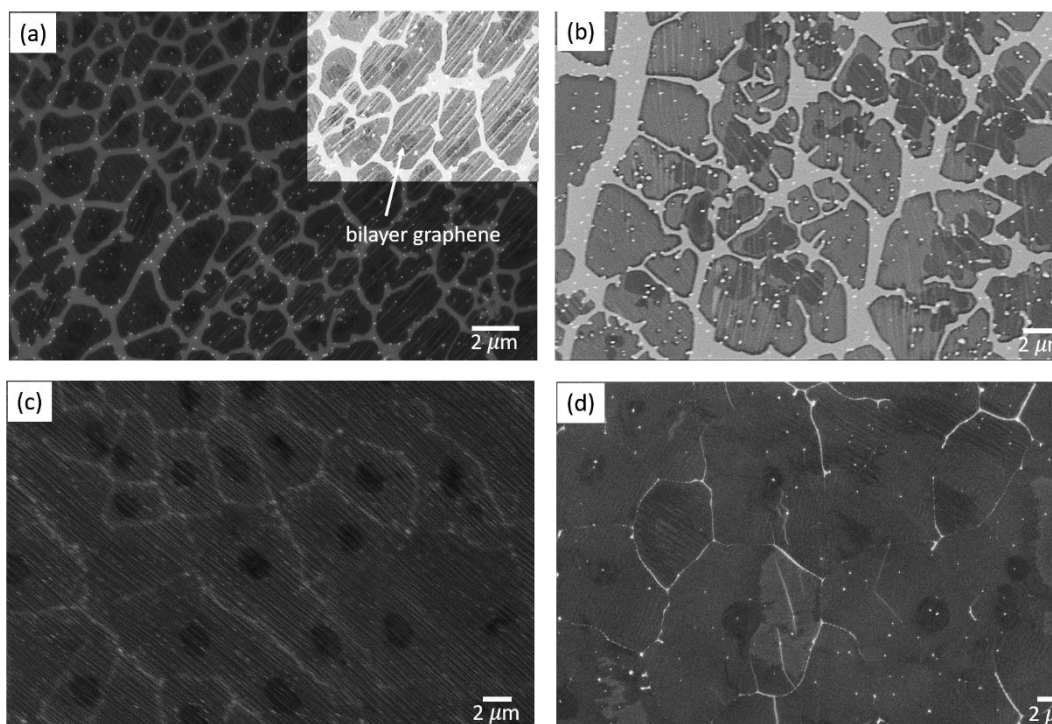


Figure 4-4: SEM images for 10 mins growth time and anneal at 5 sccm of H_2 (a) 10 mins, extra panel highlighted white region and impurity spots, and dark non-uniform flakes as bilayer graphene (b) 15 mins, (c) 20 mins and (d) 30 mins.

Figure 4-4 shows SEM images at different anneal times with a constant 10 minutes of growth time. All other parameters are the same as indicated in Table 4-1. Panel (a) highlights a 10 mins anneal with partial coverage and area density of impurity spots obviously scattered in between bright and dark regions. Impurity spots were grown preferably along and in the area of the Cu surface (bright region). The bilayer of graphene was located at almost each domain of the graphene grain. This typical SEM image displays most of the graphene on Cu plate features. The change of colour contrast in the optical image suggests a variation of graphene film thicknesses because the light interference on SiO_2 layer is

modulated by the graphene layers [76]. To overcome the low spatial resolution due to the diffraction limit of light in optical image, the SEM technique can be utilised with digital image processing [77]. As shown in panel (a), the background colour is graphene monolayer partially covering the Cu surface excluding the bright network region (bare Cu) as incomplete growth. Ten minutes of anneal time is not sufficient to reduce nucleation density through producing a uniform surface prepared for catalytic decomposition of the carbon feedstock. The subset image in (a) shows the image enhancement for sharper and brighter features as grown. From the subset image, those white, narrow stripes in the graphene region are typical Cu facets after graphene growth. This is because faceting is produced due to the restructuring of the copper underneath these regions into steps [38]. The darker spot regions indicate graphene with multilayers, Raman spectroscopy (Figure 4-1) has confirmed this as bilayer graphene. The secondary electrons intensity coming from graphene depend on the number of layers and represent as different contrasts in SEM digital image. The brightness decreasing can be associated to monolayer and bilayer graphene respectively. Weak interaction between graphene and Cu resulted in many difference domains of graphene islands as shown on panel (a). Panel (c) and (d) displayed longer anneal times and full coverage of graphene growth apparently can be seen. Impurity spots were decreased, and graphene grain size started to grow bigger. Since growth time was set at only 10 minutes, we still can see the impurity spots appearing at an average size of less than 200 nm. Our annealing study on Cu plate indicates that the area density of impurity spots strongly depends on the time taken. As anneal time lengthens, Cu plate surfaces became smoother incorrelating to other features such as wrinkles and facets.

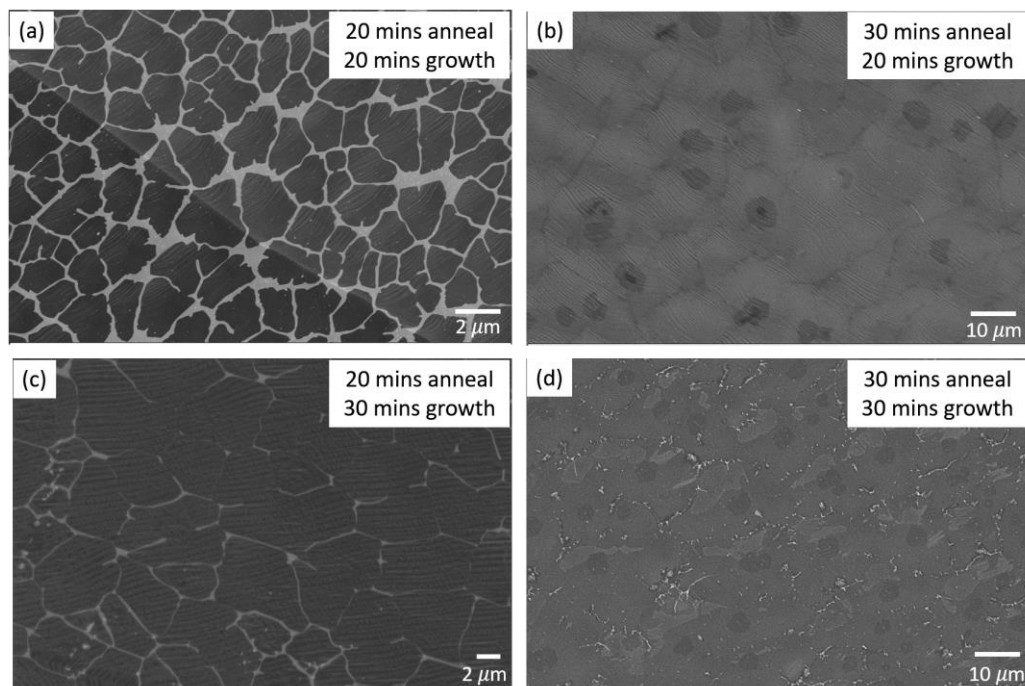


Figure 4-5: SEM images for longer growth time (a) 20 mins anneal, 20 mins growth, (b) 30 mins anneal, 20 mins growth, (c) 20 mins anneal, 30 mins growth, (d) 30 mins anneal, 30 mins growth.

Figure 4-5 shows SEM images of four different conditions of growth. Panel (a) and (c) both experienced 20 mins of annealing but different growth times, 20 and 30 mins respectively. While panel (b) and (d) both have the same 30 mins annealing time and 20 and 30 mins of growth time. Panel (a) displays partial coverage and it is not good for MBE overgrown which will be reported in Chapter 5. The anneal time was applied two times higher than Figure 4-3 and proved no impurity spots appeared. Apparently, with longer growth time but similar anneal time in panel (c), a bare Cu (bright network areas) was decreased and presented better coverage compared to (a). For the longer anneal time in panel (b), full coverage developed with some darker spots of bilayer graphene. With a manual count, the monolayer graphene covered more than 90% of the sample. Some of

the smaller islands in (a) and (c) have grown, but it dissipated at higher coverage in (b) and (d). It can be suggested that the small islands can be etched away when the initial nucleation density is higher than the density of grains when it experienced almost full coverage of graphene. For 30 minutes growth time in (d), it demonstrates more bilayer coverage compared to (c). Bilayer graphene actively exists in this sample due to the reaction of carbon atoms lying directly onto current monolayer graphene and its stacked. Quantitative analysis of SEM data was performed to obtain the impurity spot density and graphene grain size. They are plotted in Figure 4-6 and 4-7 respectively.

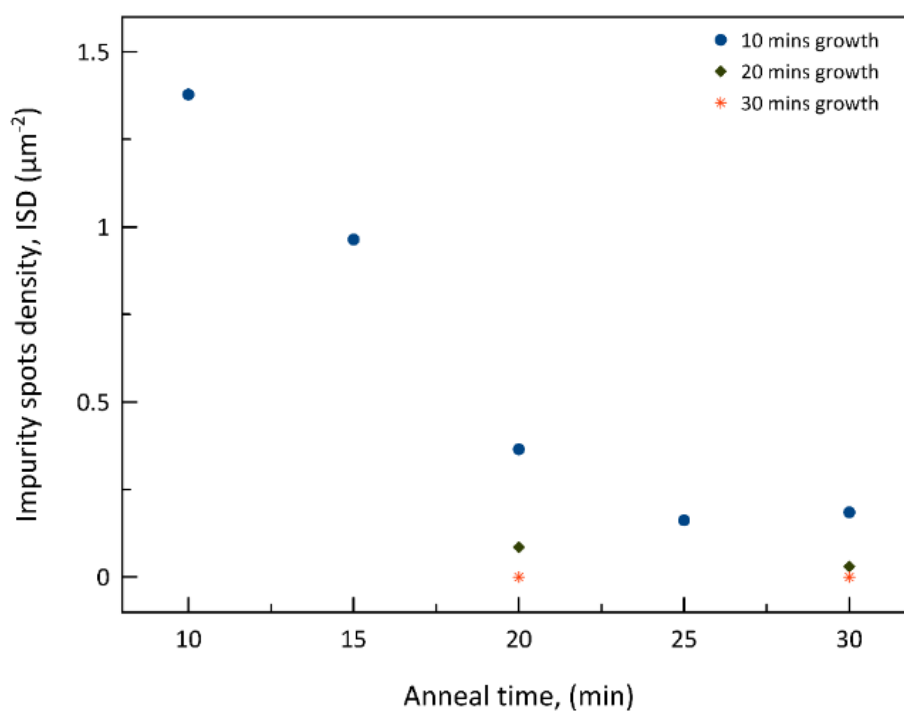


Figure 4-6: Area density of impurity spots vs anneal time from SEM image.

Figure 4-6 shows the area density of spots in the sample compare to anneal time. Impurity spot density, ISD decrease with anneal time for low growth time. At high anneal time however, ISD is smaller for longer growth time. Both growth and annealing suppressed ISD and made a good and clean graphene. ISD represented in the SEM images normally in bright region, with high magnification (subset image in Figure 4-3 (a) we can identify the contamination spots compared with bare Cu. The bare Cu bright network are normally connected to each other due to incomplete growth of graphene layers. ISD appeared probably as a matter of adsorption from tube contamination. The Cu plate has a larger volume of Cu and it may have cross contamination by heterogenous particles deposited in the quartz tube.

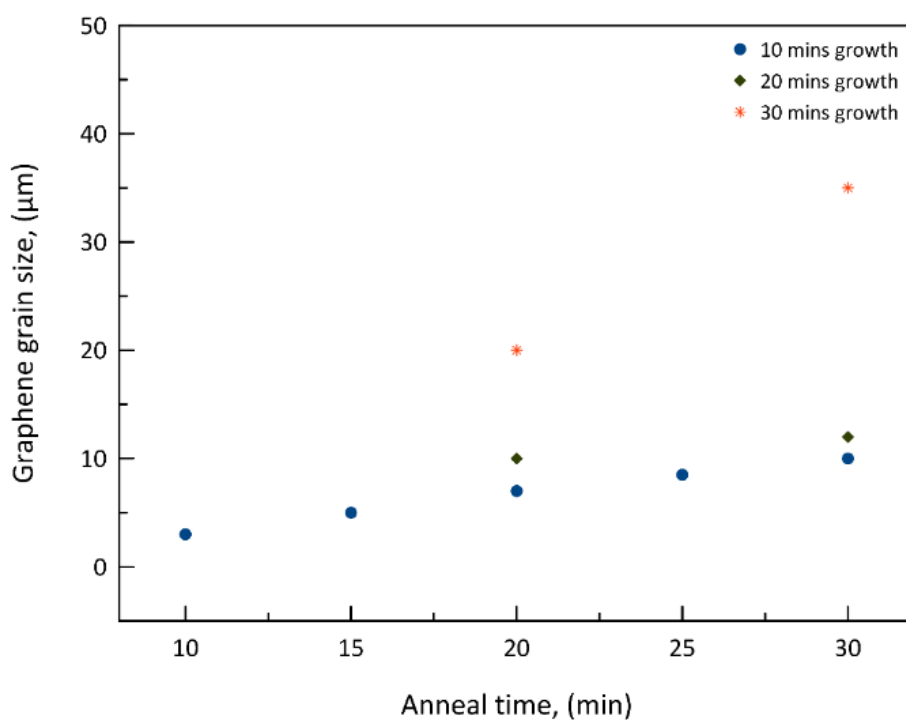


Figure 4-7: Graphene grain size vs anneal time from SEM image.

Figure 4-7 represents graphene grain size correlated with anneal time. It has been processed using MIPAR software and average grain size for graphene on Cu plate approximately up to 40 μm depends on the anneal time. Our Cu foil study [38] confirmed the grain size was between 50 to 100 μm . Island sizes were produced differently depending on the nucleation density and growth rate of islands which were determined by the flow of hydrogen and methane. As the small ratio of H_2 and CH_4 had been used, we confirmed that it can prevent higher nucleation density of graphene grains as reported in our Cu foil paper. We can see more nucleation sites on Cu plate as the Cu grain size looks smaller than the foil (Figure 3-2). As matter of fact, the ratio of gas flow was consistent in this study, hence graphene grain size is likely influenced by the heterogeneous nucleation where the adatoms get stuck at a defect.

AFM measurements were undertaken in order to examine the surface roughness of the graphene on Cu plate. As such, the measurements would help distinguish the grain boundaries and steps through high resolution scanning and in effect, facilitate in the analysis. Figure 4-8 below displays the results of the AFM measurements.

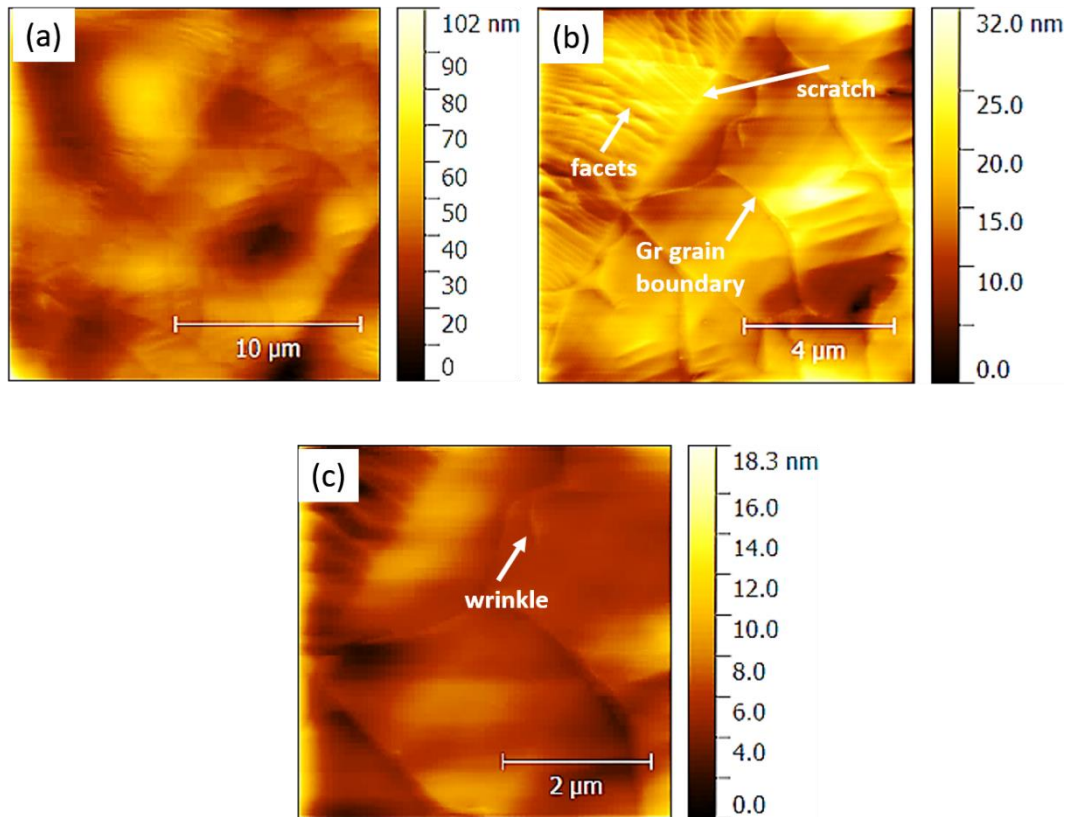


Figure 4-8: AFM for 15 mins anneal and 10 mins growth with different image size respectively (a), (b) and (c).

The first observation to be made from the results in Figure 4-8, is the difference in the image panel sizes as illustrated by the different sized scales. The panel (a) image size is 20 x 20 microns with height scale 0 - 102 nm, (b) is 10 x 10 microns with height scale 0 - 32 nm and (c) is 5 x 5 micron with height scale 0 - 18.3 nm. As the different scales decreased, less of the surface and more of the wrinkle features were seen. In Figure 4-8 (a), the AFM image is on a large-scale with RMS roughness 9.60 nm of Cu substrate. The appearance of facets was ambiguous but clearly the narrow lines as graphene boundaries with 4 to 5 μm can be detected. In Figure 4-8(b) and 4-8(c), facets are clearer and grain boundaries feature (lower right). These were observed in the AFM image as a result of the

chemical combination of the grown graphene. In (b), there is a straight feature that possibly occurs because a polish scratch happened during substrate preparation as explained in Chapter 3. The RMS roughness value indicates the mean from different scanning areas on the sample. The facets and grain boundary features were formed as a result of the graphene electronic properties (a major characteristic of semiconductors). The LEED pattern in Figure 4-3 shows that faceting happened on graphene thin film as well, the facet spots did not move with energy and the reflection of graphene spots appeared as normal to the facet spots.

The results from the AFM process (Figure 4-8) were observed to be similar to those attained when depositing multi-layer graphene films on a Si substrate as reported by Lin et al. [78]. The wrinkles formed on the graphene on Cu plate surface in association with a thermal expansion coefficient difference are identified to be crossing the grains of Cu boundaries which indicates continuous growth of the film [79]. For example, Figure 4-8 (c), clearly shows the presence of wrinkles, flakes, and facets. Graphene growth, in this case, has varied thicknesses hence yielding the same structure of graphene having some regions with up to triple flakes. According to Li et al. [79], they reported that the growth of graphene is most seen in the catalysed surface process in their study unlike in the precipitation process used by other researchers [46], [76], [80].

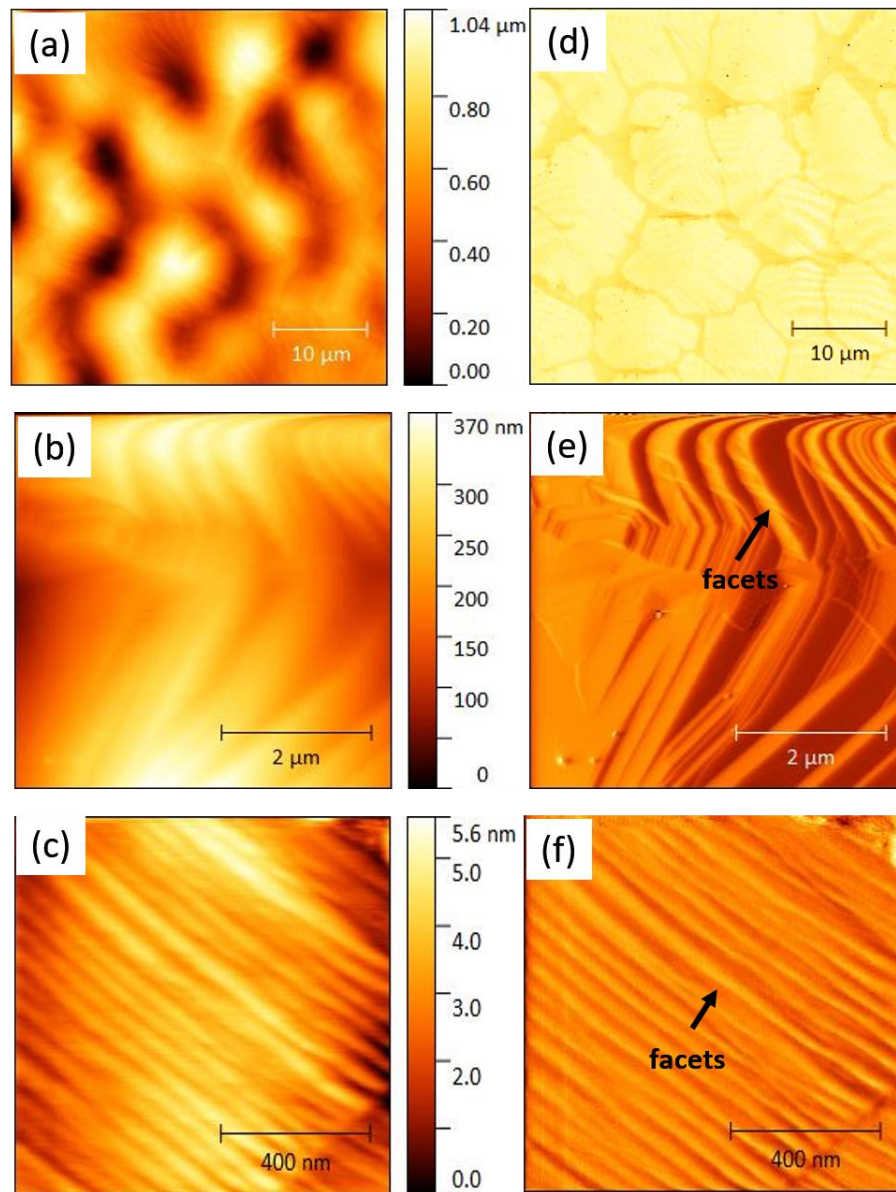


Figure 4-9: Different scan area of AFM for 30 mins anneal and 20 mins growth (a), (b), (c), (d) are topography images and (d), (e), (f), (g) are images in vertical deflection.

Figure 4-9 shows the AFM image for the 30 mins of annealing and 20 mins growth times. Panel (a), (b) and (c) shows image topography of the sample. No

impurity spots density was present. Graphene grain sizes in (a) are approximately in scale of 10 to 20 μm . The facet features can be seen in image (b) and (c). It shows that different scan area may experience different faceting features. The meandering facet in (b) are in microscale while in (c) in nanoscale. As explained in Chapter 1, faceting minimises graphene bending energy and it can happen randomly on the graphene films on the same sample. Panel (d), (e) and (f) display an alternative image of sample topography as it processed by Gwyddion software. This is the best image obtained after deflection signals had been minimised. As growth times was double compared to Figure 4-8, the facet features still appeared on the sample.

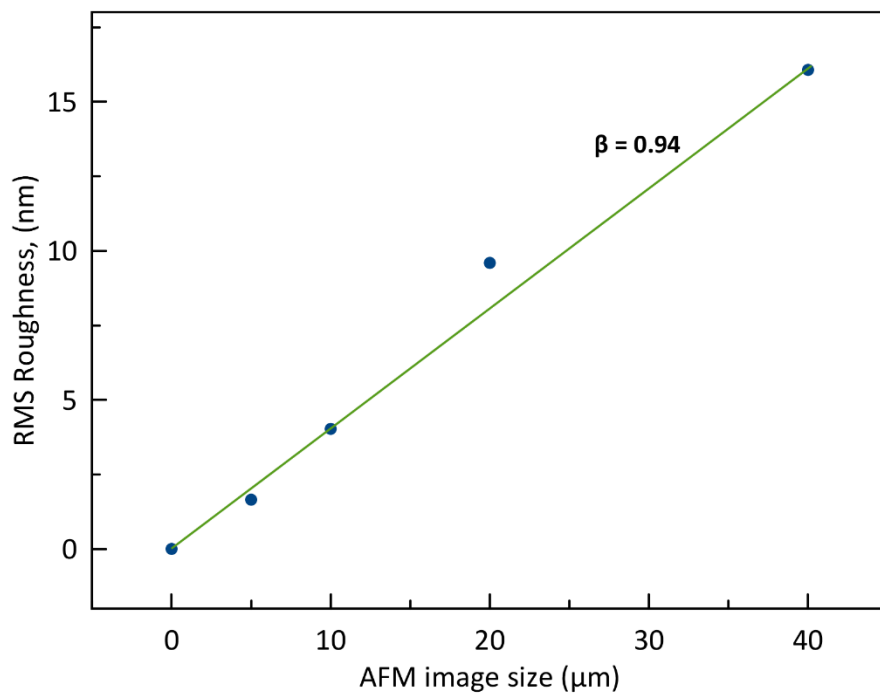


Figure 4-10: RMS roughness as a function of AFM image size.

Figure 4-10 shows the RMS roughness from the same sample in Figure 4-8. The graph is plotted with 4 different image sizes which are 5 μm , 10 μm , 20 μm and 40 μm . The RMS roughness was processed with Gwydion software analysis using 3rd order polynomial fitting and background extraction, lines were corrected by matching the height medium and then the horizontal scars were corrected. It is nearly linear which means that there are still rougher surfaces features being “found” as the image increases. The data are well fitted with $\beta = 0.94$. This is consistent with the deeper polishing scratches being removed by the final polish and the overall variance of scratch depth reducing significantly. Eventually it will tail off but the length scale on which this happens is beyond that accessible by our AFM. The roughness exponent is close to 1 for all samples measured by the AFM, independent of the growth and annealing conditions. This means there must be large-scale roughness (compared to AFM scan sizes of tens of microns) in the Cu plate which does not depend on the details of the graphene growth. But overall the roughness is quite acceptable for performing MBE and RHEED.

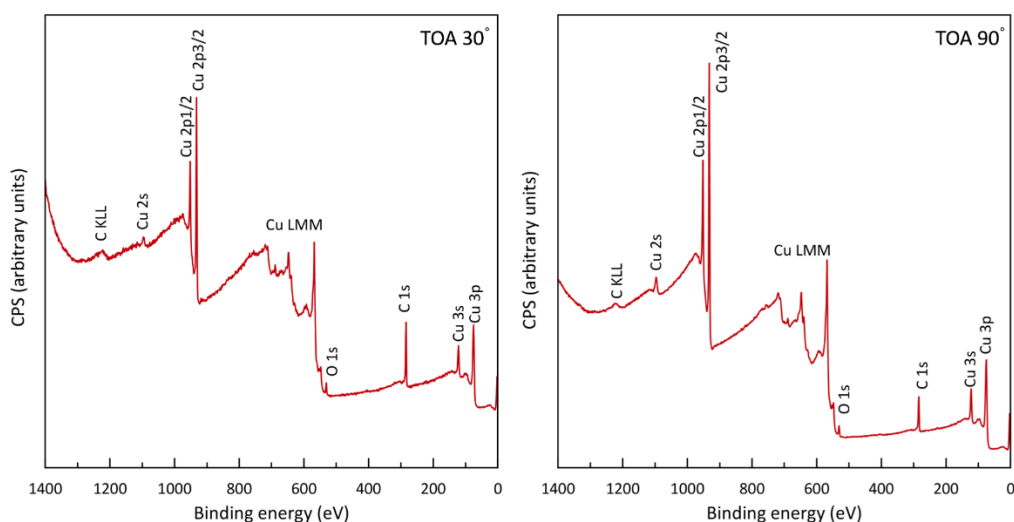


Figure 4-11: XPS survey scan for TOA 30 °(left) and TOA 90 ° (right).

Further, in order to examine the elements lying on the sample after CVD growth, a typical survey scan is shown in Figure 4-11. This broad survey scan was initially applied to get useful information to which elements they are bonded to the sample before measuring the elemental composition. XPS was used after SEM and several air transfers. All XPS data are from 30 mins anneal time and 20 mins growth time as shown in Table 4-1. This sample shows full coverage with no bare Cu presence and measurement is taken with two different take-off-angle, (TOA) of 30° and 90° . Several peaks of Cu LMM was detected and C, Cu and O peaks are observed. No other elements can be seen below detection limits. The O 1s peak is very small and not much O is contained in both angles. Cu 1s peak is higher in TOA 30° as surface sensitivity increased after the samples had been tilted. It can be assumed as the Cu atoms are only on the surface of the sample and not embedded in the graphene film. All fits used a Shirley background Voigt function and symmetric mixed Lorentzian (95%) – Gaussian (5%) component excluding O 1s. Figure 4-10 confirms the main elemental components are C, Cu and O.

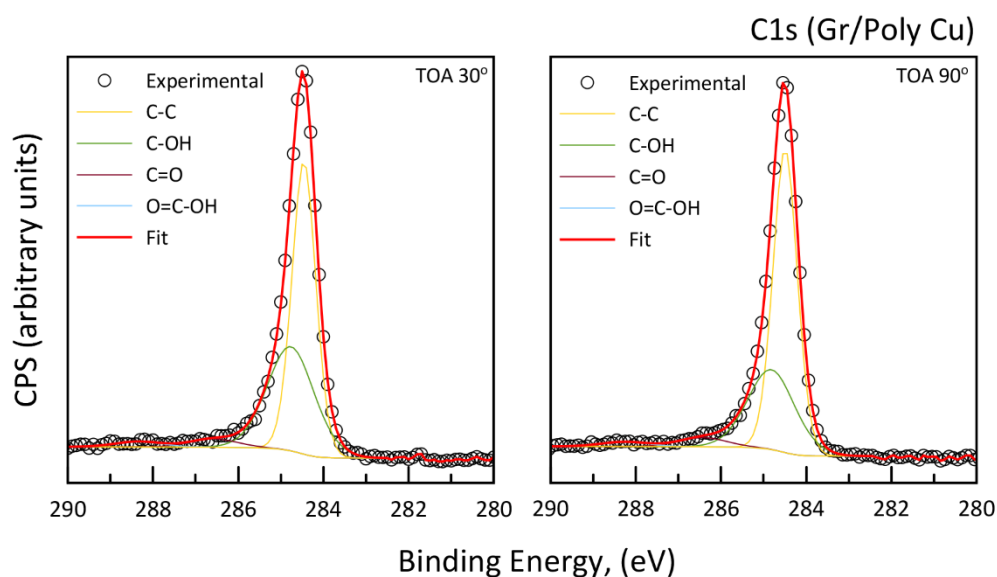


Figure 4-12: Right panel is fitted XPS spectra of C 1s with TOA 90 ° and left panel with TOA 30 °.

Figure 4-12 shown C 1s for both TOA angles and had been fitted using typically C-C element with higher BE components and symmetric. From the results obtains from the graph, the binding energies (BE) of the common chemical state of sp^2 carbon is approximately (284.5 ± 0.1) eV and in the sp^3 carbon chemical state is (284.8 ± 0.1) eV. The copper plate was observed to primarily contain carbon as indicated by the C-C and hydroxide like components. The C-C peak may contain atmospheric or adventitious carbon contamination. The C 1s spectrum shows intense sample of sp^2 carbon feature with a wider and asymmetric tail towards the binding energy. C-OH peak can be attributed to asymmetry of C 1s in pristine graphene [81]. Other features observed from the C 1s peak (carbon-carbon peaks) include satellite features.

Additionally, the results in Figure 4-12 demonstrate a symmetric shape when in sp^3 -bonded carbon with high concentrations. The symmetrical trend is noted to slightly shift to the area with higher BE. Functionalised graphene is noted to have a C1s spectrum which is complex in sp^2 and sp^3 components. Carbon layers on Cu are actually graphene films since the graphene sheet is a monolayer of carbon atoms which are bound together tightly. In principle, we cannot distinguish sp^2 from sp^3 in C 1s main peak unless X-ray induced C KLL Auger peak is adopted in a semi-quantitative approach [82]. It could be diamond-like-C, but SEM and Raman make this very unlikely.

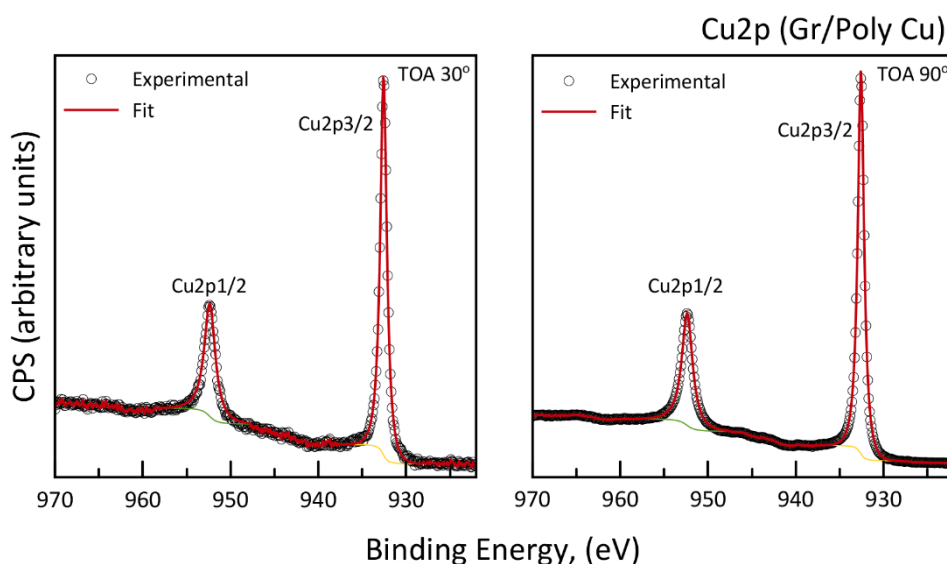


Figure 4-13: Right panel is fitted XPS spectra of Cu 2p with TOA 90 ° and left panel with TOA 30 °. Open circles are experimental data points and red lines show fits as described in the text.

Figure 4-13 represents Cu 2p fitted by mixed Lorentzian (95%) – Gaussian (5%) with single component and no chemical shift. It showed that no Cu oxide peak

which is correlated that no bare Cu and proved that this sample experienced full coverage of graphene. Graphene layer covered bare Cu from being oxidised. Each spin-orbit splitting line is fitted with a single component of metallic Cu. Cu metal (chemical state) shows a BE of Cu 2p_{1/2} and Cu 2p_{3/2} to be approximately (952.4 ± 0.1) eV and (932.6 ± 0.1) eV respectively. The spin orbit splitting is (19.8 ± 0.1) eV and comparing with NIST database [83], Cu 2p values are 19.80, 19.82 and 19.90 eV. In particular, no higher BE such as Cu (I) oxide, Cu (II) oxide and Cu (II) carbonate dihydroxide of 933 eV, 933.5 eV and 934.7 eV respectively were present [84]. In addition, no difference was observed between 30° and 90° TOA and we conclude that the surface was not oxidised. Graphene has protected Cu from oxidation during air transfer CVD to XPS via SEM and AFM.

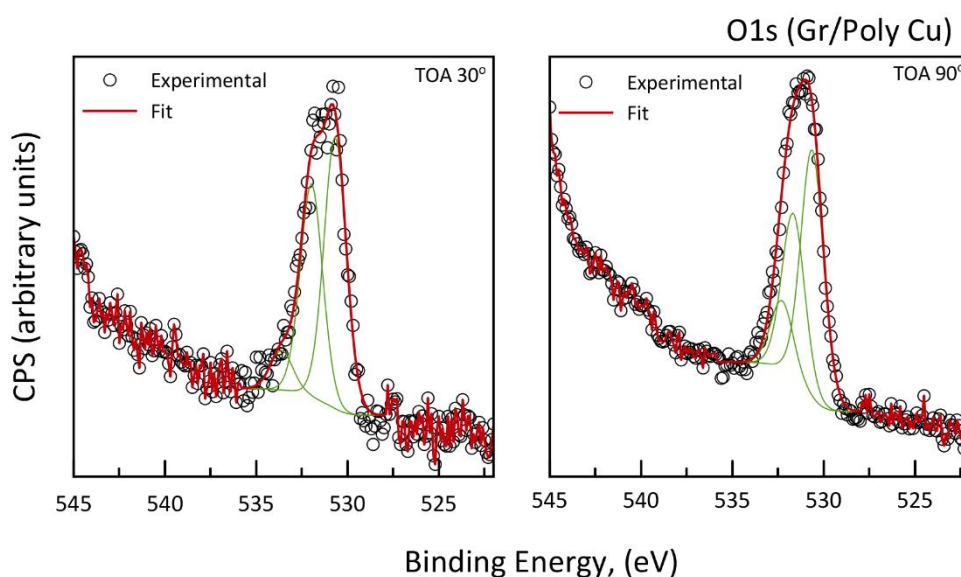


Figure 4-14: Right panel is fitted XPS spectra of O 1s with TOA 90° and left panel with TOA 30°.

Further, O 1s XPS spectrum were obtained and summarised as shown in figure 4-14. All fits for this spectra used symmetry mixed of GL(30), Lorentzian (30%) – Gaussian (70%).

The O 1s fitting shown in Figure 4-14, represents the different binding energies required in fitting graphene on Cu plate core level spectra. O 1s spectra interpretation is not a straightforward procedure as there are broad O 1s peaks for multiple overlapping components hence the binding energy for most compounds fits with a short range [85]. Also, the organic contamination hinders carbonates discernments in the O 1s region. The signal to noise (s/n) is obviously worse and is present at small percentage the end of the graph. The adventitious oxygen is probably physisorbed contamination e.g H₂O, O₃, CO and CO₂. It could be a small amount of oxidised Cu. CuO is not visible in spectra as the XPS average depth of analysis is approximately 5 nm. The O 1s peak position can be used for measuring the band gaps [85] of various materials such as graphene on Cu. Oxygen is a residual contaminant for the graphene produced. Besides being contaminated with oxygen, annealing at lower temperatures still produces high quality undoped graphene. The high temperatures' formation of doped n-type graphene first removes all the oxygen that was initially absorbed. Also the oxidisation of graphene on the plates was identified to be similar to that grown on the Cu foil which also confirmed that graphene is typical compared to the one grown on the thinner foils of Cu.

Results obtained from the XPS measurement are summarised in Table 4-3.

Table 4-3: Summary of chemical composition for C 1s, O 1s and Cu 2p for XPS spectra of graphene on Cu plate.

Name	%Atomic Concentration	
	TOA 30°	TOA 90°
C 1s	(50.88 ± 0.1)	(26.99 ± 0.1)
O 1s	(4.60 ± 0.1)	(3.47 ± 0.1)
Cu 2p _{1/2}	(20.52 ± 0.1)	(34.12 ± 0.1)
Cu 2p _{3/2}	(24.00 ± 0.1)	(35.41 ± 0.1)

Table 4-3 presents the quantitative data. The key feature of these percentage atomic concentrations is the representation of the intensities as a percentage, that is, the ratio of the intensity to the total intensity of electrons in the measurement [86]. Using Casa XPS software, the data had been extracted after fitting was done. It shows higher percentages at TOA 30° for O 1s. This evaluation of different TOA determining surface sensitivity with lower TOA 30° compared to normal emission TOA 90°. The impact of oxygen on the various components is caused by the sample exposure to the atmosphere through oxidation, water or adventitious contamination. Nevertheless, oxygen contaminates on top of the graphene but has not chemically reacted with graphene or Cu.

4.4 Summary

As conclusion in this chapter, we confirm graphene on Cu plate is the best quality to obtain the growth of MnSb in MBE. Eventhough the grain size as not as good as foil, but it is acceptable as full coverage of graphene is promising. RMS roughness is slightly larger than on foil. RHEED also can be measured in-situ as rigidity of the plate is not compromised after spot-welding. Faceting under graphene occurs like on foil and this is a signature feature that is still uncovered except for various assumptions in [51] stating that faceting minimise the bending energy of graphene. Graphene on Cu plate acted as a substrate in the next chapter for the growth of ferromagnetic MnSb in MBE.

Chapter 5: MnSb on graphene on Cu plate

5.1 Introduction

An advantage of MnSb in device optimisation and design, is that it can process materials with the utilisation of conventional III-V etching and lithographic techniques. This helps in the scalable processing of spintronic devices. Also, there are numerous reports by various researchers on using the single crystal semiconductor substrates for successful growth of epilayers of MnSb where most of them are focused on magnetism and optics applications [41], [87]–[94]. A broad study had been carried out in our group and prior knowledge of ferromagnetic MnSb material motivated an interest for a different substrate [35], [91], [94]–[96]. Typical T_{sub} for MnSb thin films growth on single semiconductor substrate was recorded at 415 °C [34]. Early experiments for MnSb on graphene on Cu foil were very inconsistent at $T_{\text{sub}} > 250$ °C due to low sticking coefficient of graphene.

In Chapter 4, graphene on Cu plate has been epitaxially grown with the best quality with > 90% monolayer coverage. Graphene is known as a zero-gap semiconductor and this is the challenged in this study whether MnSb can be overgrown on graphene epitaxially. MBE is used as a method of thin film deposition. In-situ and ex-situ surface studies such as SEM, AFM, RHEED, LEED, XPS and SQUID have been conducted and discussed here.

5.2 Experiment details

Cleaning of graphene on Cu plate substrate needed extra care. Cu plate substrates, measuring approximately 7 mm x 7 mm, were mounted onto a sample plates using tantalum wire fixed by spot weld. Surface debris on sample plate was then removed by chemical degreasing using acetone. Isopropanol and water wash cycle followed by drying with dry nitrogen. Samples were loaded into the vacuum chamber and prepared by ion bombardment and annealing to 200 °C for one hour. The Sb cell was heated to 360 °C and the Mn cell to 850 °C respectively before the growth was started for fifteen minutes. The temperature for the substrate, T_{sub} was set to 200 °C. The beam flux ratio, $J_{\text{Sb/Mn}} = 5.5 - 6$, was fixed while range of thickness have been grown with constant growth rate. While growing, in-situ RHEED was observed and recorded with the RHEED gun operating at 12.5 keV. Sb capping at $T_{\text{sub}} = 80$ °C for 90 s was done to prevent oxidation of the surface samples. Thicknesses of the samples were calibrated relative to the MnSb on graphene substrates and afterwards scaled to the measured Mn beam flux. This nominal thickness growth rates were in the range 2 – 3 nm min⁻¹. After RHEED studies, samples were removed from the MBE chamber and imaged using SEM, AFM, XPS and magnetometry. It should be noted that no special precautions were taken to prevent surface oxidation during transport for imaging.

5.3 Results and discussion

Several MnSb samples of varying thickness have been grown on graphene on Cu plate. All samples were Sb-capped. As an example, MnSb is preferentially forming at graphene grain boundaries. Additionally the density of MnSb islands changes with graphene monolayer or bilayer coverage. The high mobility of adatoms (including Mn and Sb) on graphene provides additional support to this idea, whereby adatoms are free to move around on a graphene sheet but are trapped at boundaries. Spontaneous nucleation on the substrate, presumably, defects gives rise to a low density of islands on the foils themselves. The solution is to turn down the temperature at 200 °C. This is applied throughout all samples in the experiment. The times is varied from 30 s to 15 mins and it corresponded to nominal thickness 0.9 nm – 28 nm. The sample that had been reported in detail here is labelled G005 with 28 nm nominal thickness.

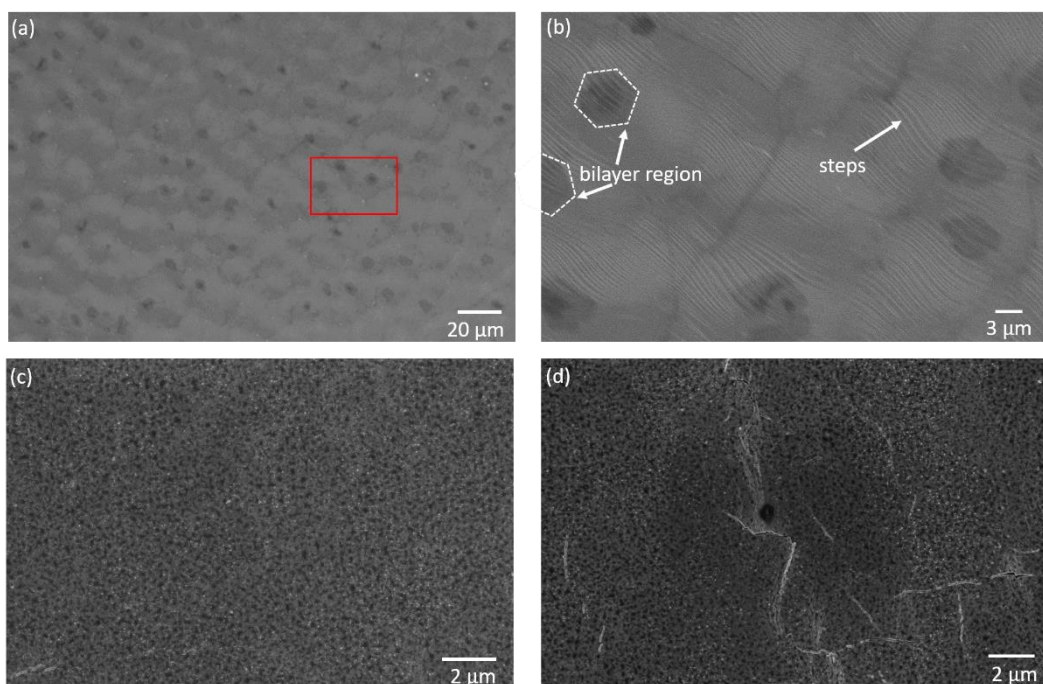


Figure 5-1: (a) Low magnification SEM image of graphene on Cu plate with red rectangle the position of a zoom shown in (b), (c) Low magnification SEM image of MnSb on graphene (supported on Cu plate) and (d) other part of sample (c)

Figure 5-1 shows SEM images before and after MnSb thin films growth. Panel (a) shows the full coverage of graphene with approximately 5% of bilayer. The graphene grain sizes are approximately $> 10 \mu\text{m}$. Panel (b) shows higher magnification of (a) and bilayer regions hexagonal-like as labelled in the figure. Apparently, no contrast due to Cu or graphene grains and no graphene bilayers appeared after MnSb growth as seen in panel (c). The presence of islanded light and dark granular pattern indicated that graphene layer is completely obscured. These patterns are consistent with panel (d) showing the other part of sample for extra contrast. At the centre of the figure, it displays white line features that probably are due to large-scale Cu roughness. The Cu plate has been bent a little

during manual cutting for MBE which may locally increase the number of white lines as defects. Nonetheless, dark granules can still be seen on these lighter defect features. As can be seen in panel (d), a continuous growth of MnSb is observed regardless the defect features.

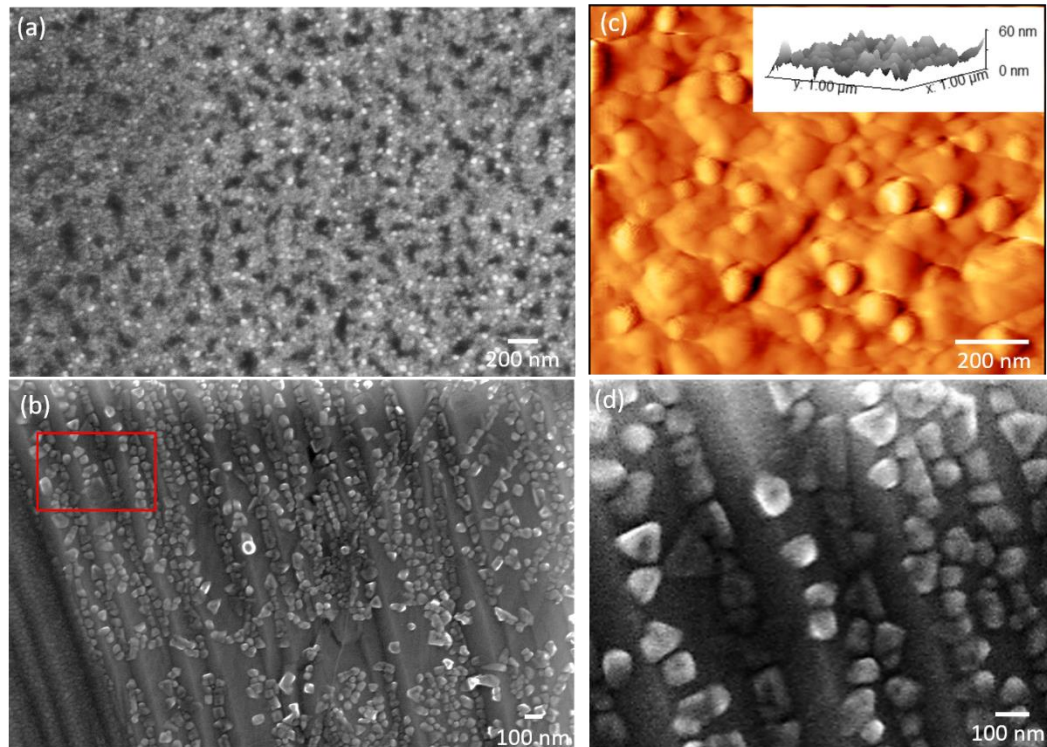


Figure 5-2: MnSb on graphene on Cu plate with 28 nm nominal thickness. (a) Low magnification SEM image using secondary electron mode, (b) High magnification SEM image using backscattering mode with red rectangle the position of a zoom shown in (d), and (c) AFM image with inset of 3D profile.

Figure 5-2 displays the SEM and AFM images of MnSb on graphene. Panel (a) is obtained using secondary electrons mode very high magnification up to nano-scale. This mode imaging is more surface sensitive and due to the atoms near the surface, hence the granular pattern can still be seen but the energy was

sufficient to escape from the sample surface. To get visible contrast, backscattering mode in panel (b) was used as a signal. It appears that clear facet with continuous coverage by nano-crystallites. The angular shapes looked brighter as backscatter influenced lighter elements had low contrast. Sb has greater atomic mass than Mn and Cu, hence angular shapes can be differentiated based on contrast in this image. Panel (d) is the zoomed-in region on SEM image (b). To all appearances, the angular shapes is not curved or smooth but appeared as with edges. Some of nano-crystallites had hexagonal symmetry and consistent with hexagonal basal plane in MnSb (0001). Furthermore, the direction is preferentially aligned and suggested that we have epitaxial on the sample. Linear structure in panel (b) aligned with epitaxy of MnSb nano-crystallites. Cu faceting as we discussed in Figure 4-8 and 4-9 do not lift up after MnSb growth. Panel (c) shows AFM image and it can be inferred that nano-crystallites are formed during growth and that these are likely to be MnSb. The inset 3D profile reveals that nano-crystallite forming almost 90- 95 % complete coverage on the substrate. The height of island is between 5 and 50 nm and consistent as Volmer-Weber growth modes as explained in Section 1.5.

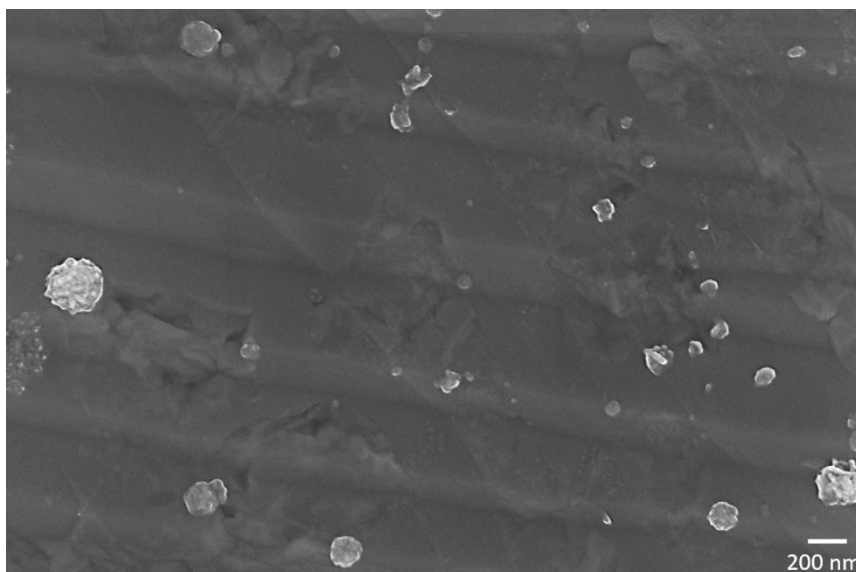


Figure 5-3: SEM image for thinner sample with nominal thickness 1.6 nm with backscattered electron signal mode.

Figure 5-3 shows SEM image of MnSb on graphene with 1.6 nm nominal thickness. It seems that nearly horizontal stripes were Cu facets from graphene on Cu plate CVD growth. There were isolated MnSb clusters and not as much as in Figure 5-2 (b) and affirmed that there was an approximate 5% incomplete coverage with crystallites preferentially forming at graphene on Cu plate.

Next, we evaluated the structure, streaks and sharpness of graphene on Cu plate using RHEED as shown in the Figure 5-3. The RHEED was monitored throughout the growth process and was recorded to identify any changes which might occur in the symmetry thus in turn affecting the consistent formation of the MnSb layers.

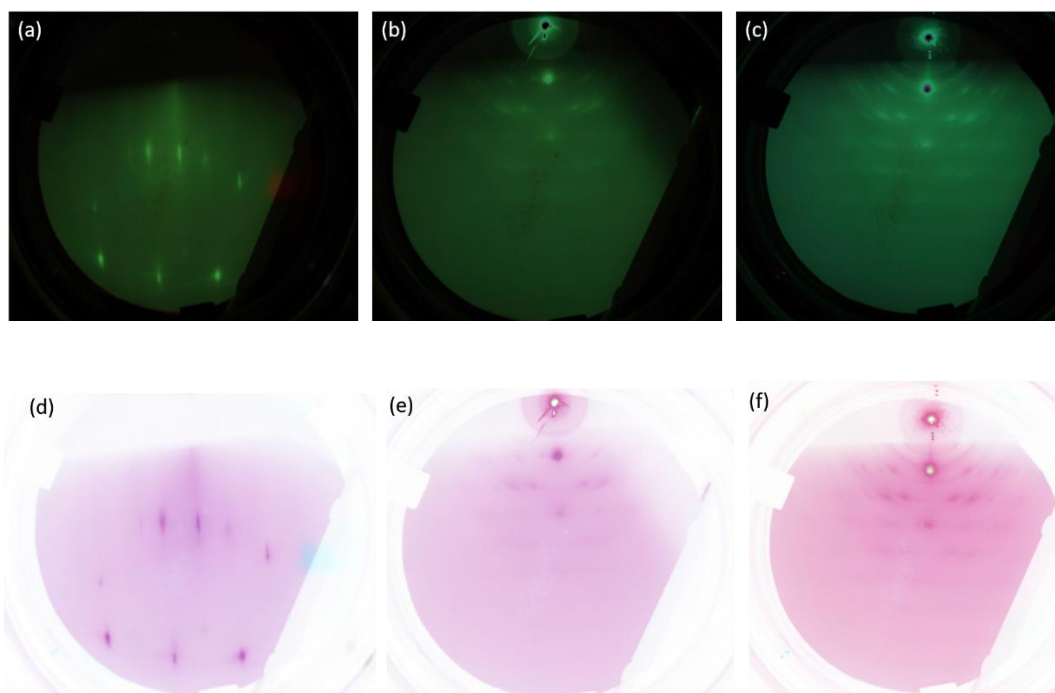


Figure 5-4: RHEED patterns for before, during and after growth respectively (a) graphene on Cu plate (b) MnSb growth after 4s and (c) MnSb after Sb cap. Panel (d), (e) and (f) highlight a contrast image of streaks and spots pattern.

Figure 5-4 represents RHEED patterns prior MnSb growth, during and after Sb capping. Panel (a) shows streaks appearing at various location on the substrate and it is consistent with clear and clean graphene full coverage based on XPS spectrum Figure 4-11. Irregular sharp streaks are consistent with well-ordered Cu polycrystalline domains. There are other streaks and spots from other grains which are Cu and/or graphene with different textures.

In RHEED, indexing diffraction pattern is too complex for Cu and graphene since their lattice parameters quite similar. Panel (b) shows MnSb thin films after 4 s after growth started. The nominal thickness approximately 0.124 nm and obviously the irregular streaks pattern in (a) had disappeared and exposed a

regular array of spots indicating transmission diffraction. The patterns did not change as the sample was moved parallel to the surface (x and y changes on the sample manipulator). In contrast, graphene on Cu plate RHEED pattern as discussed in Figure 4.2 changed a lot with small movement because the surface diffraction depends on local grain orientation. This was not the case for MnSb transmission diffraction patterns presumably due to the bulk crystal planes being orientated almost uniformly on the surface.

RHEED pattern unveiled mirror plane symmetry on the sample but were too complex for overall symmetry to be indexed. There was some array of spots appeared parallel to the surface and it can be measured between the space of the line using the calibration of RHEED system. Indexing the pattern using RHEED interpretation in Chapter 2 had clarified that d-spacings value is 4.9 Å. The MnSb bulk d-spacings for (0001) is 5.79 Å. This difference may be influenced by a Cu facet angle. LEED in Figure 4.3 yields an important feature of facet which correlated with graphene spots. MnSb presumably growth on tilted facet and d-spacings is smaller due to the facet angle.

Panel (c) in Figure 5-4 shows diffraction pattern after Sb capping of the 28 nm MnSb films. During this stage the Sb flux held for 90 s, resulting in cap thicknesses between 1 and 4 nm. RHEED is recorded after the Sb cap was completed. The cap displays spots RHEED pattern and demonstrate the same symmetry with MnSb in Figure 5-4(b). On this basis, Sb caps are thought to be oriented as a layer and throughout this chapter, Sb cap is referred to h-Sb denoting the hexagonal setting of the rhombohedral Sb crystal structure [97]. RHEED patterns appeared from the underlying MnSb transmission still exists and is identified to be superimposed on the powder rings. The array of spots does not change much and additional powder diffraction rings appear. The rings result from the randomly oriented Sb crystallites diffraction. During MnSb nucleation, atoms

impinged on the surface and met other atoms and formed islands. These islands formed quickly after couple of seconds as in panel (b). The timer used in-situ RHEED experiment to confirm the growth time and recorded with a digital single lens camera. Initially, the glancing angle of incident electrons scattered through the atoms on the surface. During growth, islands became denser but maintained height less than 50 nm. A high beam energy presumably strokes at the corner of the islands and displayed almost the same pattern as in panel (b). Overall the pattern can be interpreted as thin Sb layer on MnSb nano-crystallites. X-Ray Diffraction (XRD) measurements were attempted on the nominal 28 nm thickness sample but we were unable to detect any XRD peaks. It was not surprising because it was difficult to align polycrystalline Cu in this type of scan. This led to very weak scattering for x-rays to be detected.

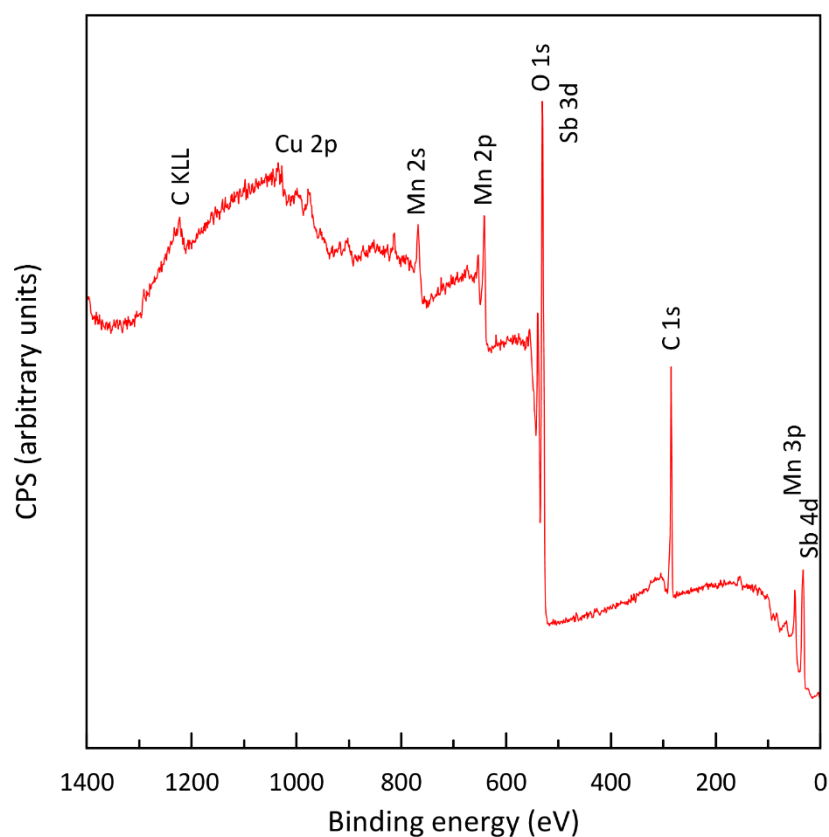


Figure 5-5: XPS survey scan for MnSb on graphene/Cu.

XPS measurements were carried out after several air transfers. Figure 5-5 shows survey scan for MnSb on graphene. The take-off-angle is 90° . The elemental peaks of Mn, C, Sb, O and Cu are obviously present. No other unexpected elements appear. All peaks except Cu were fitted using Shirley background and Gaussian-Lorentzian (GL) ratio varies according to the element. The XPS survey scan for TOA 90° in Figure 4-10 indicated Cu peaks with very high intensity in contrary with Figure 5-5.

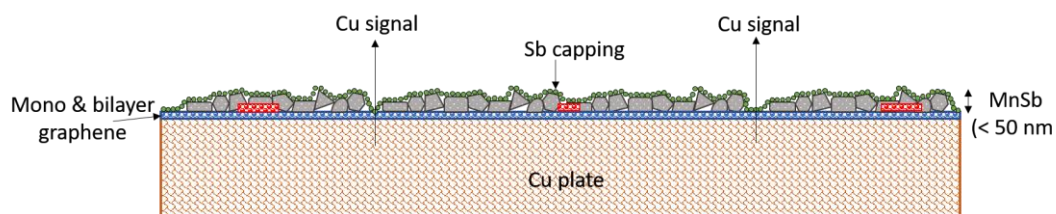


Figure 5-6: An illustration of MnSb growth on graphene on Cu plate

Figure 5-6 shows a simplistic schematic of MnSb on graphene/Cu growth in this study. It illustrated the schematic based on SEM and AFM findings in the previous sections of the thesis. Blue and red layers display graphene monolayer and bilayer respectively. Angular shapes mixed with hexagonal structure in grey colour represents MnSb islands with height less than 50 nm. The small green circle shows thin Sb capping layer to protect surface from oxidation. Cu plate (as labelled in figure) experienced full cover of graphene with some bilayer region less than 5%. An incomplete MnSb nano-crystallite coverage formed on graphene resulting in small Cu signal passing through thin Sb cap layer. It can be seen in XPS survey scan there is low intensity of Cu peak at high binding energy.

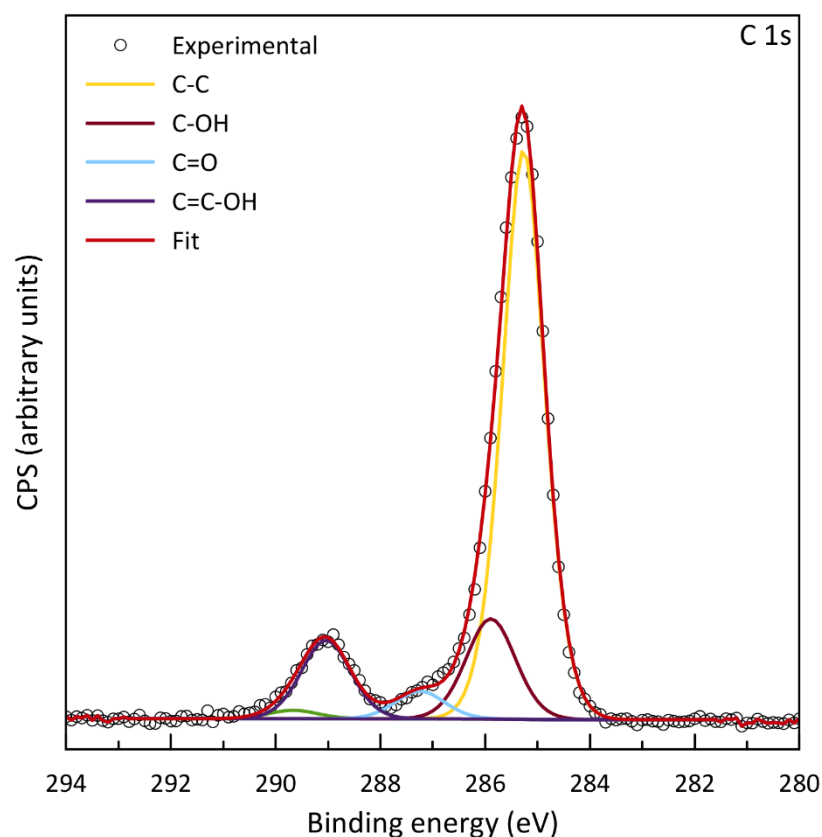


Figure 5-7: XPS spectrum of C 1s for MnSb on graphene/Cu. See Appendix 2 for spectral parameter details.

Figure 5-7 shows C 1s spectrum from XPS measurement. Peaks fitted using symmetric Voigt function, GL(30) for all components. The value for C-C component had been set to a binding energy of 285.2 eV and the other higher B.E as labelled C-OH (285.9 eV), C=O (287.2 eV), and C=C-OH (289.0 eV) were typical contamination components. As mentioned in Chapter 2, argon sputtering in XPS would eliminate carbon contamination due to several air transfer but we expected measurable quantity of adventitious carbon contamination from Sb capping. Any graphene contribution to C 1s should be small and suppressed by MnSb.

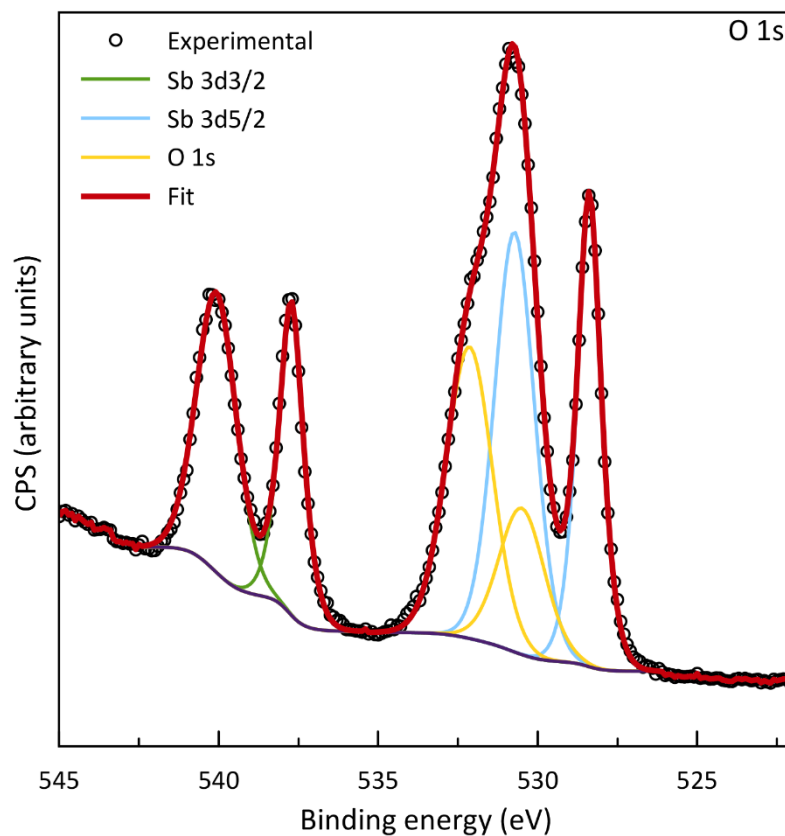


Figure 5-8: XPS fitted Sb 3d and O 1s regions indicate Sb-oxides overlapping of atmospheric O. See Appendix 2 for spectral parameter details.

Figure 5-8 shows XPS spectrum for O 1s and Sb 3d of MnSb on graphene. Interpretation of O 1s spectrum is not direct where two different regions to fit all three doublets are required for core level corresponding to Sb 3d3/2 and O bonding environments. The corresponding binding energies of all components are given in Table 5-1. All components for Sb fitted with GL (70), Sb oxide with GL (50) and O with GL (30). Sb 3d5/2 area constraints is fixed to 1.5 higher than Sb 3d3/2 with similar FWHM between spin-orbit splitting. O 1s region resulted in broad with

overlapping directly with Sb 3d_{5/2} peaks in blue line. This is consistent with Sb capping being strongly oxidised but Sb peaks still can be elemental and proves that the capping works.

Table 5-1: Peak fitting details showing the assigned bonding environment and binding energy for a sample MnSb on graphene. Values are taken from the fits in Figure 5-8.

Binding energy (eV)	Bonding environment
528.3	Sb 3d _{5/2} from Sb
530.7	Sb 3d _{5/2} from Sb ₂ O ₃
530.9	Sb 3d _{5/2} from Sb ₂ O ₅
530.5	O 1s metallic oxides
531.9	Adventitious O
537.7	Sb 3d _{3/2} from Sb
539.6	Sb 3d _{3/2} from Sb ₂ O ₃
540.1	Sb 3d _{3/2} from Sb ₂ O ₅

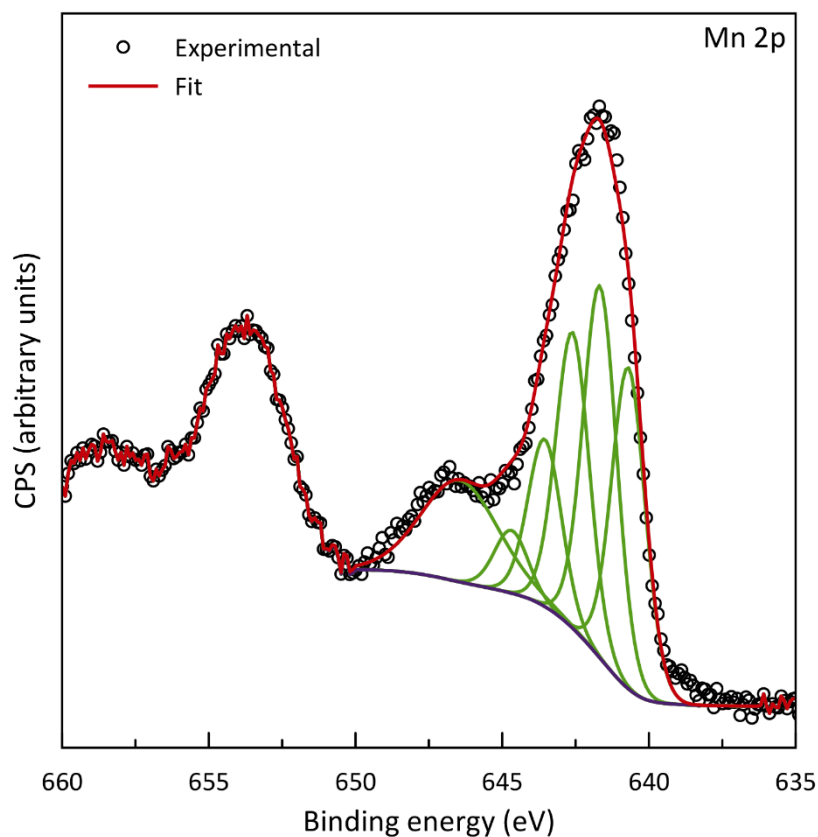


Figure 5-9: XPS spectrum for Mn2p of MnSb on graphene.

For MnSb, there are no strong evidence that Mn 2p region derives necessarily as the surface treatment progresses. Figure 5-9 shows Mn 2p metal components model from Biesenger et al, [98] for Mn 2p_{3/2} spectral parameter. The main peak is centered at 641.8 eV and its broad and asymmetric with a slightly bigger shake-up feature at 647.1 eV, approximately 5.3 eV from the main peak. The satellites are particularly sensitive to the stoichiometry of the oxide, decreasing in intensity upon either surface oxidation or reduction and disappearing completely in higher oxide phases [99] . All the peaks are fitted with

GL (30). The region for the Mn 2p core level is not wide enough to fit both parts of the doublet as the cut off before the shake-up feature from the 2p_{1/2} peak is out of range, hence is challenging to fit. We used multiplex peaks to define origin of the satellite peaks and the peaks contributed to the Mn 2p core level. The spin-orbit splitting energy Δ_{so} for first-row transition metal 2p varies depending on the chemical state and local environment [100]. The value of Δ_{so} draw out from the spectra in Figure 5-9 shows an increase (11.8 ± 0.2) eV compared to our previous study for bulk MnSb of 11.5 eV [94].

Figure 5-10 shows XPS spectra for a nominal 28 nm thick sample taken at 90° TOA of the shallow core region (25 to 60 nm) and a zoom-in of the Sb 4d region. It can be seen on top panel that both Mn and Sb are present in the surface region. The Mn component peaks were fitted according to model of MnO in Ilton et.al [101]. Upon obtaining the best fit for multivalent samples, the fit parameters were fixed for individual oxidation states but allowed to shift energies and intensities as packets relative to other oxidation states [102]. Our observations indicated that in Mn 3p fitting, the Sb region looks like a metallic state (MnSb) thereby highlighting the difference between the regions [102]. The main peak at 48.5 eV can be assigned to a Mn³⁺ state [100] while the higher binding energy peak may be due to mixed-valence Mn [94].

Figure 5.10 (bottom panel) shows the Sb 4d region for the sample. Four doublets have been fitted and are assigned as Sb-Sb, Sb-Mn and Sb-O bonding environments. Vacuum annealing first reduces the higher energy binding components and the peaks which appear to be almost overlapping. Moreover, the Sb 4d within the shallow core was fitted with two ratios GL (50) and GL (70) in order to obtain peak areas which enhanced the accuracy of estimating the

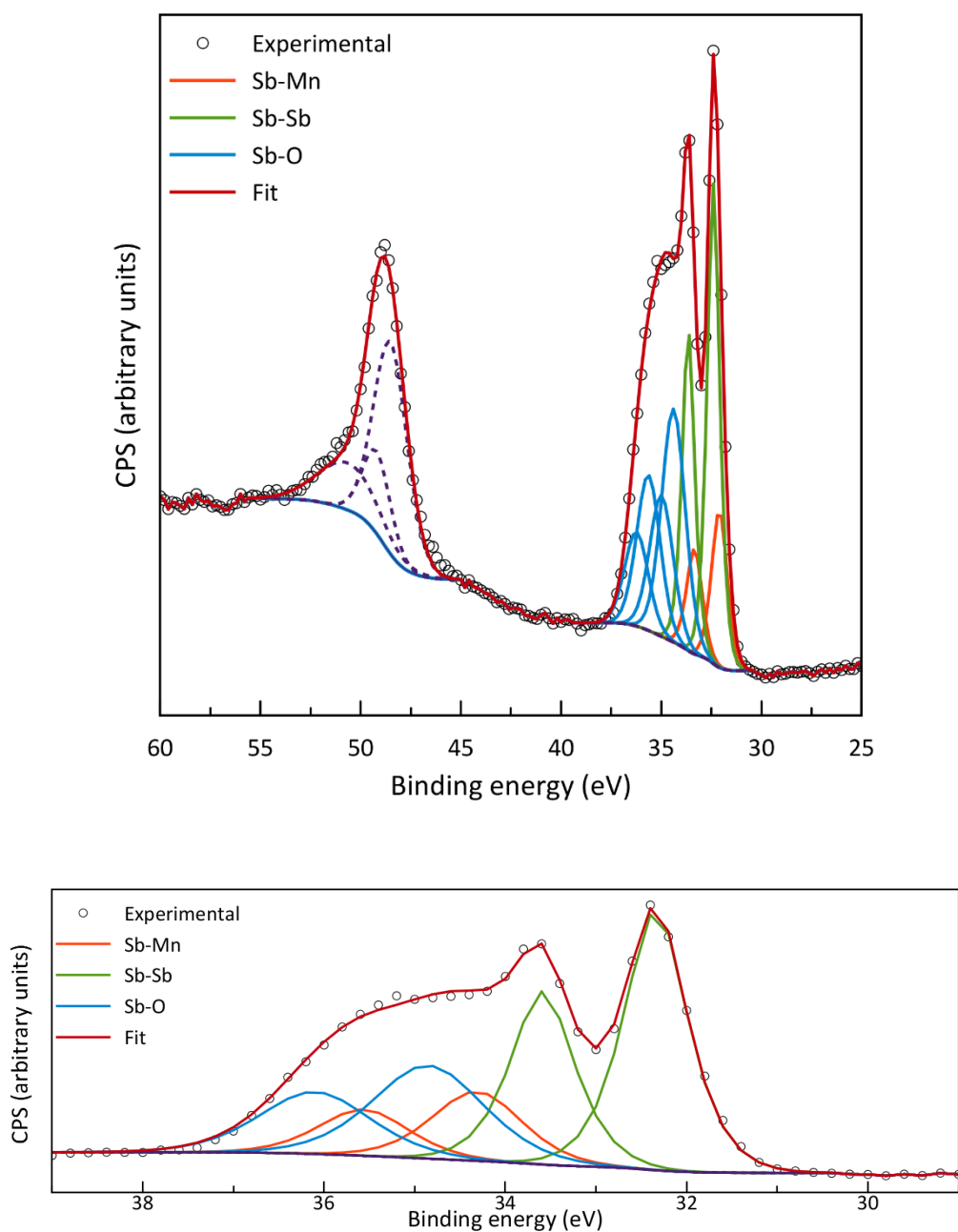


Figure 5-10: XPS spectrum of shallow core region with the Mn 3p and Sb 4d core level presents on the (top) panel and (bottom) panel is Sb 4d regions fitted indicates the presence of Sb-Sb, Sb-Mn and Sb-O. See Appendix 2 for spectral parameter details.

stoichiometry trends. Peak fitting details of the binding energies and bonding environment are summarised in Table 5-2.

The value of chemical shift relative to Sb-Sb component is formed at -0.30 eV for Sb-Mn bonding environment while a shift of 1.99 eV is formed for oxide peak. The oxide peak was allowed a larger range of FWHM values in order to account for multiples oxides such as Sb_2O_3 , Sb_2O_3 , and Sb_2O_3 [103].

The chemical shift for Sb-Mn determined here is slightly smaller than previously observed [94]. Referring to Table 5-3, some conclusions can be drawn regarding the stoichiometry of these samples. These sample had been exposed to several days of air transfer before it went to XPS measurement. It was expected to experience heavily contaminated at Sb capping layer and can be oxidised. The surface is Sb-rich with a ratio of Sb-Mn of (2.95 ± 0.03) . This is significant with the oxide bonding environments at 49.7 %. This is opposed to $\text{MnSb}(0001)$ samples reported by Maskery et.al [94] where the surfaces are Mn-rich as composition ratio as high as Mn:Sb 4:1 after several days of air transfer. It is very likely that Mn-oxides has not enough time to form first than Sb-rich oxides. Despite this is possible that the high reactivity of Mn, relative to that of Sb would originally lead to the formation of Mn oxides and not Sb oxides.

Table 5-2: Sb 4d region peak binding energies, chemical shift relative to the Sb-Sb bonding environment and percentage breakdown of Sb bonding environments for MnSb on graphene/Cu sample. Values are taken from the fit shown in Figure 5-10.

Bonding environment	Binding energy 4d _{5/2} (eV)	ΔE (rel. to Sb-Sb) (eV)	Percentage
Sb-Sb	32.40	0.00	36.1
Sb-Mn	32.10	-0.30	14.2
Sb-O	34.39	1.99	49.7

Table 5-3: Core level and percentage composition for the C 1s, O 1s, Mn 3p, and Sb 4d

Core level	Percentage composition
C 1s	41.41
O 1s	25.68
Mn 3p	8.34
Sb 4d	24.56

Hysteresis loop examination via magnetometry measurements as mentioned early in Chapter 2 plays a significant role in examining the magnetic properties of MnSb. In this experiment, SQUID (superconducting quantum interference device) measurements generate the hysteresis loop by the measuring the ferromagnetic magnetic flux while changing the magnetising force. Results are shown in Figure 5-11.

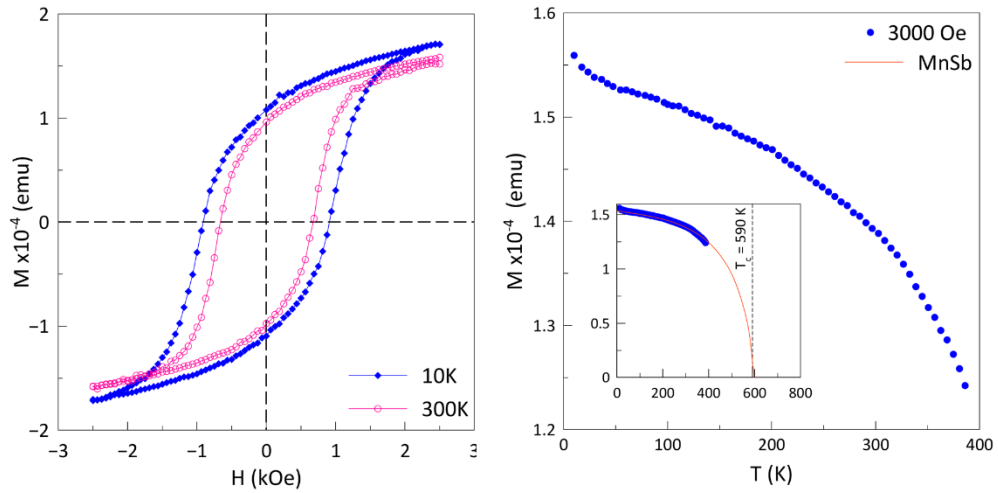


Figure 5-11: SQUID magnetometry of a 28 nm MnSb nominal thickness on graphene on Cu plate substrate. Panel (a) shows a hysteresis loop (M - H) acquired at 10 K and 300 K between -3 and 3000 Oe. Panel (b) shows a M - T plot for the same sample taken at a fixed applied field of 3000 Oe, the inset shows a Brillouin function plot for MnSb at $T_c = 590$ K.

Figure 5-11 shows magnetometry measurement of MnSb on graphene/Cu. In our study, measurements of M vs H were taken at a fixed temperature of 10 K and 300 K while M vs T measurements were taken at a fixed field of 3000 Oe. The shape of the curve is indicative of hard axis behaviour, while the coercive field is (667 ± 5) Oe at 300 K and (900 ± 20) Oe at 10 K. SQUID measurements also show that the magnetic field is aligned out of plane which results in the field being aligned with the sample load area which is located at the top of the magnetometer. This study only sees hysteresis loop for thicker sample – 28 nm. Thinner samples ended up with no magnetic response being detected. SQUID measurement showed that the MnSb film is ferromagnetic at room temperature.

Summary of the nominal thickness to Mn percentage from XPS is plotted as in Figure 5-12.

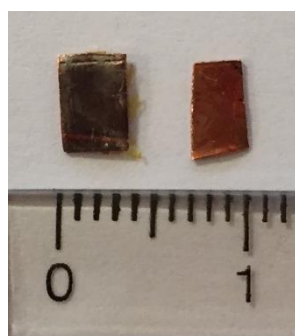
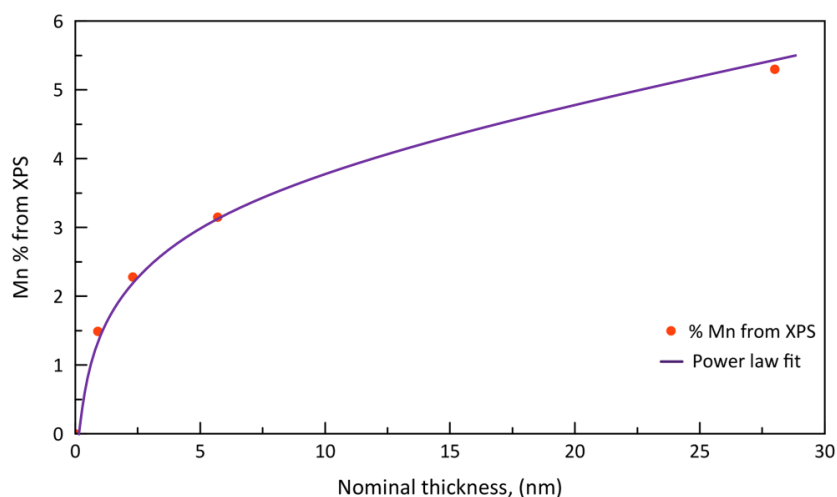


Figure 5-12: Top panel is a nominal thickness for set of samples versus Mn percentage from XPS, bottom panel is the condition after MBE growth for 28 nm and 1.6 nm nominal thickness, left and right respectively.

Top panel of Figure 5-12 shows a Mn percentage to nominal thickness for MnSb on graphene/Cu for different samples. This is well below linear, as expected for clusters as explained in Figure 5-3. When the x-ray beam focused on the Mn surface, the detector only count the electrons that have travel through the sample into the vacuum of the instrument. Mn layers will allow more photoelectrons passed through compare to Mn cluster due to its thickness. As the thickness

increase, the signals detected from the electron detector at the surface is much higher than the signals detected from deeper below the Mn surface. The exponential function become apparent as the depth increase. Thus, it is plausible that Mn clusters represent below liner with nominal thickness less than 10 nm as in Figure 5-12. Bottom panel displays the conditions of Cu plate after MBE growth. 28 nm plate changed to silver colour relatively to MnSb while 1.6 nm plate remained Cu original colour due to the minimum cluster of MnSb formed.

Discussion

The theoretical and experimental study of half-metallic ferromagnetic (HMF) materials remains interest among researchers. As our group had successfully growth MnSb on different single crystal semiconductor materials substrate, we had a presumably strong fundamental for understanding MnSb [34], [93], [94], [96]. As explained in Section 1.4, MnSb had three types of polymorphs. Experimental observation for the growth of MnSb(0001) thin film on GaAs(111) [34] represented multiple phases were formed during the thin film growth including surface reconstruction, atomic diffusion and the formation of secondary phase of *c-MnSb*. The *n-MnSb* epilayer is grown on GaAs(111) with a number of misfit dislocations near the surface.

In this study, some of the evidences from SEM and RHEED shows MnSb epitaxial growth is obtained with graphene, but this was not enough to deduce completely about epitaxy of MnSb on graphene/Cu. Other researcher had grown MnSb on graphite [104], [105]. We compare the morphology and surface structures and magnetic properties with ours.

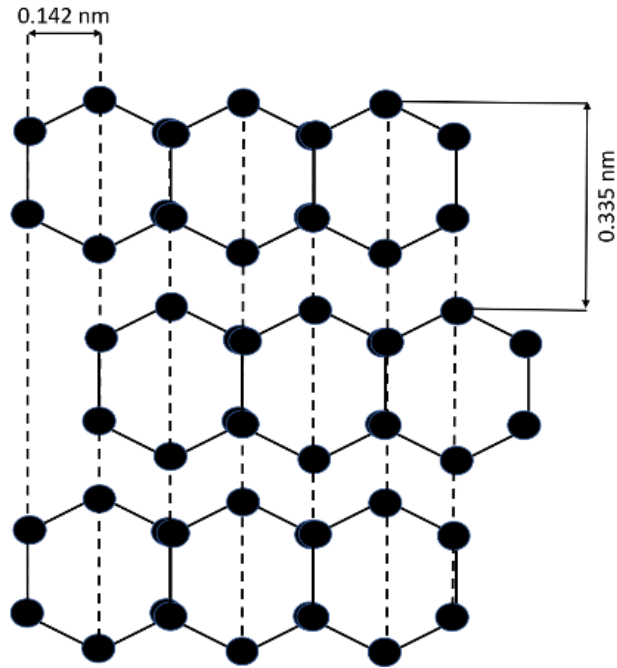


Figure 5-13: An illustration of graphite crystal structure. The dotted lines model the weak forces between the layers in graphite. The hexagonal unit cell is 0.142 nm and half the crystallographic c-axis spacing is 0.335 nm.

Figure 5-13 shows a graphite crystal structure. Graphite is known as a layered, planar structure [106]. The atoms are arranged in a few layers of hexagonal pattern with unit cell $c = 0.671 \text{ nm}$ and $a = 0.246 \text{ nm}$ [107]. Graphite consists of few layers of graphene. In graphite, there are three carbons atom connected with each carbon atom by covalent bond (Figure 5-13). There is one non-bonded outer electron left and becomes delocalised and its free to move through the structure. This behaviour influences graphite as conductor. The carbon layers are bound in the c -direction by weak van der Waals forces, [106].

Zhang et.al [105] confirmed the MnSb nanocrystalline were formed on highly oriented pyrolytic graphite (HOPG) along the step edges. The STM images revealed 2×2 and $(2\sqrt{3} \times 2\sqrt{3})R30^\circ$ reconstructions on the MnSb(0001) surface

and a 2×1 superstructure on $\text{MnSb}(10\bar{1}1)$. The surface morphology from our sample is quite similar with nanocrystalline formed along facet features as shown in Figure 5.2(d). If the non-bonded outer electrons are free to move and acted such as a single layer on graphene, presumably our sample can be identified with similar surface reconstructions. STM has not been carried out in our study due to high RMS roughness approximately at 20 nm to 30 nm for (40 x 40) micron image size. As we can see in AFM image Figure 5-2(c), MnSb nanocrystalline sizes are the range of several hundreds nm. The STM resolution is up to 1.0 nm which is smaller than our MnSb islands.

5.4 Summary

The growth of MnSb on graphene/Cu layers has been investigated over a range of thickness with growth time at constant growth rate. The growths are successfully enabled with MBE method. Surface topology revealed a textured nano-crystallites structure. It demonstrated 90% coverage of denser nano-crystallites at longer growth time with a nominal thickness 28 nm compared to a thin nominal thickness 1.6 nm which were too isolated.

Chapter 6: Graphene on Cu single crystal

6.1 Introduction

It is a general phenomenon that faceting can appear in all substrate where graphene is covered as a thin film. Facet is found to be able to minimise graphene's bending energy as it driven by the overlayer in the vicinity of steps [51]. In Chapter 4, we have seen faceting on our Cu plate. As the Cu plate has a complex grain structures with polycrystalline behaviour, crystal structure (hkl) is yet hard to be identified. Unlike the Cu foil which has been produced by roll-based method [73], the tendency of having one consistent direction as Cu(100) became higher. In our Cu foil study, facets occurred almost at (100) and (210) direction [38]. By combining both theory and experimental results of Cu foil, we should see facets on rigid substrate (Cu plate) and this has been proven with LEED, EBSD and AFM in Chapter 4. We see an interesting preliminary works to be applied for Cu single crystal in (n10) direction and the sample is immediate availability in storage. This chapter reports a study of graphene growth on a flat single crystal oriented along Cu(100) and Cu(410). All samples were investigated and analysed with SEM, Raman and LEED.

6.2 Experimental details

The samples are Cu single crystals that had been used for a wide variety of surface science experiments and stored in ambient air for several years. Using the 4-step preparation method as Cu plate, graphene was grown by the CVD technique

with similar growth conditions as explained in Chapter 4. The samples were taken through air transfer for SEM, Raman and LEED measurements.

6.3 Results and discussion

Using the same growth conditions, we expected that bulk single crystal experienced a full coverage of graphene monolayer. This was confirmed with Raman measurement.

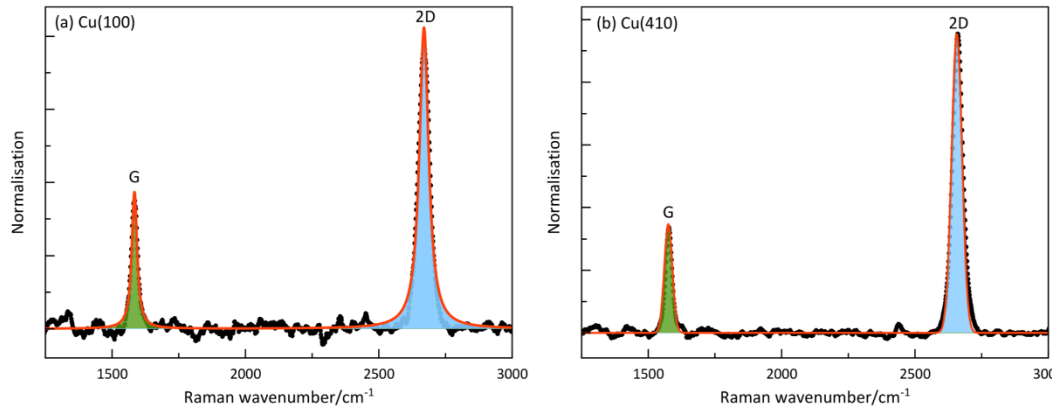


Figure 6-1: Raman spectra for (a) Cu(100) and (b) Cu(410) after 30 mins anneal and 20 mins graphene growth in CVD

Raman spectrum for both bulk Cu single crystals are represented in Figure 6-1(a) and (b). The measurements were carried out as explained in Figure 4-1. In both figures, the 2D/G ratio lies between 2-4 range as expected graphene monolayer had covered almost the whole Cu single crystal's surface. A Raman spectrum of graphene on Cu showing the G peak and 2D peak typical of monolayer graphene. The negligibly low D peak indicates low defect density in graphene and the high quality of the graphene samples [108].

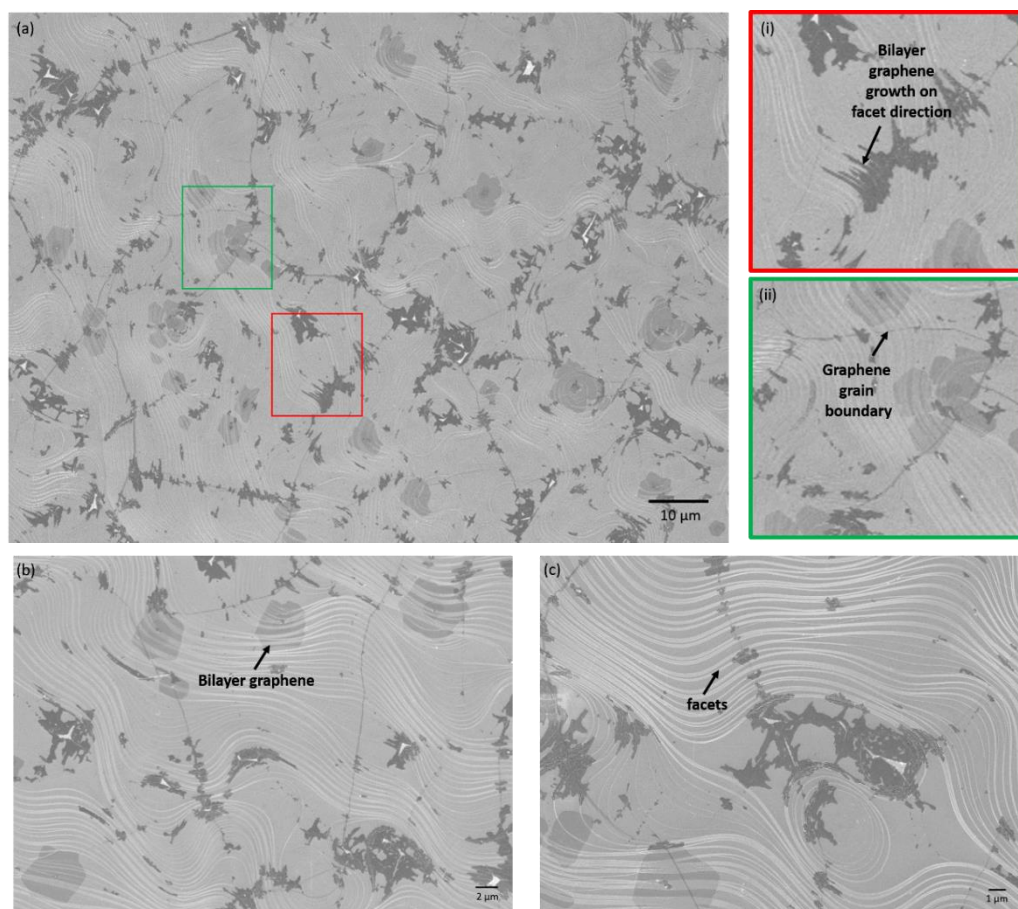


Figure 6-2: SEM images for Cu(100) with (a) low magnification with green and red a zoom in showed at (i) and (ii) respectively. (b) and (c) displays a higher magnification of the sample.

Figure 6-2 shows SEM images of the Cu(100). Monolayer graphene can be seen in panel (a), almost 85 to 90 % of the image represented with bright area while in contrast are some bilayer patches. No impurity spots detected as the 4-step preparation had successful produced clean bulk Cu single crystal. The bilayer graphene and meandering facets can be observed in panel (b) and (c). Some of the bilayer graphene (a)(i) growth on the facet direction. Panel (a)(ii) highlights the graphene grains boundaries that randomly appeared in between facet and bilayer

graphene. The facet on Cu(100) shows a lower initial step density compared to foil. The meandering facet is moving continuously on the surface as same Cu crystallography does not limit the structural feedback to form [38].

Figure 6-3 shows LEED pattern of Cu(100) from low to higher beam energy. It was observed that with an increase in the beam energy levels, the strength of the spots reduced and they diffused further. However, with beam energy reduction, the spots became clearer with less distortion of the spots. The change in the variation of these features arose due to structural effects of graphene in the samples. Regardless of the changes in the beam energy, some LEED spots do not change with the beam energy changes: these are referred to as (00) beams emanating from facets on an incline surface plane to Cu(100). Only a few images have been selected as a representative and used to show the trend throughout the various adjustments as shown in the Figure 6-3. At 35 eV, we can see 4 facet spots at Cu $\langle 100 \rangle$. An arc can be seen obviously at 40 and 45 eV and it came from the centre of the facet spots opposite of the arc. This arc is an azimuth ring in LEED. Different colours of facet spots showed the corresponding arc as in panel (b).

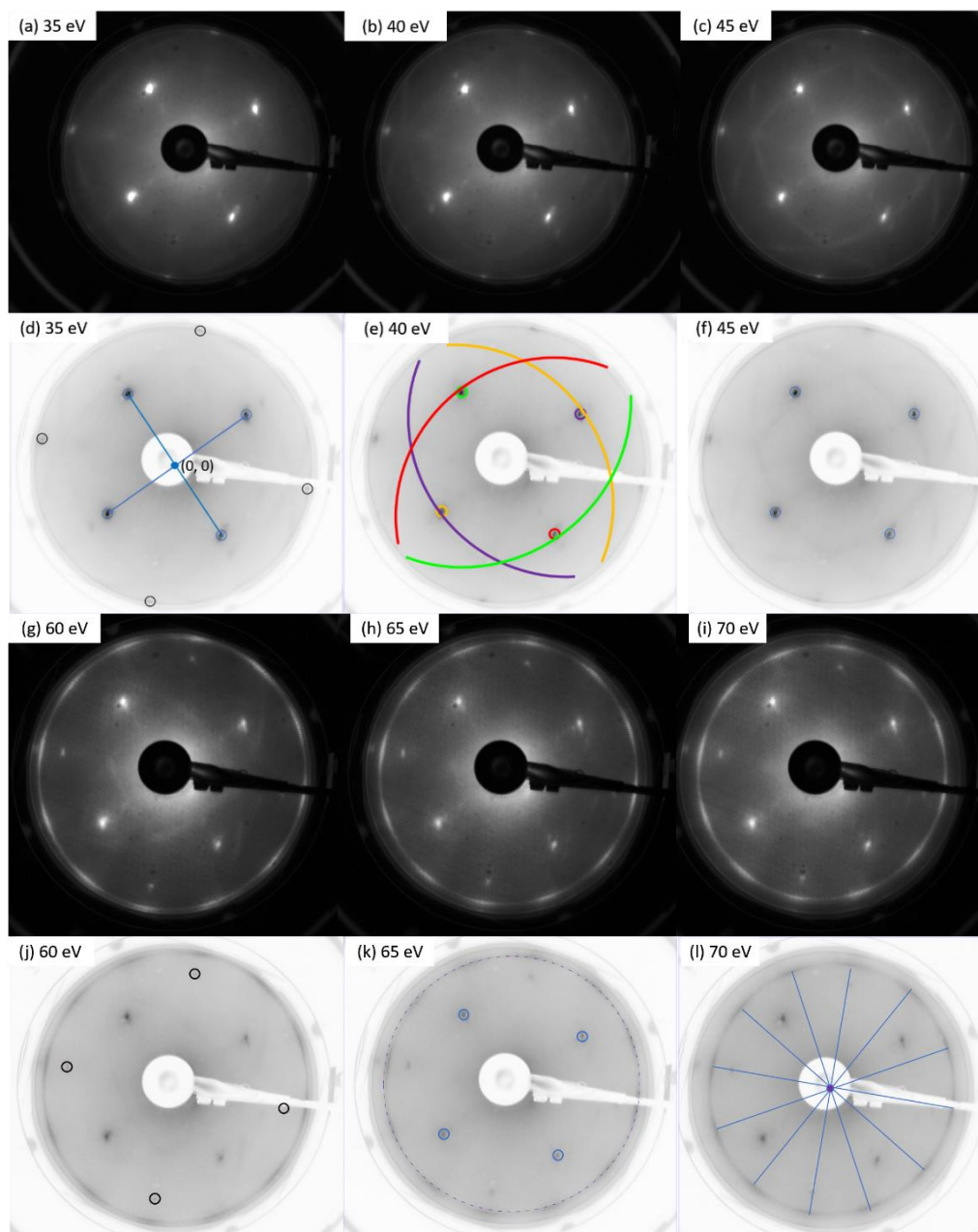


Figure 6-3: Cu(100) LEED patterns from graphene on Cu. (a), (b) and (c) are indexed in (d), (e) and (f) respectively shows graphene orientation preference. Panel (g), (h) and (i) are indexed in (j), (k), and (l) at a higher energy displaying how facets do not move with energy. Blue represents the expected reciprocal lattice of facet spots on Cu(100). Red, green, yellow and purple indicates the graphene rings related with facet Cu(100). (l) in blue line shows the 12 strong graphene spots

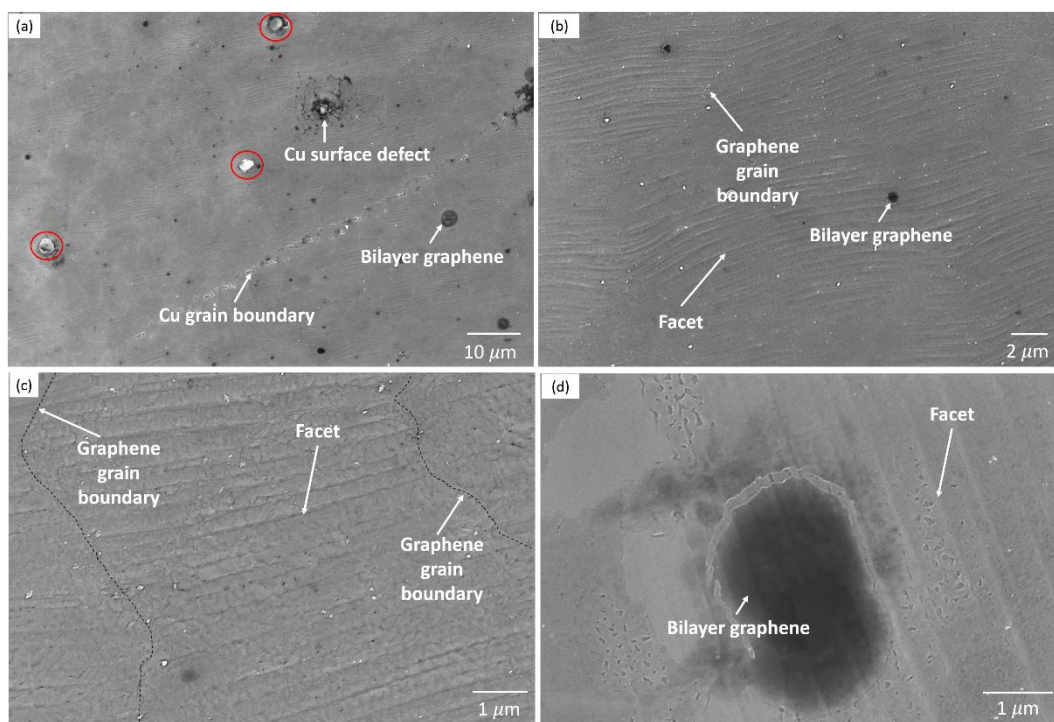


Figure 6-4: SEM images for Cu(410). Panel (a) is low magnification image and red circles represent impurity spots. Panel (b), (c) and (d) are details image with high magnifications and were taken at different spots of scan area. Darker region marks as bilayer graphene and black-dashed line is graphene grain boundaries.

Figure 6-4 shows SEM image for Cu(410). Panel (a) displays a low magnification image at approximate size of 90 μm x 60 μm with labels on the figure represents the bilayer graphene, Cu grain boundary and Cu surface defect. Cu surface defect was expected due to the initial physical conditions of bulk Cu after 4-steps surface preparation. A rough surface and some small dent or defect obviously can be seen. The green circles show impurity spots that come from bulk contamination from Cu while in CVD. In CVD quartz tube, some Cu residual from previous growth and contaminated the tube surface. It may react to the next sample growth. Regardless the defect while growing, Cu(410) showed in Figure

6.1(b) the surface covered with monolayer graphene. Some bilayer graphene with darker region scattered randomly on the sample. Panel (b) displays facets features and it continuously grows almost on the same direction. Ambiguous graphene grain boundary is highlighted with black-dashed line in Figure 6-4(c). Faceting features appeared in separation line between 1 μm to 2 μm . The density of facets are higher compare to Cu(100) as in Figure 6-2(a). Panel (d) shows a different scan area with some incomplete bilayer region appeared in between facets. It is plausible the facets appeared more in Cu(410) due to catalytic surface and more bilayer occurred compared to Cu(100) regardless the same growth conditions.

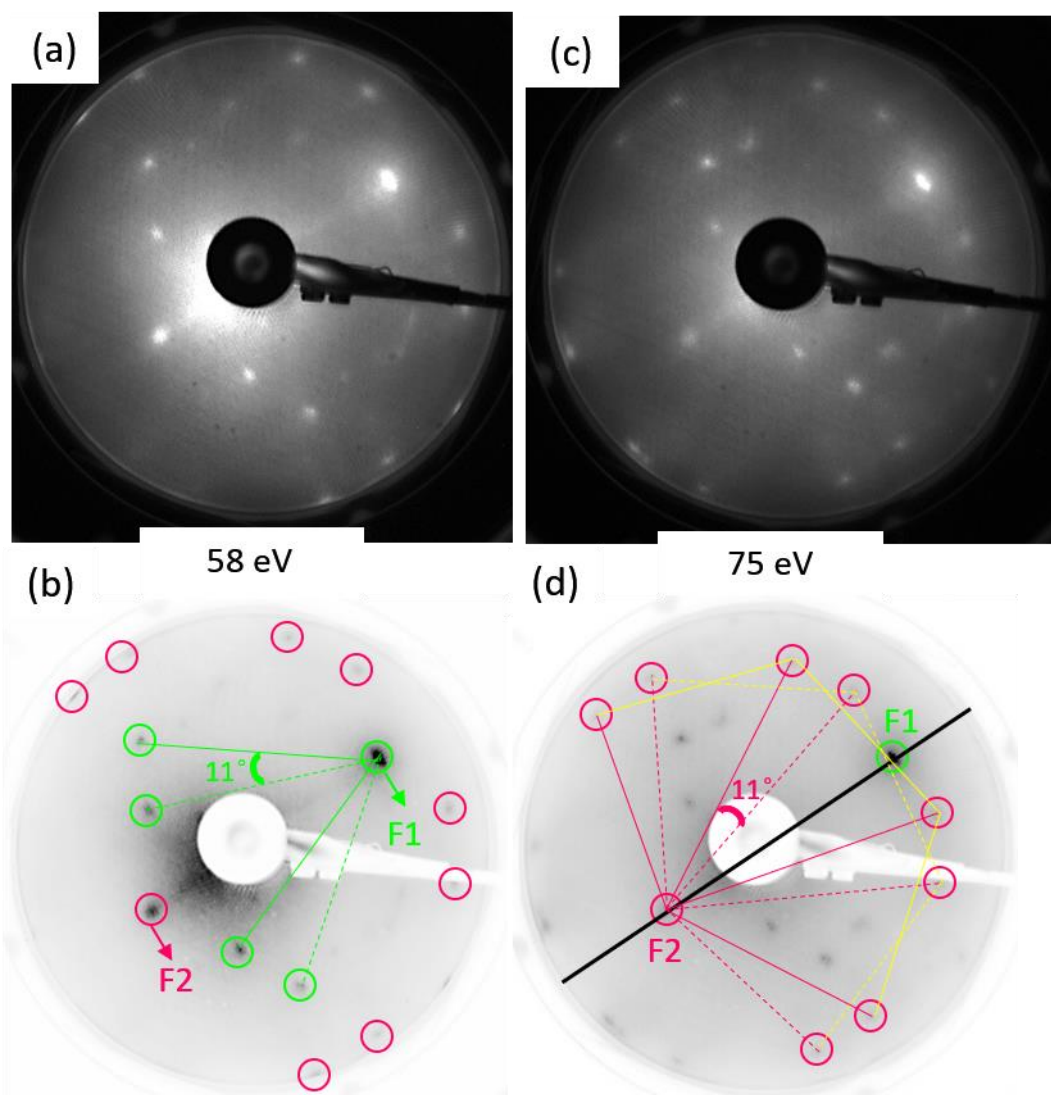


Figure 6-5: Cu(410) LEED patterns from graphene on Cu. (a) (indexed in (b)) shows graphene orientation preference. (b) (indexed in (d)) at a higher energy displaying how facet do not move with energy. F1 and F2 are two different facet points identified in the pattern. Green and pink circles are graphene spots correlate with F1 and F2 respectively. Black line is a mirror plane of 2-fold symmetry.

Figure 6-5 represents graphene on copper LEED pattern from Cu(410). Panel (a) and (b) were indexed and showed in (c) and (d) respectively. There are two facet points labelled as F1 (green circle) and F2 (pink circle). It was expected

as Cu(410) direction in mirror plane as 2-fold symmetry implying that these graphene surfaces are all perpendicular to the incident electron beam and parallel to each other. Two pairs of graphene domain spots are separated with dashed and solid line. Mismatch angle is measured between graphene domains and the value is $(11 \pm 2)^\circ$. Facet reflection showed it is not moving with energy in (c) where changing in wavelength did not give any effect to the facet point. F2 was indexed in (d) and apparently 4 pairs of graphene domains can be seen with half hexagonal pattern formed. There are no signs of Cu reconstruction spots. The angle between domains is 11° to 13° as distortion of the spot may influenced the measurement, but it is still acceptable within range as reported in [38]. This implies that each set of graphene spots actually comes from a large number of graphene grains [109].

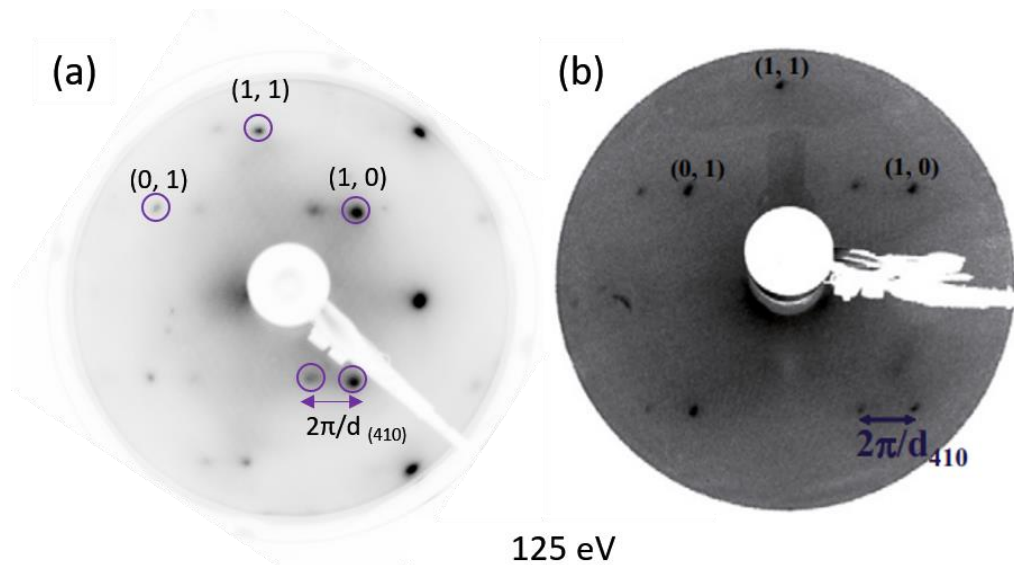


Figure 6-6: Cu(410) LEED pattern. (a) after ion-bombardment and annealing of the surface. (b) Reference LEED pattern from Valbuena et.al [110].

Figure 6-6(a) shows our LEED pattern after removing graphene with ion-bombardment and annealing. The surface is cleaned and left the crystal structure of the bulk Cu. No graphene spots were visible and it was consistent the treatment had removed graphene overlayer. We compare with study from Valbuena et.al and show in panel (b). We can see the square pattern represents the diffraction from Cu(410). The splitting distance labelled as $2\pi/d$ is consistent with the expected superperiodicity of the new regular step array [110]. Facet (00) spots were identified by monitoring spot movement with beam energy and were easy to observe due to their constant position on the screen as the electron energy was changed. The sample LEED movie (in AVI file format) steps through beam energies from 45 to 100 eV, and the non-moving facet spots to the left and right of the electron gun are clearly visible. A few extra spots with weaker density appear as symmetry indexing of $(\bar{1}, 0)$, $(1, 1)$, $(1, \bar{1})$ or $(\bar{1}, \bar{1})$.

6.4 Summary

This chapter can be summarised that graphene on Cu does not like to stay at steps but more stable on facets. Graphene quality was confirmed by Raman spectrum with monolayer full coverage. Cu(100) experienced graphene growth in many orientations with tendency to simple domain epitaxy. Graphene is sitting on some Cu facets and in all directions even Cu crystallography oriented along (100) direction. In SEM (Figure 6.2), initial facet on large flat area of Cu(100) surface showed low steps density and consistent with bending energy argument. At high energy, we see simple domain of graphene in all order and four-fold symmetry as it should be. When graphene growth is started, strong energy push to smooth Cu surface. Cu(410) inherited with completely facets on the surface. When high energy is applied at the starting of steps density, graphene grows with higher facet coverage. After argon sputtering on Cu(410), it just reverted to the nice surface of single crystal. MnSb is not deposited on the graphene/Cu single crystal due to oversize compared to our MBE sample holder.

Chapter 7: Conclusions and future work

7.1. Conclusions

The evolution of high technology devices has powered up the development of simpler yet more efficient hardware. The interests in graphene as a highly functional material have been widely acknowledged. At present, many researchers are in active pursuit to further process and functionalise graphene to make it perform even better as a storage device. One example is to magnetise graphene through binding with another substrate.

Throughout this research, arrays of techniques have been utilised to study the structural, chemical and magnetic properties of MnSb thin films on graphene on Cu substrate. Beforehand, a detailed study for Cu substrate are carried out in the first experimental report in Chapter 3. An initial study has focused on how Cu foil substrate preparation can be applied to Cu plate. Research on Cu foil usage as substrate successfully produce a full coverage of monolayer graphene growth has already been established. Through them, we have managed to prepare a Cu plate that is 10 times thicker than Cu foil. Using 2-steps preparation of Cu foil on Cu plate, high density of impurity spots within an area was shown at an average of $2.2 \mu\text{m}^{-2}$ indicating quite serious contamination. The 4-steps preparation enhances the outcome of graphene growth. An acceptable graphene grain on Cu plate shows an average size between $10 \mu\text{m}$ to $40 \mu\text{m}$. The 4-steps preparation of Cu plate promises full coverage of monolayer graphene and low impurity spots density area after CVD growth.

The rigidity and flatness of Cu plate is crucial for MBE overgrown layer of graphene on Cu plate. This influence the RHEED in-situ reading since Cu foil surface can easily form wrinkles after being spot-weld on the substrate holder [41]. As a matter of substrate quality, Cu plate needs to get the best conditions before undergoing the overgrowth in MBE. The results in Chapter 4 indicate that the growth parameter in CVD at 30 minutes annealing and 20 minutes growth times result in epitaxial graphene films on Cu plate. The LEED analysis reveals the pattern of graphene rings and weak mismatch at $11^\circ \pm 2^\circ$ between two graphene domains. The RHEED analysis shows a straight line of shadow edge in Cu plate compare to Cu foil. It showed the rigidity of the Cu plate. A structural feedback or faceting on graphene films is not only limited to Cu foil but also appeared in our Cu plate. These facets are a signature feature on graphene growth. XPS elemental chemical analysis proves the C, O and Cu peaks fitted with associated binding energy of graphene layers.

Following Chapter 4 studies, graphene on Cu plate is ready for MBE to overgrown MnSb. Chapter 5 presents MBE growth of MnSb on graphene/Cu plate over a range of thickness. The surface topology of MnSb on graphene/Cu can be thought as a textured nano-crystallite at nominally 28 nm thickness while 1.6 nm displayed an isolated MnSb islands. In-situ RHEED reveals random diffraction streaks and spots and impossible for indexing on Cu plate before MnSb growth. This pattern matches with polycrystalline Cu texture. Post-growth RHEED analysis deducts the d-spacing of our sample to be 4.9 Å. While the reported d-spacing of MnSb(0001) is 5.79 Å. The difference plausibly influenced by tilted facet on graphene as discussed in LEED (Figure 4-3). SQUID as a magnetometry technique shows a hard axis behaviour with the coercive field is (667 ± 5) Oe at 300 K and (900 ± 20) Oe at 10K.

The final experiment of Cu single crystals is described in Chapter 6. A bulk Cu(100) and Cu(410) undergone graphene growth using the 4-steps preparation method. Both Cu single crystals have 2D/G peaks in Raman spectrum in ratio range of 2 to 4. It indicates monolayer graphene. The bulk single crystal gives promising quality of graphene as our plate with full coverage of monolayer and some bilayer regions in the SEM. The growth parameter in CVD remain the same as applied to Cu plate. SEM images reveal the meandering facets on Cu(100) in all directions. In contrast, Cu(410) facet has low density of steps. LEED pattern confirms epitaxial graphene on Cu(100) with graphene ring and three weak mismatch domains. While Cu(410) appears only with two mismatch domains graphene. The angle of separation for both Cu(100) and Cu(410) is $11^{\circ} \pm 2^{\circ}$. This preliminary study on Cu(100) and Cu(410) confirms a facet as signature features of graphene films occurs in our foil, plate and bulk single crystal.

7.2. Future work

MnSb epitaxial growth on graphene/Cu is promising with some of the analysis that has been reported here are not enough to deduce completely about MnSb polymorphs and their spintronic applications. These derive from both interfacial, for spin transport, and halfmetallic polymorph, for magnetometry, deliberations. Regarding the interface, the interaction of Mn with the surface of graphene is seen to be epitaxial and the substitution of Mn into the surface could act to form island nucleation. XRD has failed to detect the crystal structure on our sample. This limited our study on the nanocrystal orientation of MnSb. Some future works can be suggested to quantify MnSb

nanocrystal structure and epitaxy such as a transferable sample for tunnelling electron microscopy (TEM), synchrotron XRD and small-angle X-ray scattering (SAXS). Otherwise, if using the same XRD method, a thicker film than 28 nm should be grown.

MnSb is a promising ferromagnetic material. The magnetic strength of the sample may obscure the graphene layers that underlying by MnSb islands. SQUID is known as a precision technique with detection sensitivity of as low as 5×10^{-18} T. The magnetic signals from our sample presumably come as a consequence of strong magnetic fields of MnSb nanocrystal. To get the magnetic moment in graphene, x-ray magnetic circular dichroism (XMCD) can be suggested to this work provided that the sample is flat, smooth and clean.

We grew some thinner samples of less than 5 nm and no hysteresis loops was detected. The behaviour of MnSb thin film thickness in the range of between 5 nm to 25 nm is yet to be studied.

Appendix A

XPS Analysis For MnSb Other Samples

Introduction

This appendix outlines the XPS analysis performed on the growth of MnSb on graphene/Cu substrates with growth times varies at 0.5 min, 0.75 min, 1.25 min, and 3 mins. This work was performed at shorter times than the sample we presented in Chapter 5. All fitting were applied as explained in Chapter 5.

Sample	T_{sub} , (°C)	Nominal thickness, (nm)	Growth time, (min)	Sb capped
G006	200	5.69	3.0	Yes
G007	200	0.88	0.5	Yes
G008	200	1.61	0.75	Yes
G010	200	2.34	1.25	Yes

Table A-1: Growth conditions for all MnSb on graphene/Cu sample

Table A-1 shows a growth condition of all MnSb on graphene/Cu sample. These samples were grown after we got the hysteresis loops in SQUID for 28 nm. Figure (A-1), (A-2), (A-3) and (A-4) show XPS fitting spectra for C, O, Mn and shallow core of the sample.

C1s

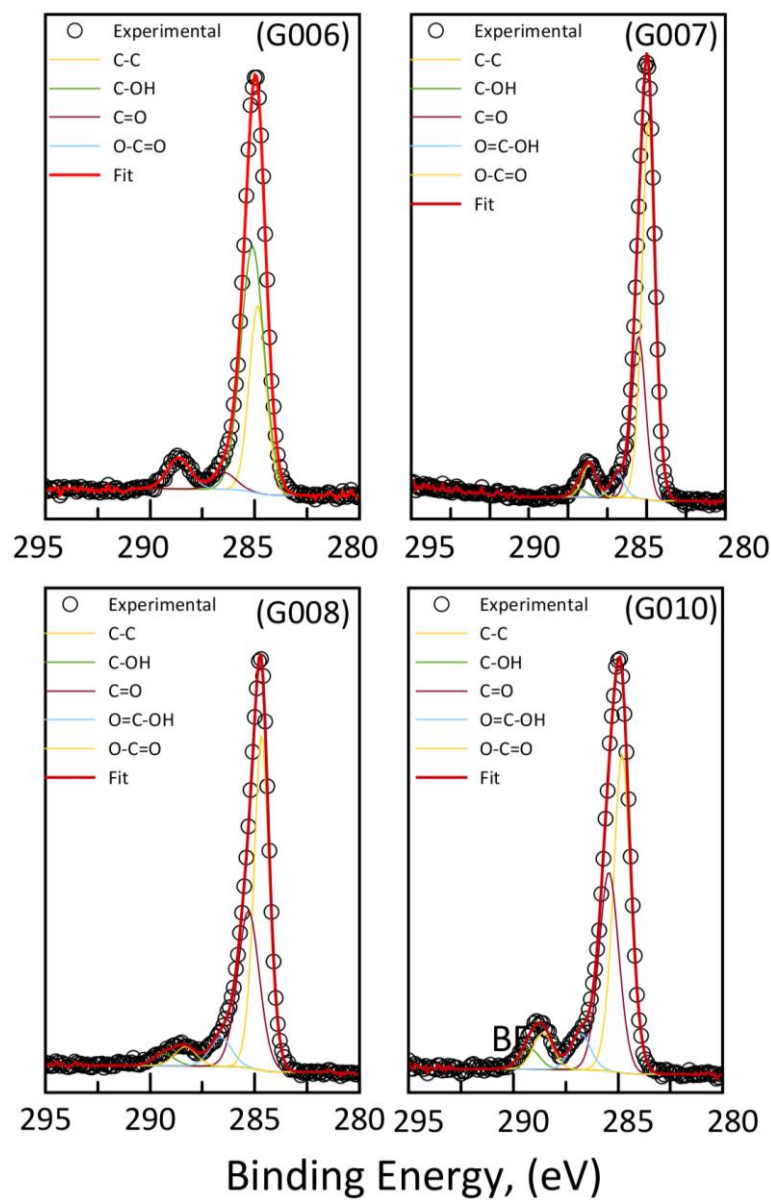


Figure A-A-1: C 1s for all MnSb on graphene/Cu sample.

O 1s

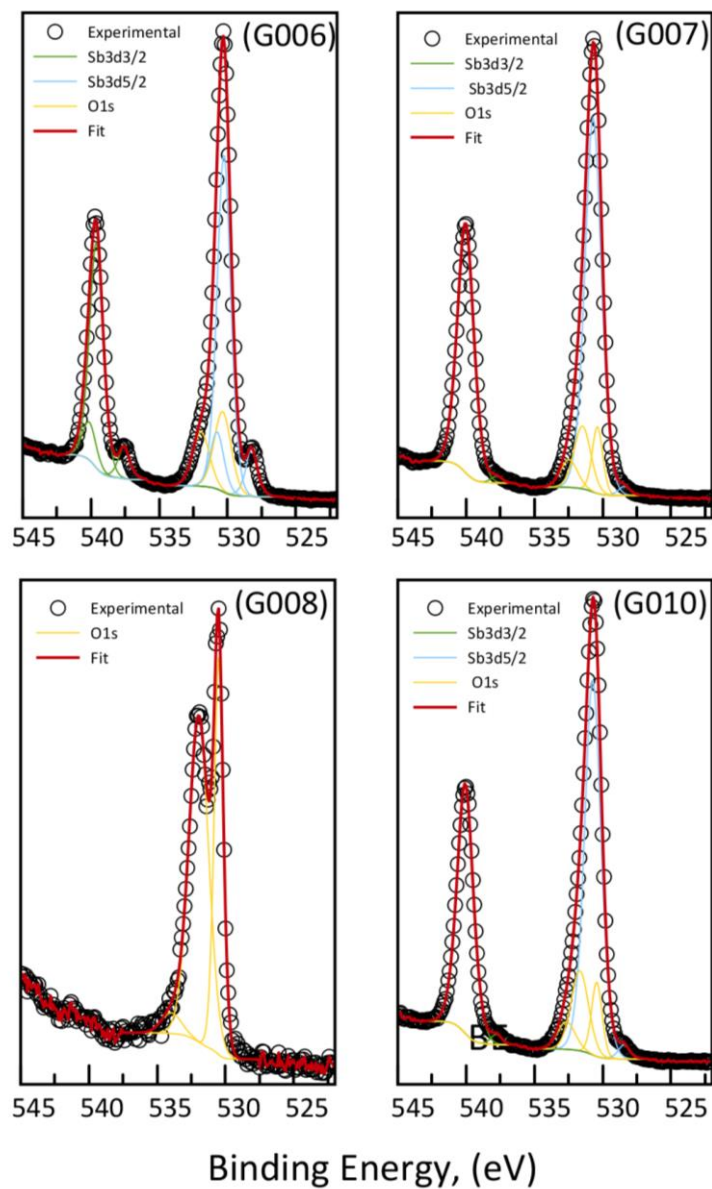


Figure A-A-2: O 1s for all MnSb on graphene/Cu sample.

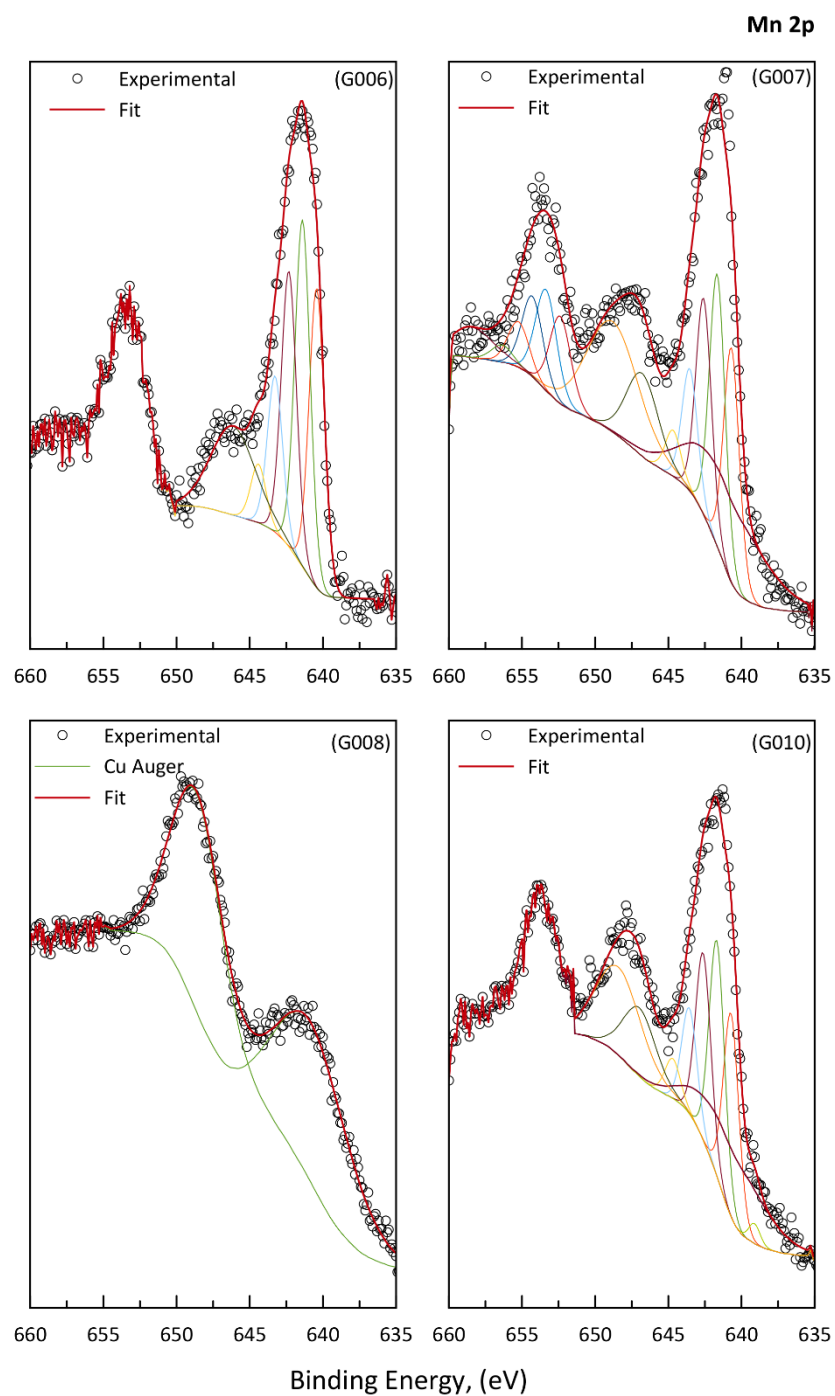


Figure A-A-3: Mn 2p for all MnSb on graphene/Cu sample.

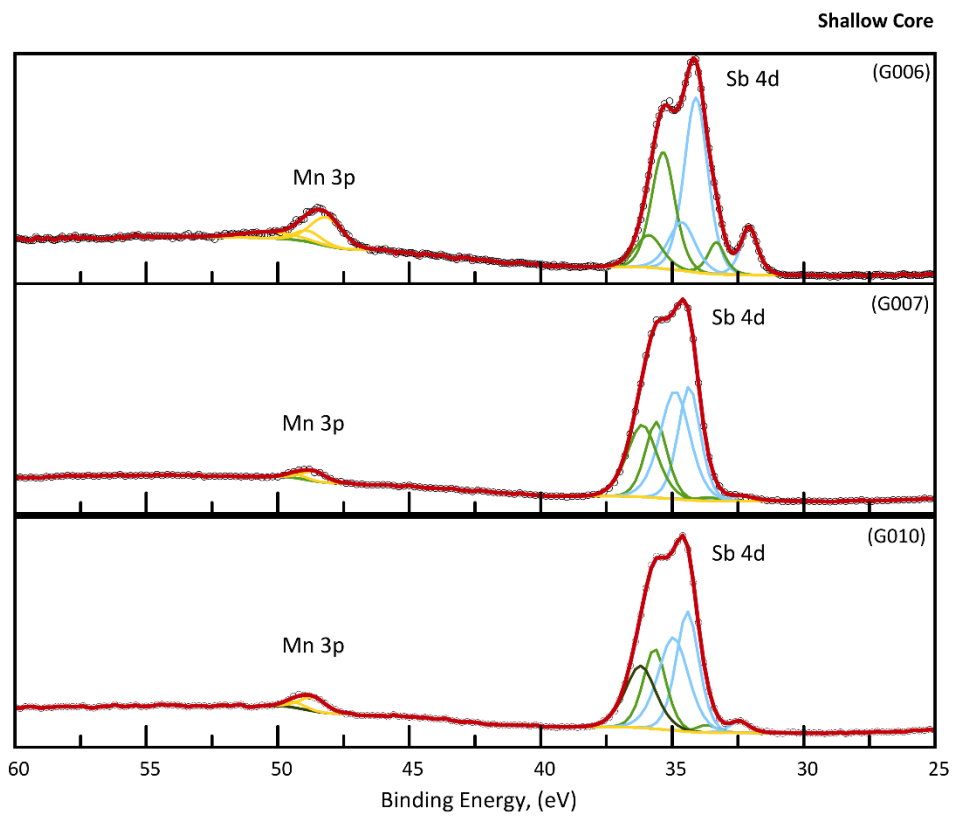


Figure A-4: Shallow core for all MnSb on graphene/Cu. For G008, no shallow core peaks was detected

References

- [1] M. Lundstrom, "Applied physics: Moore's law forever?," *Science (80-.)*, vol. 299, no. 5604, pp. 210–211, 2003.
- [2] G. E. Moore, "Cramming more components onto integrated circuits," *Proc. IEEE*, vol. 86, no. 1, pp. 82–85, 1998.
- [3] I. L. Markov, "Limits on fundamental limits to computation," *Nature*, vol. 512, no. 7513, pp. 147–154, 2014.
- [4] M. M. Waldrop, "The chips are down for Moore's law," *Nature*, vol. 530, no. 11 February 2016, pp. 144–147, 2016.
- [5] K. S. Novoselov *et al.*, "Electric field effect in atomically thin carbon films," *Science (80-.)*, vol. 306, pp. 666–669, 2004.
- [6] K. S. Novoselov, V. I. Fal'Ko, L. Colombo, P. R. Gellert, M. G. Schwab, and K. Kim, "A roadmap for graphene," *Nature*, vol. 490, no. 7419, pp. 192–200, 2012.
- [7] J. W. Suk *et al.*, "Transfer of CVD-grown monolayer graphene onto arbitrary substrates," *ACS Nano*, vol. 5, no. 9, pp. 6916–6924, 2011.
- [8] R. Mas-Ballesté, C. Gómez-Navarro, J. Gómez-Herrero, and F. Zamora, "2D materials: To graphene and beyond," *Nanoscale*, vol. 3, no. 1, pp. 20–30, 2011.
- [9] S. A. Wolf, "Spintronics: A spin-based electronics vision for the future," *Science (80-.)*, vol. 294, no. 5546, p. 1488, 2001.
- [10] W. K. Lee, K. E. Whitener, J. T. Robinson, and P. E. Sheehan, "Patterning

- magnetic regions in hydrogenated graphene via E-Beam Irradiation,” *Adv. Mater.*, vol. 27, no. 10, pp. 1774–1778, 2015.
- [11] B. Uchoa, V. N. Kotov, N. M. R. Peres, and A. H. Castro Neto, “Localized magnetic states in graphene,” *Phys. Rev. Lett.*, vol. 101, no. 2, pp. 1–4, 2008.
 - [12] M. Mizuguchi, H. Akinaga, K. Ono, and M. Oshima, “Magnetic properties of MnSb granular films,” *J. Magn. Magn. Mater.*, vol. 226–230, pp. 1838–1839, 2001.
 - [13] W. Q. Liu *et al.*, “Atomic-scale interfacial magnetism in Fe/graphene heterojunction,” *Sci. Rep.*, vol. 5, pp. 1–9, 2015.
 - [14] J. H. Warner *et al.*, “Graphene Fundamentals and emergent applications,” *Graphene*, vol. 17. pp. 1–4, 2013.
 - [15] A. H. . Castro Neto, N. M. R. . Peres, K. S. . Novoselov, A. K. . Geim, and F. Guinea, “The electronic properties of graphene,” *Rev. Mod. Phys.*, vol. 81, no. 1, pp. 109–162, 2009.
 - [16] A. H. Castro Neto, F. Guinea, N. M. R. Peres, K. S. Novoselov, and A. K. Geim, “The electronic properties of graphene,” *Rev. Mod. Phys.*, 2009.
 - [17] R. R. Nair *et al.*, “Fine structure constant defines visual transparency of graphene,” *Science (80-.)*, vol. 320, no. 5881, p. 1308, 2008.
 - [18] C. Lee, X. Wei, J. W. Kysar, and J. Hone, “Measurement of the elastic properties and intrinsic strength of monolayer graphene,” *Science (80-.)*, vol. 321, no. 5887, pp. 385–388, 2008.
 - [19] P. Zhang *et al.*, “Fracture toughness of graphene,” *Nat. Commun.*, vol. 5,

pp. 1–7, 2014.

- [20] P. O. Lehtinen, A. S. Foster, Y. Ma, A. V. Krasheninnikov, and R. M. Nieminen, “Irradiation-induced magnetism in graphite: A density functional study,” *Phys. Rev. Lett.*, vol. 93, no. 18, 2004.
- [21] V. M. Pereira, F. Guinea, J. M. B. Lopes Dos Santos, N. M. R. Peres, and A. H. Castro Neto, “Disorder induced localized states in graphene,” *Phys. Rev. Lett.*, vol. 96, no. 3, 2006.
- [22] P. Society and T. P. Society, “Nonmagnetic-Defect-Induced Magnetism in Graphene,” *J. Phys. Soc. Japan*, vol. 76, no. 6, pp. 1–5, 2007.
- [23] J. J. Palacios, J. Fernández-Rossier, and L. Brey, “Vacancy-induced magnetism in graphene and graphene ribbons,” *Phys. Rev. B - Condens. Matter Mater. Phys.*, vol. 77, no. 19, 2008.
- [24] R. Singh and P. Kroll, “Magnetism in graphene due to single-atom defects: Dependence on the concentration and packing geometry of defects,” *J. Phys. Condens. Matter*, vol. 21, no. 19, 2009.
- [25] A. V. Krasheninnikov, P. O. Lehtinen, A. S. Foster, P. Pyykk, and R. M. Nieminen, “Embedding transition-metal atoms in graphene: Structure, bonding, and magnetism,” *Phys. Rev. Lett.*, vol. 102, no. 12, 2009.
- [26] K. Harigaya, Y. Kobayashi, K. Takai, J. Ravier, and T. Enoki, “Novel electronic wave interference patterns in nanographene sheets,” *J. Phys. Condens. Matter*, vol. 14, no. 36, 2002.
- [27] Y. W. Son, M. L. Cohen, and S. G. Louie, “Half-metallic graphene nanoribbons,” *Nature*, vol. 444, no. 7117, pp. 347–349, 2006.

- [28] E. J. Kan, Z. Li, J. Yang, and J. G. Hou, "Half-metallicity in edge-modified zigzag graphene nanoribbons," *J. Am. Chem. Soc.*, vol. 130, no. 13, pp. 4224–4225, 2008.
- [29] M. A. Akhukov, A. Fasolino, Y. N. Gornostyrev, and M. I. Katsnelson, "Dangling bonds and magnetism of grain boundaries in graphene," *Phys. Rev. B - Condens. Matter Mater. Phys.*, vol. 85, no. 11, 2012.
- [30] S. S. Alexandre, A. D. Lcio, A. H. C. Neto, and R. W. Nunes, "Correlated magnetic states in extended one-dimensional defects in graphene," *Nano Lett.*, vol. 12, no. 10, pp. 5097–5102, 2012.
- [31] J. Berashevich and T. Chakraborty, "Sustained ferromagnetism induced by H-vacancies in graphane," *Nanotechnology*, vol. 21, no. 35, 2010.
- [32] E. V. Castro, N. M. R. Peres, J. M. B. Lopes Dos Santos, A. H. C. Neto, and F. Guinea, "Localized states at zigzag edges of bilayer graphene," *Phys. Rev. Lett.*, vol. 100, no. 2, 2008.
- [33] E. H. Lieb, "Two theorems on the Hubbard model," *Phys. Rev. Lett.*, vol. 62, no. 10, pp. 1201–1204, 1989.
- [34] J. D. Aldous *et al.*, "Cubic MnSb: Epitaxial growth of a predicted room temperature half-metal," *Phys. Rev. B - Condens. Matter Mater. Phys.*, vol. 85, no. 6, 2012.
- [35] S. A. Hatfield and G. R. Bell, "Growth by molecular beam epitaxy and interfacial reactivity of MnSb on InP(0 0 1)," *J. Cryst. Growth*, vol. 296, no. 2, pp. 165–173, 2006.
- [36] J. E. Pask, L. H. Yang, C. Y. Fong, W. E. Pickett, and S. Dag, "Six low-strain zinc-blende half metals: An ab initio investigation," *Phys. Rev. B - Condens.*

Matter Mater. Phys., vol. 67, no. 22, 2003.

- [37] H. Akinaga, S. Miyanishi, W. Van Roy, and L. H. Kuo, "Structural and magnetic properties of epitaxial (0001) MnSb thin films grown on (111) B GaAs: Influence of interface quality," *Appl. Phys. Lett.*, vol. 70, no. 18, pp. 2472–2474, 1997.
- [38] N. R. Wilson *et al.*, "Weak mismatch epitaxy and structural Feedback in graphene growth on copper foil," *Nano Res.*, vol. 6, no. 2, pp. 99–112, 2013.
- [39] R. L. Park and H. H. Madden, "Annealing changes on the (100) surface of palladium and their effect on CO adsorption," *Surf. Sci.*, vol. 11, no. 2, pp. 188–202, 1968.
- [40] E. A. Wood, "Vocabulary of surface crystallography," *J. Appl. Phys.*, vol. 35, no. 4, pp. 1306–1312, 1964.
- [41] P. J. Mousley, C. W. Burrows, M. J. Ashwin, M. Takahasi, T. Sasaki, and G. R. Bell, "In situ X-ray diffraction of GaAs/MnSb/Ga(In)As heterostructures," *Phys. Status Solidi Basic Res.*, vol. 254, no. 2, 2017.
- [42] X. Li *et al.*, "Large-area graphene single crystals grown by low-pressure chemical vapor deposition of methane on copper," *J. Am. Chem. Soc.*, vol. 133, no. 9, pp. 2816–2819, 2011.
- [43] C. V. Deposition, "The fundamentals of chemical vapour deposition," *J. Mater. Sci.*, 1977.
- [44] O. Frank and M. Kalbac, "Chemical vapor deposition (CVD) growth of graphene films," *Graphene Prop. Prep. Characterisation Devices*, no. Cvd, pp. 27–49, 2014.

- [45] X. Li *et al.*, “Large-area synthesis of high-quality and uniform graphene films on copper foils,” *Science* (80-.), vol. 324, no. 5932, pp. 1312–1314, 2009.
- [46] K. S. Kim *et al.*, “Large-scale pattern growth of graphene films for stretchable transparent electrodes,” *Nature*, vol. 457, no. 7230, pp. 706–710, 2009.
- [47] K. Celebi *et al.*, “Evolutionary kinetics of graphene formation on copper,” *Nano Lett.*, vol. 13, no. 3, pp. 967–974, 2013.
- [48] L. Liu *et al.*, “A systematic study of atmospheric pressure chemical vapor deposition growth of large-area monolayer graphene,” *J. Mater. Chem.*, vol. 22, pp. 1498–1503, 2012.
- [49] A. M. Lewis, B. Derby, and I. A. Kinloch, “Influence of gas phase equilibria on the chemical vapor deposition of graphene,” *ACS Nano*, vol. 7, no. 4, pp. 3104–3117, 2013.
- [50] I. Vlassiouk *et al.*, “Role of hydrogen in chemical vapor deposition growth of large single-crystal graphene,” *ACS Nano*, vol. 5, no. 7, pp. 6069–6076, 2011.
- [51] D. Yi *et al.*, “What Drives Metal-Surface Step Bunching in Graphene Chemical Vapor Deposition?,” *Phys. Rev. Lett.*, vol. 120, no. 24, p. 246101, 2018.
- [52] H. Xin and W. Li, “A review on high throughput roll-to-roll manufacturing of chemical vapor deposition graphene,” *Appl. Phys. Rev.*, vol. 5, no. 3, 2018.
- [53] A. Y. Cho, J. R. Arthur, B. Laboratories, M. Hill, and I. Introduction, “Pii:

0079-6786(75)90005-9," vol. 10, pp. 1–35, 2002.

- [54] M. A. H. and H. Sitter, *Molecular Beam Epitaxy - Fundamentals and Current Status*. Springer-Verlag, 1989.
- [55] D. R. Lide, "CRC Handbook of Chemistry and Physics, 84th Edition, 2003-2004," *Handb. Chem. Phys.*, 2003.
- [56] J. R. Arthur, "Interaction of Ga and As₂ molecular beams with GaAs surfaces," *J. Appl. Phys.*, vol. 39, no. 8, pp. 4032–4034, 1968.
- [57] R. S. Wagner and W. C. Ellis, "Vapor-liquid-solid mechanism of single crystal growth," *Appl. Phys. Lett.*, 1964.
- [58] T. I. Kamins, R. S. Williams, D. P. Basile, T. Hesjedal, and J. S. Harris, "Ti-catalyzed Si nanowires by chemical vapor deposition: Microscopy and growth mechanisms," *J. Appl. Phys.*, vol. 89, p. 1008, 2001.
- [59] W. Braun, A. Trampert, V. M. Kaganer, B. Jenichen, D. K. Satapathy, and K. H. Ploog, "Endotaxy of MnSb into GaSb," *J. Cryst. Growth*, vol. 301–302, no. SPEC. ISS., pp. 50–53, 2007.
- [60] A. Ichimiya and P. I. Cohen, *Reflection High Energy Electron Diffraction*. UK: Cambridge University Press, 2004.
- [61] R. L. Park, J. E. Houston, and D. G. Schreiner, "The LEED instrument response function," *Rev. Sci. Instrum.*, vol. 42, no. 1, pp. 60–65, 1971.
- [62] G. Binnig and C. F. Quate, "Atomic Force Microscope," *Phys. Rev. Lett.*, vol. 56, no. 9, p. 930, 1986.
- [63] A. J. Schwartz, M. Kumar, B. L. Adams, and D. P. Field, *Electron backscatter diffraction in materials science*. 2009.

- [64] A. J. Wilkinson, D. J. Dingley, and G. Meaden, "Strain mapping using electron backscatter diffraction," in *Electron Backscatter Diffraction in Materials Science*, 2009.
- [65] S. Tanuma, C. J. Powell, and D. R. Penn, "Calculations of electron inelastic mean free paths. VIII. Data for 15 elemental solids over the 50-2000 eV range," *Surf. Interface Anal.*, vol. 37, no. 1, pp. 1–14, 2005.
- [66] D. A. Shirley, "High Resolution X-ray Photoemission Spectrum of The Valence Bands of Gold," *Phys. Rev. B*, vol. 5, no. 12, p. 4709, 1971.
- [67] "CasaXPS: Processing Software for XPS, AES, SIMS and More." [Online]. Available: <http://www.casaxps.com>.
- [68] N. John and S. George, "Raman Spectroscopy," in *Spectroscopic Methods for Nanomaterials Characterization*, 2017.
- [69] M. Hulman, "Raman spectroscopy of graphene," *Graphene Prop. Prep. Characterisation Devices*, pp. 156–183, 2014.
- [70] X. Wang, J. W. Christopher, and A. K. Swan, "2D Raman band splitting in graphene: Charge screening and lifting of the K-point Kohn anomaly," *Sci. Rep.*, no. 7, p. 13539, 2017.
- [71] A. C. Ferrari *et al.*, "Raman spectrum of graphene and graphene layers," *Phys. Rev. Lett.*, vol. 97, no. 18, 2006.
- [72] X. Li *et al.*, "Graphene films with large domain size by a two-step chemical vapor deposition process," *Nano Lett.*, vol. 10, no. 11, pp. 4328–4334, 2010.
- [73] S. Bae *et al.*, "Roll-to-roll production of 30-inch graphene films for

- transparent electrodes,” *Nat. Nanotechnol.*, vol. 5, no. 8, pp. 574–578, 2010.
- [74] A. C. Ferrari *et al.*, “Raman spectrum of graphene and graphene layers,” *Phys. Rev. Lett.*, vol. 97, no. 18, pp. 1–4, 2006.
- [75] M. H. Park, T. H. Kim, and C. W. Yang, “Thickness contrast of few-layered graphene in SEM,” *Surf. Interface Anal.*, vol. 44, no. 11–12, pp. 1538–1541, 2012.
- [76] A. Reina *et al.*, “Large area, few-layer graphene films on arbitrary substrates by chemical vapor deposition,” *Nano Lett.*, vol. 9, no. 1, pp. 30–35, 2009.
- [77] X. Jining and J. . Spallas, “Different Contrast Mechanisms in SEM Imaging of Graphene Application Note,” *Agilent Technologies*, 2012. [Online]. Available: <http://www.toyo.co.jp/files/user/img/product/microscopy/pdf/5991-0782EN.pdf>.
- [78] L.-Y. Lin, D.-E. Kim, W.-K. Kim, and S.-C. Jun, “Friction and wear characteristics of multi-layer graphene films investigated by atomic force microscopy,” *Surf. Coatings Technol.*, vol. 205, no. 20, pp. 4864–4869, 2011.
- [79] X. Li *et al.*, “Large area synthesis of high quality and uniform graphene films on copper foils,” *Science (80-.)*, vol. 324, no. 5932, pp. 1312–1314, 2009.
- [80] Q. Yu, S. Siriponglert, S.-S. Pei, J. Lian, H. Li, and Y. P. Chen, “Graphene segregated on Ni surfaces and transferred to insulators,” *Appl. Phys. Lett.*,

vol. 93, no. 11, 2008.

- [81] A. J. Marsden *et al.*, "Is graphene on copper doped?," *Phys. Status Solidi - Rapid Res. Lett.*, vol. 7, no. 9, pp. 643–646, 2013.
- [82] "XPS Simplified Carbon." [Online]. Available: <https://xpssimplified.com/elements/carbon.php>.
- [83] J. R. Rumble, D. M. Bickham, and C. J. Powell, "The NIST x-ray photoelectron spectroscopy database," *Surf. Interface Anal.*, 1992.
- [84] "XPS Simplified Cooper." [Online]. Available: <https://xpssimplified.com/elements/copper.php>.
- [85] "XPS Simplified Oxygen." [Online]. Available: <https://xpssimplified.com/elements/oxygen.php>.
- [86] Casa XPS, "Basic Quantification of XPS Spectra," *CasaXPS Softw. user's Man.*, 2008.
- [87] T. Chen, J. C. Mikkelsen, and G. B. Charlan, "Crystal growth and crystal chemistry of NiAs-type compounds: MnSb, CoSb, and NiSb," *J. Cryst. Growth*, vol. 43, no. 1, pp. 5–12, 1978.
- [88] H. Tatsuoka *et al.*, "Growth of epitaxial ferromagnetic MnSb layers by hot-wall epitaxy Growth of epitaxial ferromagnetic MnSb layers by hot-wall epitaxy," vol. 2190, pp. 1–4, 1995.
- [89] B. L. Low *et al.*, "Morphology and magnetic analysis of MnSb films grown by hot-wall epitaxy," *J. Appl. Phys.*, vol. 84, no. 2, pp. 973–977, 1998.
- [90] H. Tatsuoka, K. Isaji, H. Kuwabara, Y. Nakanishi, T. Nakamura, and H. Fujiyasu, "Growth of epitaxial MnSB layers on Si substrates by hot-wall

- epitaxy," *Appl. Surf. Sci.*, vol. 113–114, pp. 48–52, 1997.
- [91] S. A. Hatfield and G. R. Bell, "Mapping the surface reconstructions of MnSb(0 0 0 1) and $(1\bar{1}0\ 0\ 1)$," *Surf. Sci.*, vol. 601, no. 23, pp. 5368–5377, 2007.
- [92] H. Tatsuoka, H. Kuwabara, M. Oshita, Y. Nakanishi, T. Nakamura, and H. Fujiyasu, "Structural characterization of epitaxial ferromagnetic MnSb layers grown by hot-wall epitaxy," *Appl. Surf. Sci.*, vol. 92, pp. 382–386, 1996.
- [93] J. D. Aldous *et al.*, "Depth-dependent magnetism in epitaxial MnSb thin films: Effects of surface passivation and cleaning," *J. Phys. Condens. Matter*, vol. 24, no. 14, 2012.
- [94] I. Maskery *et al.*, "Bulk crystal growth and surface preparation of NiSb, MnSb, and NiMnSb," *J. Vac. Sci. Technol. B Nanotechnol. Microelectron.*, vol. 34, no. 4, 2016.
- [95] J. D. Aldous *et al.*, "Growth and characterisation of NiSb(0001)/GaAs(111)B epitaxial films," *J. Cryst. Growth*, vol. 357, no. 1, pp. 1–8, 2012.
- [96] C. W. Burrows *et al.*, "Heteroepitaxial growth of ferromagnetic MnSb(0001) films on Ge/Si(111) virtual substrates," *Cryst. Growth Des.*, vol. 13, no. 11, pp. 4923–4929, 2013.
- [97] J. Donohue, *The Structures of The Elements*. Malabar, R. E. Krieger, 1982, 1982.
- [98] M. C. Biesinger, B. P. Payne, A. P. Grosvenor, L. W. M. Lau, A. R. Gerson, and R. S. C. Smart, "Resolving surface chemical states in XPS analysis of first row transition metals, oxides and hydroxides: Cr, Mn, Fe, Co and Ni,"

Appl. Surf. Sci., vol. 257, no. 7, pp. 2717–2730, 2011.

- [99] B. L. Low, C. K. Ong, J. Lin, A. C. H. Huan, H. Gong, and T. Y. F. Liew, "Structure and magnetization of MnSb thin films deposited at different substrate temperatures," *J. Appl. Phys.*, vol. 85, no. 10, pp. 7340–7344, 1999.
- [100] J. Liu, M. P. Hanson, J. A. Peters, and B. W. Wessels, "Magnetism and Mn Clustering in (In,Mn)Sb Magnetic Semiconductors," *ACS Appl. Mater. Interfaces*, vol. 7, no. 43, pp. 24159–24167, 2015.
- [101] E. S. Ilton, J. E. Post, P. J. Heaney, F. T. Ling, and S. N. Kerisit, "XPS determination of Mn oxidation states in Mn (hydr)oxides," *Appl. Surf. Sci.*, vol. 366, pp. 475–485, 2016.
- [102] E. S. Ilton, J. E. Post, P. J. Heaney, F. T. Ling, and S. N. Kerisit, "XPS determination of Mn oxidation states in Mn (hydr)oxides," *Appl. Surf. Sci.*, vol. 366, pp. 475–485, 2016.
- [103] F. Garbassi, "XPS and AES study of antimony oxides," *Surf. Interface Anal.*, 1980.
- [104] S. S. Kushvaha, H. L. Zhang, Z. Yan, A. T. S. Wee, and X. S. Wang, "Growth of self-assembled Mn, Sb and MnSb nanostructures on highly oriented pyrolytic graphite," *Thin Solid Films*, vol. 520, no. 23, pp. 6909–6915, 2012.
- [105] H. Zhang, S. S. Kushvaha, A. T. S. Wee, and X. Sen Wang, "Morphology, surface structures, and magnetic properties of MnSb thin films and nanocrystallites grown on graphite," *J. Appl. Phys.*, vol. 102, no. 2, 2007.
- [106] D. D. L. Chung, "Review: Graphite," *Journal of Materials Science*. 2002.

- [107] R. W. G. Wyckoff, *Crystal Structures - Volume 1*. New York: Interscience Publishers, 1963.
- [108] C. Lin *et al.*, "Quasi-one-dimensional graphene superlattices formed on high-index surfaces," *Phys. Rev. B - Condens. Matter Mater. Phys.*, vol. 89, no. 8, pp. 1–5, 2014.
- [109] C. Lin, N. Tong, W. Yang, R. Zhao, and Z. Hu, "Low energy electron diffraction study of high index copper surfaces underneath graphene," *Appl. Surf. Sci.*, vol. 347, pp. 147–154, 2015.
- [110] M. A. Valbuena, L. Walczak, J. Martínez-Blanco, I. Vobornik, P. Segovia, and E. G. Michel, "Lateral confinement effects of M-point Tamm state in vicinal Cu(100) surfaces," *Surf. Sci.*, vol. 630, pp. 144–152, 2014.